博士論文

Chemical Charging of Positive Electrode in Fuel Cell/Battery Systems

（燃料電池・蓄電池（FCB）システムにおける
正極の化学充電に関する研究）

ムセル　マイク イグナズ

Table of Contents

Table of tables IV
Table of figures V
Acknowledgements X
Abstract XII

Chapter 1 Introduction 1
1.1. Motivation 1
1.2. Electrochemical Energy Storage and Conversion Devices 3
1.2.1. Batteries 3
1.2.2. Fuel Cells 7
1.2.3. Fuel Cell/Battery System 10
1.3. Manganese Dioxide as Positive Electrode Material in FCB System 15
1.3.1. Physical Properties 15
1.3.2. Battery mode: 18
1.3.3. Fuel cell mode: 19
1.3.4. Fuel cell/battery mode: 21
1.4. Objective of this work 23

Chapter 2 Effect of MnO_2 Crystal Structure on Chemical Charging 25
2.1. Introduction 26
2.2. Experimental 27
2.3. Results and Discussion 30
2.3.1. Crystal Structure and Morphology Analysis 30
2.3.2. Electrochemical Characterization 37
2.4. Conclusion 45

Chapter 3 Chemical Charging Mechanism of MnO_2 with Oxygen 47
3.1. Introduction 48
3.2. Experimental 49
3.3. Results and discussion 50
3.3.1. Physical properties of MnO_2 and cyclic voltammograms 50
3.3.2. Chemical charging of MnO_2 with oxygen 52
3.4. Conclusions 61

Chapter 4 Surface Reaction and Proton Diffusion During Chemical Charging 63
4.1. Introduction 64
4.2. Results and discussion 65
4.2.1. Fuel cell/battery mode 65
4.2.2. Fuel cell mode 77
4.2.3. Battery mode 81
4.3. Conclusions 85

Chapter 5 Performance Enhancement with Nano-Sized λ-MnO_2 and Oxygen Reduction Catalyst 87
5.1. Introduction 88
5.2. Experimental 89
5.3. Results and discussion 90
5.3.1. Micro- and nano-sized λ-MnO_2 90
5.3.2. Fibrous λ-MnO_2 103
5.4. Conclusions 108

Chapter 7 Conclusions and Outlook 111
7.1. Conclusions 111
7.2. Recommendations for Future Work 114

Appendix A Standard Reduction potentials 119

Appendix B Measurement Techniques 120
Scanning Electron Microscopy 120
X-ray Diffraction 123
Brunauer-Emmett-Teller 124

Appendix C Ag-covered nano λ-MnO_2 Charge Curves 126
Introduction 128
Experimental 128
Results and discussion 129

Appendix D Synthesis of MnO_2 covered carbon nanofibers 139

Bibliography 140
List of Publications 150
Conferences 151
Honors 152

Table of tables

Table 1.1: Comparison of PbA, NiMH and LiB [12] 4
Table 1.2: Differences among fuel cells 7
Table 1.3: Mn–O bond lengths of different MnO_2 crystal structures in protonated and proton-free state 21
Table 2.1: Overview of synthesis conditions of all experiments. 28
Table 2.2: BET surface area of selected compounds. 36
Table 4.1: Slope and activation energies of γ- and λ-MnO_2 69
Table 4.2: Mn-O bond lengths of charged and discharged γ- and λ-MnO_2 72
Table 4.3: Crystal lattice parameters of charged and discharged γ- and λ-MnO_2 73
Table 5.1: BET surface area of selected samples 92
Table 5.2 Calculated diffusion coeficient for different materials 97

Table of figures

Fig. 1.1: Residual power outlook in Germany [3] 2
Fig. 1.2: Discharge curves at different currents 6
Fig. 1.3: Typical I-V curve found in fuel cells 10
Fig. 1.4: Main reactions taking place at the negative and positive electrode of FCB systems in (a) battery mode, (b) fuel cell mode, and (c) FCB mode. 11
Fig. 1.5: Comparison of chemical charging rate of (a) negative electrode and (b) positive electrode 14
Fig. 1.6: Elemental price of the chemical elements vs. crustal abundance [27] 16
Fig. 1.7: Tunnel structures of α-, β-, γ-, and δ-MnO_2 structures, showing that the void space decrease according to δ > α > γ > β. 17
Fig. 1.8: Crystal structure of λ-MnO_2 18
Fig. 1.9: Discharge curves of chemically charged γ-MnO_2H for 1 h and 48 h 22
Fig. 2.1: MnO_2 crystal structure phase diagram with KCl content and synthesis temperature as variables. 31
Fig. 2.2: XRD patterns of various MnO_2 samples with corresponding powder diffraction files. a) α-MnO_2 with JCPDS 44-141, b) β-MnO_2 with JCPDS No. 24-0735, c) γ-MnO_2 compounds with JCPDS No. 44-142, and d) δ-MnO_2 compounds with JCPDS No. 43-1456, e) commercial λ-MnO_2. 32
Fig. 2.3: SEM images of a) α-MnO_2 120-3-0.2 b) β-MnO_2 160-3-0, c) γ-MnO_2 120-3-0, d) commercial γ-MnO_2 (Tosoh), e) δ-MnO_2 90-1-1, and f) δ-MnO_2-cold. Magnification is 15,000× for a), b), and c) and 5,000× for d), e), and f). 35
Fig. 2.4: Linear sweep voltammetry of different materials at 0.1mV/s from open circuit to -1.0 V vs. Hg/HgO 38
Fig. 2.5: 1st discharge curves of various compounds. 39
Fig. 2.6: (a) Nyquist plots of commercial γ-MnO_2 and γ-MnO_2 120-3-0. SEM images of pasted (b) γ-MnO_2 120-3-0 and (c) commercial γ-MnO_2 on nickel foam. 40
Fig. 2.7: Discharge capacity and capacity retention of various compounds during first 31 cycles. ×: α-MnO2 120-3-0.2; ●: Comm. γ-MnO_2; ▲: γ-MnO2 120-3-0; +: β-MnO2 160-3-0; ■: δ-cold; ♦: δ-MnO2 90-1-1 42

Fig. 2.8: XRD spectra of samples after cycling. a) α-MnO_2 120-3-0.2, b) β-MnO_2 160-3-0, c) Comm. γ-MnO_2 and γ-MnO_2 120-3-0, d) δ-cold and δ-MnO_2 90-1-1, e) comm. λ-MnO_2. 43
Fig. 2.9: Proposed crystalline structure change of different MnO_2 structures during cycling in alkaline media between -0.5 V vs. Hg/HgO and 0.5 V vs. Hg/HgO. 45
Fig. 3.1: Three stages of chemical oxygen charging of MnOOH 48
Fig. 3.2: Set-up of pressurized vessel to supply oxygen to sample during regeneration with oxygen and ORR measurement. The side view in (b) only shows the layered assembly of the half-cell 49
Fig. 3.3: X-ray diffraction patterns of pristine (a) γ-MnO_2 and (b) λ-MnO_2. 50
Fig. 3.4: Scanning electron microscopy images of pristine (a) γ-MnO_2 and (b) λ-MnO_2. 51
Fig. 3.5: CV curves of γ-MnO_2 and λ-MnO_2 comprising five loops between −0.4 V and +0.5 V vs. Hg/HgO. All CV cycles were conducted at 0.1 mV/s. 52
Fig. 3.6: (a) potential evolution of γ-MnO_2 and λ-MnO_2 during chemical charging at 0.1 C, (b) subsequent electrochemical discharge curves, (c) cumulative discharge capacity of 10 FCB cycles 54
Fig. 3.7: (a) electrochemical charge curves and (b) calculated chemical charge cruves of γ- and λ-MnO_2 55
Fig. 3.8: change in charge rate of (a) γ-MnO_2 and (b) λ-MnO_2 during chemical charging with oxygen. In both electrodes, three stages were observed. In (a), data of extended charge step is shown in order to clearly highlight the three phases of γ-MnO_2 57
Fig. 3.9: Detailed overview of the chemical charging mechanism of MnOOH with oxygen. 61
Fig. 4.1: Discussion outline of this chapter 65
Fig. 4.2: Chemical charge rate of γ- and λ-MnO_2 with oxygen at 1.0 MPa. 66
Fig. 4.3: (a) electrochemical impedance spectroscopy curves of protonated ($MnOOH_{0.8}$) γ-MnO_2 and λ-MnO_2 with equivalent circuit model and 67
Fig. 4.4: Arrhenius plot of discharged γ- and λ-MnO_2. 69
Fig. 4.5: Dependency of charge-transfer resistance on state of charge 70
Fig. 4.6: Energy level of MnO_6 octahedron 71
Fig. 4.7: X-Ray diffraction patterns of pristine and electrochemically discharged γ- and λ-MnO_2. 72
Fig. 4.8: HOMO-LUMO in MnOOH 73

Fig. 4.9: Arrhenius plot for proton diffusion 76
Fig. 4.10: Sequence used to measure the oxygen reduction reaction rate of MnO_2, showing typical voltage evolution during each step. 78
Fig. 4.11: I-V curves of γ-MnO_2 and λ-MnO_2. 79
Fig. 4.12: X-ray diffraction patterns of (a) γ-MnO_2 and (b) λ-MnO_2 of used materials before and after oxygen reduction reaction measurements. 81
Fig. 4.13: Charge and discharge capacities of λ-MnO_2 and γ-MnO_2 at different rates. 82
Fig. 4.14: X-ray diffraction patterns of as-used samples and samples after first discharge and after 36 cycles at different rates. (a) γ-MnO_2, (b) λ-MnO_2 84
Fig. 5.1: SEM images of (a) "commercial", (b) "micro", and (c) "nano" λ-MnO_2 at different magnifications. 91
Fig. 5.2: XRD patterns of (a) "commercial", (b) "micro", and (c) "nano" λ-MnO_2 93
Fig. 5.3: Electrochemical discharge curves of selected samples after 1 h oxygen charge at 1.0 MPa 94
Fig. 5.4: concentration variation in a particle at different times 98
Fig. 5.5: Discharge capacity of selected samples at 0.2 C charge and different discharge rates 100
Fig. 5.6: XRD of nano, micro and commercial λ-MnO_2 after electrochemical cycling 101
Fig. 5.7: I-V curves of selected samples 102
Fig. 6.1:SEM images of λ-MnO_2 covered carbon fibers at two different magnifications 104
Fig. 6.2: XRD pattern of λ-MnO_2 covered carbon fibers 105
Fig. 6.3: Electrochemical discharge curves of different electrodes after 1 h chemical oxygen charge at 1.0 MPa 106
Fig. 6.4: Electrochemical discharge capacities of the fibrous electrode compared to a pasted electrode 107
Fig. 6.5: SEM images of the λ-MnO2 covered carbon fibers after electrochemically cycling. 108
Fig. 7.1: MnO_2 deposited on a nano-CF mesh 117
Fig. A.1: Standard reduction potentials at 298 K, 1 M, 1 atm 119
Fig. B.1: Electron gun in an SEM 121
Fig. B.2: SEM column 121
Fig. B.3: X-ray diffraction in two different crystal layers 124
Fig. 5.8: SEM image of Ag coated nano λ-MnO_2 129
Fig. 5.9: SEM and EDX images of Ag-coated nano λ-MnO_2 130

Fig. 5.10: XRD pattern of Ag-coated nano λ-MnO_2 130
Fig. C.1: SEM image of silver nanoparticles and MnO_2 131
Fig. C.2: SEM image of conglomerated silver nanoparticles and MnO_2 131
Fig. 5.11: ORR of Ag-coated and Ag-free nano λ-MnO_2 132
Fig. 5.12: Discharge capacities of the Ag-free and Ag-covered nano λ-MnO_2 electrodes. ... 133
Fig. 5.13: Charge curves of Ag-free and Ag-covered nano λ-MnO_2 electrodes during the 5^{th} cycle at 0.2 C 134
Fig. D.1: Charge curves of Ag-covered λ-MnO_2 highlighting the point at which oxygen evolution starts 136
Fig. 5.14: Discharge curves (0.1 C) of Ag-free and Ag-covered nano λ-MnO_2 electrodes after chemical oxygen charging 137
Fig. E.1: MnO_2 covered CNF 139

“Plans are nothing; planning is everything.” – Dwight D. Eisenhower

Acknowledgements

First and foremost, I would like to express my great appreciation to Professor Atsushi Tsutsumi for giving me the opportunity to do my PhD degree under his supervision. He has helped me tremendously throughout my studies with his large expertise and many hours of his precious time. His kind and supportive manner have made our discussions not only fruitful but also enjoyable.

Besides my advisor, I would like to thank all members of the thesis committee: Prof. Shikazono Naoki, Prof. Maruyama Shigeo, Prof. Yamada Atsuo, and Prof. Yokokawa Harumi for their insightful comments and the hard questions which incented me to improve my dissertation from various perspectives.

I would also like to thank my sempai, Dr. Bokkyu Choi for the valuable and constructive suggestions that helped me immensely during the analysis of my work. His input has greatly impacted my studies and his genial manner made the discussions not only fruitful but also pleasant.

My gratitude shall also be expressed to Professor Yasuki Kansha, Dr. Dhruba Panthi, and Mr. Ishizuka Masanori for the help and suggestions regarding not only my research work but also my future endeavors. It has always been a pleasure to exchange thoughts with them.

In addition, I would like to say thank you to all other laboratory members, both current students and others that have already found new opportunities outside academia, for the memorable times within and outside the campus. A lot of great memories have been built

throughout the last years. A special thanks also to all of my friends I have made during the last years in Japan, in particular our dinner group, for the amazing times together.

I would furthermore like to point out my appreciation to Exergy Power Systems, Inc. for the financial support and the possibility to work part-time for them during my studies.

Last but not least, I would like to sincerely thank my family, particularly my mother, for the support throughout my studies and willingness to let me study far away from home.

Abstract

A fuel cell/battery (FCB) system consists of metal hydride (MH) and MnO_2 as the negative and positive electrode, respectively, and can run according to three different modes: (i) battery mode, (ii) fuel cell mode, and (iii) FCB mode. In battery mode, the MH and MnO_2 are redox cycled according to a secondary alkaline battery. In fuel cell mode, the metal hydride and MnO_2 work as catalysts for proton oxidation and oxygen reduction reaction (ORR), respectively. Lastly, in FCB mode, discharged MH and discharged MnO_2 (MnOOH) are chemically charged with hydrogen and oxygen, respectively, followed by electrochemical discharge as in battery mode. This mode allows for a high energy density as found in fuel cells and a high power density as found in batteries.

Previously, it was found that the chemical charging of the MH negative electrode with hydrogen gas was considerably faster than chemical charging of the MnO_2 positive electrode with oxygen gas. The chemical charging of MnOOH thus constitutes the main part of this dissertation. In order to improve the chemical oxygen charge rate of MnO_2, first, different crystal structures (α-, β-, γ-, δ- and λ-MnO_2) were synthesized and compared in terms of capacity and crystal stability. During electrochemical redox cycling testing, α-, β-, and δ-MnO_2 were found to transform into non-rechargeable Mn_3O_4 and/or have a low capacity, which made them unsuitable as positive electrode in FCB systems. Thus, γ- and λ-MnO_2 were identified as the most promising structures as active materials in FCB systems and used for further studies.

As the main part of this dissertation, in-depth analysis of the reaction mechanism during chemical oxygen charging was conducted. This was done by measuring the potential during chemical oxygen charging and comparing the chemical charge curve with the electrochemical charge curve. Based on these curves, the chemical charge rate could be calculated and three

distinct stages could be identified. In the first stage, which lasted a few tens of seconds, oxygen adsorption was the rate limiting step. In the second stage, chemical charging at the surface of MnO_2, which included surface oxidation and proton removal from the crystal lattice, was found to be the rate determining step. In the last stage, proton diffusion from the bulk to the surface affected the overall charge rate.

To analyze the effect of physical properties of MnO_2 on the chemical oxygen charge mechanism, the reaction rates of two different MnO_2 crystal structures, i.e. γ-MnO_2 and λ-MnO_2, were analyzed during chemical charging at the surface and in the bulk. It was found that a limited crystal distortion was crucial to achieve low charge transfer resistance and thus quick surface oxidation. Furthermore, weak O–H bonds were beneficial for quick proton removal from the crystal lattice which enabled quick charging of the MnO_2 surface. A small particle size resulted in fast proton diffusion from bulk to surface which was advantageous for a complete charge of the MnO_2 particles. λ-MnO_2 was found to show a smaller crystal distortion than γ-MnO_2 and weak O–H bonds wherefore its surface could be charged rapidly. Its weakness – poor proton diffusion – was mainly assigned to the large particle size which resulted in long diffusion paths. Thus, to improve the chemical charge rate of the positive electrode, λ-MnO_2 consisting of small particles was synthesized and analyzed under chemical charging.

In-house synthesized nano λ-MnO_2 was found to be rapidly chemically charged with oxygen; after 1 h, 34.1% of the theoretical capacity could be chemically charged. In comparison, to achieve the same chemically charged capacity with previously used γ-MnO_2, ca. 48 h of chemical charging with oxygen was required. Furthermore, nano-sized λ-MnO_2 showed better performance during electrochemical cycling at high C-rates and ORR. The latter could even further be improved by depositing silver onto nano λ-MnO_2.

Finally, the possibility of using binder-free, fibrous structures was analyzed, wherefore λ-MnO_2 was deposited onto carbon fibers. Chemical oxygen charging analysis revealed an even faster charge rate of the fibrous electrodes compared to pasted electrodes made with nano λ-MnO_2. Within 1 h, 49.1% of the initial capacity could be charged with dissolved oxygen. Problems were however found with the structural stability. Due to delamination of the active material from the current collector, a high ohmic loss was identified, which affected the discharge potential. Nevertheless, this design showed the fastest oxygen chargeability among all samples analyzed in this work and is thus a promising structure for future development.

Chapter 1 Introduction

1.1. Motivation

As the use of intermittent renewable power sources, in particular solar and wind, has increased worldwide, energy storage has become a key element to sustain this trend [1]. This has led for example the public utilities commission of the state of California to set the state's targets for energy storage systems at a total of 1,325 MW by 2020 [2]. A country at the forefront of supporting renewable power is Germany. In the "Energiewende" (energy transition), various targets are defined, among which the renewable share is to reach 80% renewables by 2050 [3], which will make energy storage indispensable. In Fig. 1.1, the yearly distribution of residual power (power demand minus renewable power output) of Germany is shown in 2012 together with the expected curves for 2020, 2030, and 2050. In 2012, there was no time throughout the entire year where renewables produced more energy than the total energy consumption. This is expected to change in 2020 where during a few hours, more renewable power will be produced than consumed. This discrepancy will become worse in the following decades; as the renewables share increases, the hours of surplus power will increase accordingly. In order to avoid waste of this surplus power and sustain a reliable power supply during cloudy and wind-free periods, energy storage is of highest importance.

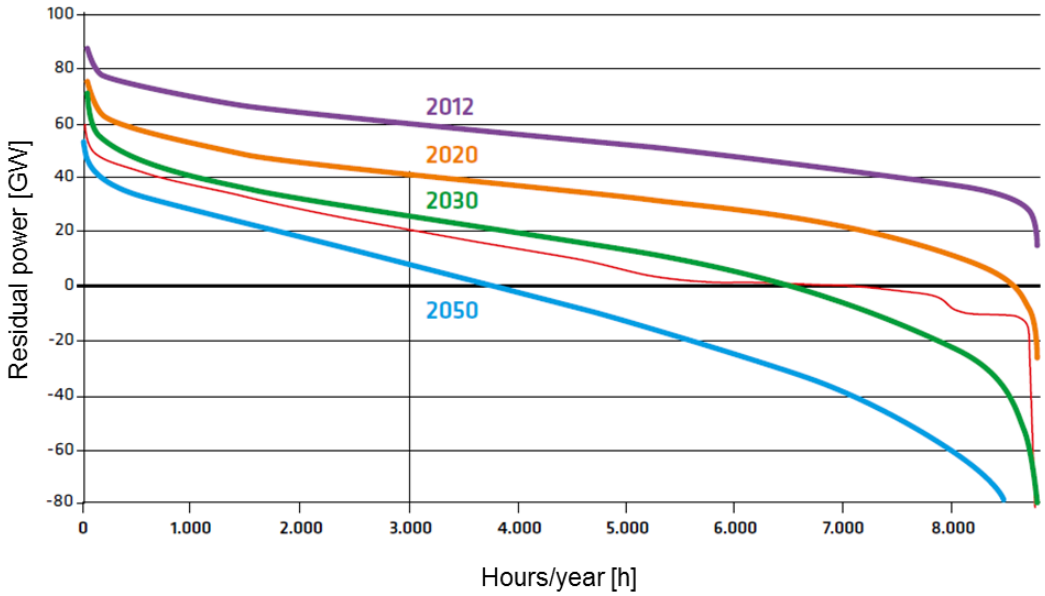

Fig. 1.1: Residual power outlook in Germany [3]

Both short-term storage (power intensive) and long-term storage (energy intensive) are required to substantially increase the use of renewable energy. Partly cloudy days can cause quick fluctuations in solar power output, requiring storage that can smoothen the output rapidly. On the other hand, wind-free nights can cause a long lasting absence of renewable power, requiring long-term storage to balance supply and demand.

Also for automobile applications, alternative energy storage technologies that compete with combustion engines are being commercialized. For example, Tesla motors recently announced its battery powered Model 3 which is targeting mass market [4]. And as the first commercially available fuel cell powered car, Toyota has introduced the Toyota Mirai in 2015 [5]. Both of these technologies bring the world closer to a net 0 emission society.

The motivation of this work is to contribute to this trend of going green. While the renewable share of power supply is increasing at rapid speeds world-wide, the energy storage deployment is lagging behind. This can be assigned to high cost, but also technological

uncertainty [6]. To remove this barrier, a lot of research has to be conducted to improve current technologies and develop novel concepts. This dissertation shall contribute to the development of a novel type of energy storage system, the fuel cell/battery (FCB).

1.2. Electrochemical Energy Storage and Conversion Devices

For electric and electrochemical storage devices, there is typically a trade-off between energy density and power densities, as shown by Ragone [7]. For example, supercapacitors have a high power density but low energy density. Fuel cells have a high energy density but low power density and batteries have an energy and power density that are between the ones of supercapacitors and fuel cells.

Several concepts have been proposed that promise to deliver simultaneously a high energy and power density by either combining fuel cells, batteries, and/or supercapacitors [8–10]. The FCB system has been introduced by our group as an alternative electrochemical cell which can achieve a power density similar to a secondary battery and an energy density similar to a fuel cell [11]. Before explaining the functioning of the FCB system, in the next sub-chapters, the basics of batteries and fuel cells are explained, followed by details about the FCB system.

1.2.1. Batteries

Batteries can be split into primary (single discharge) and secondary (rechargeable) cells with a wide combination of electrode and electrolyte materials. Some of the most widely used secondary batteries are lead acid (PbA), nickel-metal hydride (NiMH) and lithium ion batteries (LiB). A comparative overview is shown in Table 1.1.

Table 1.1: Comparison of PbA, NiMH and LiB [12]

	PbA	NiMH	LiB
Gravimetric energy density	Low	Medium	High
Gravimetric power density	High	High	Medium
Cycle life	Low	Medium	Medium
Overcharge tolerance	High	Low	Very low
Cost	Low	Medium	High

Due to the similarity of the NiMH battery to the FCB, the basics of a battery shall be explained according to the chemistry of the NiMH battery. A battery consists of three main parts; a positive electrode, a negative electrode and an electrolyte, which, in case of NiMH, are nickel hydroxide (NiOOH), metal hydride (MH) and an alkali (e.g. 6 M KOH), respectively. During electrochemical redox cycling (i.e. charging and discharging), following reactions take place at the negative and positive electrode:

(i) Negative electrode

$$M^0 + H_2O + e^- \underset{\text{discharge}}{\overset{\text{charge}}{\rightleftharpoons}} M^{-I}H + OH^-. \quad (1.1)$$

(ii) Positive electrode:

$$Ni^{II}(OH)_2 + OH^- \underset{\text{discharge}}{\overset{\text{charge}}{\rightleftharpoons}} Ni^{III}OOH + H_2O + e^-. \quad (1.2)$$

The electrons thereby flow through an external circuit to which either power is supplied (when discharging the battery) or from which power is drawn (when charging the battery). Eqs. 1.1 and 1.2 also show the effect of charging and discharging on the oxidation states of the metals. When charging, the oxidation state of Ni increases from the binary to tertiary state by

removing a proton-electron pair from the crystal lattice. Accordingly, the oxidation number of metal hydride changes from 0 to -1 during charging. The potential at which these and other materials' reactions occur is shown in tables of standard electrode potentials and can be found in Appendix A. In case of a NiMH battery, the standard potential E^0 for eq. 1.1 is -0.83 V and for eq. 1.2, E^0 is 0.45 V. The resulting open circuit potential of a NiMH battery is thus 1.28 V.

During electrochemical cycling, different losses occur which lower the overall potential during discharging and increase the potential during charging. These losses can be summarized as (i) electrode activation polarization losses, (ii) ohmic losses, and (iii) concentration polarization losses [13].

(i) The activation polarization losses can be quantified with the Butler-Volmer equation and depends on electrode reactions:

$$i = i_0 \left(e^{\frac{(1-\alpha)\eta F}{RT}} - e^{-\frac{\alpha \eta F}{RT}} \right). \quad (1.3)$$

Thereby i is the electrode current density [A/m^2], i_0 is the exchange current density [A/m^2], α is the symmetry factor [-], η is the activation polarization loss (defined as electrode potential minus equilibrium potential), F is the Faraday constant (96 485 C mol^{-1}), R is the universal gas constant (8.314 J mol^{-1} K^{-1}), and T is the temperature [K]. This equation describes how the electrode potential depends on the electrical current of an electrode. Depending on the current density, the activation polarization loss changes. For example, if a high current is applied during discharge, the cell will show a smaller potential, which is shown exemplarily in Fig. 1.2. As the current density increases from 0.1 C to 1.0 C and 10.0 C, the potential during discharge decreases. (Note, the C-rate is defined as inverse of time in hours it takes to fully charge or

discharge the cell. E.g. 10 C equals to a current that allows for a complete discharge in 1/10 h = 6 min.)

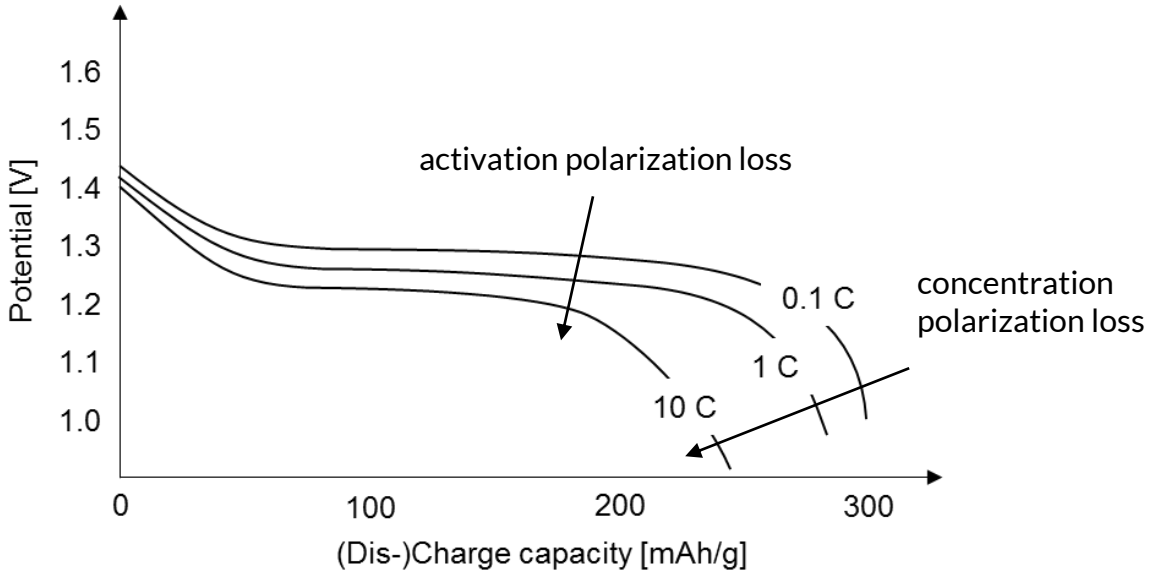

Fig. 1.2: Discharge curves at different currents

(ii) The ohmic losses contain losses in both the electrodes and electrolyte. The electronic conductivity is typically higher than the ionic conductivity. The electrolyte ohmic drop depends on the concentration of the ions in the solution. In case of KOH solution, which is widely used in NiMH batteries and the FCB system, the highest conductivity is achieved at 6 M KOH [14], which is why the same concentration is used in this work.

(iii) The concentration polarization losses, which define the discharge curve around the end of the discharge step, can be calculated with the Nernst equation:

$$E_{Nernst} = E^0 + \frac{RT}{nF} \ln \frac{[A]^a}{[B]^b} \qquad (1.4)$$

Whereby E^0 is the standard reduction potential depending on the electrode materials (see Appendix A) [V], n is the number of electrons exchanged [-], [A] and [B] are the concentration

of the positive and negative electrode, respectively [mol/L], and the indices ‘a’ and ‘b’ are stoichiometric values to balance the overall reaction [-]. The concentration polarization losses affect the curves at the end of the discharge due to diffusion limitation and result in a lower discharge capacity during high C-rate discharge, as shown in Fig. 1.2.

In typical battery cells, the reactions between electrolyte and electrodes take place at a two-phase interface. This allows for high power densities. However, because batteries are typically a closed system (apart from metal air batteries), all the energy has to be stored in the electrodes, resulting in comparatively small energy densities.

1.2.2. Fuel Cells

As for batteries, a wide range of fuel cells consisting of different materials exist. Some of the most promising are the proton exchange fuel cell (PEFC), alkaline fuel cell (AFC) and solid oxide fuel cell (SOFC) [15], summarized in Table 1.2.

Table 1.2: Differences among fuel cells

	PEFC	AFC	SOFC
Operating temperature	Medium	Low	High
Efficiency	Medium	High	High
Electrical power	Medium	Low	High

The AFC uses an alkaline electrolyte and is thus most similar to the FCB. Its reactions shall thus be used here as an example.

In case of an AFC, the overall reaction at the negative electrode (anode) is as follows:

$$2H_2 + 4OH^- \rightarrow 4H_2O + 4e^-. \quad (1.5)$$

This reaction is typically much faster than the reactions at the positive electrode.

At the positive electrode (cathode), according to E. Yeager [16] two different paths are possible for the oxygen reduction reaction (ORR) in alkaline medium; either a $4e^-$ transfer or a $2e^-$ transfer. The reactions are as follows:

(i) Direct 4-electron pathway:

$$O_2 + 2H_2O + 4e^- \rightarrow 4OH^-. \quad (1.6)$$

(ii) (2+2)-electron pathway (peroxide pathway):

$$O_2 + H_2O + 2e^- \rightarrow HO_2^- + OH^-. \quad (1.7)$$

This reaction is then either followed by a further reduction reaction:

$$HO_2^- + H_2O + 2e^- \rightarrow 3OH^-, \quad (1.8)$$

or the decomposition reaction:

$$2HO_2^- \rightarrow 2OH^- + O_2. \quad (1.9)$$

Typically, the 4-electron pathway is preferred due to faster reaction kinetics [17].

The overall reaction of an AFC is thus as follows:

$$H_2 + \frac{1}{2}O_2 \rightarrow H_2O. \quad (1.10)$$

This is the most basic and common reaction encountered in fuel cells [18]. The change in enthalpy can be calculated according to following reaction:

$$\Delta H = -nFE_t. \quad (1.11)$$

Whereby n is the number of electrons involved (=2 for eq. 1.10), and E_t the thermos-neutral potential [V]. The change in enthalpy is -285.8 kJ/mol for eq. 1.10, wherefore E_t is 1.48 V. However, this voltage cannot be achieved due to entropy loss from heat generation. To calculate the theoretical maximum voltage, the Gibbs free energy has to be used. In case the reactants and products are in their standard states, the standard free energy of reaction (1.10) can be calculated according to:

$$\Delta G^0 = -nFE^0. \qquad (1.12)$$

ΔG^0 of eq. 1.10 can be quantified at -237.2 kJ/mol, wherefore the standard potential E^0 is 1.229 V. This holds for an ideal process in any fuel cell running on hydrogen and oxygen as fuels (i.e. not only AFC, but also PEFC and SOFC if hydrogen is used as fuel).

Further losses occur because fuel cells typically do not run under standard conditions. Equivalent to batteries, losses occur during operation which can be summarized as (i) activation losses, (ii) ohmic losses and (iii) concentration losses.

Activation losses account for most of the losses at low current density and occur because a certain amount of energy is necessary to force the electrochemical oxidation reaction. At a higher current density, typically in the designated area of fuel cell operation, ohmic losses occur due to limited ion conductivity of the electrolyte/membrane and internal resistance towards electron flow. In the high current density region, the main loss is due to concentration overpotential, which is attributable to mass transport limitations. As can be seen in the Nernst equation, if the partial pressures of the feed gasses decrease because of a too fast consumption, the potential declines accordingly. For a fuel cell that works according to eq. 1.10, the Nernst potential is as follows:

$$E_{Nernst} = E^0 + \frac{RT}{2F} \ln\left(\frac{p_{\dot{H}_2} \cdot (p_{\dot{O}_2})^{0.5}}{p_{\dot{H}_2O}}\right). \quad (1.13)$$

Whereby p_I is the partial pressure of the educts and products [Pa]. All losses are summarized in a polarization curve (I-V curve), exemplarily shown in Fig. 1.3.

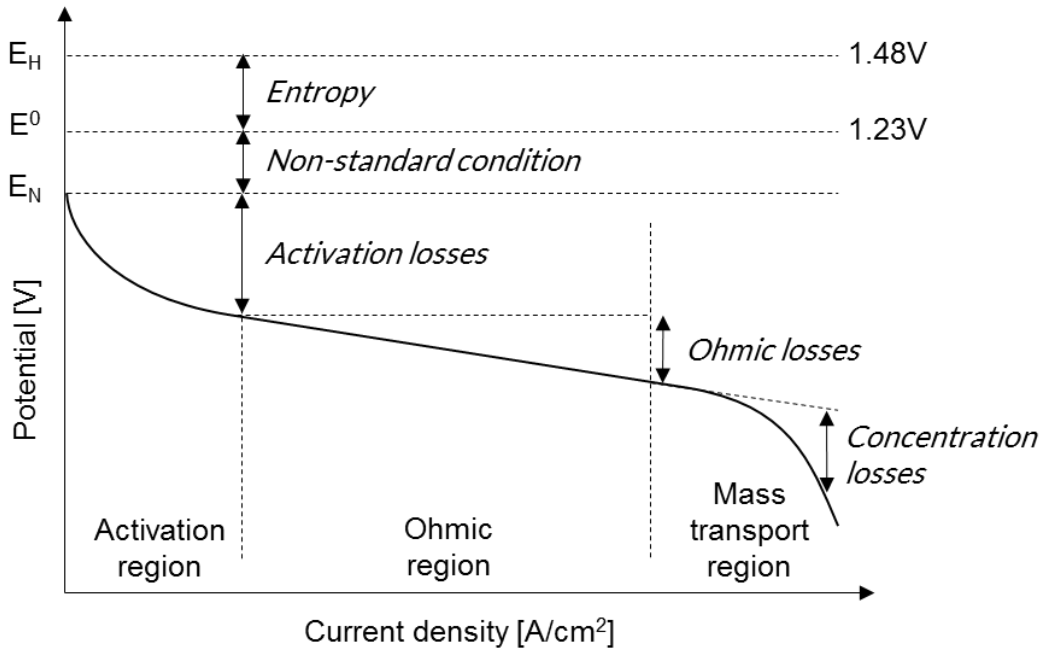

Fig. 1.3: Typical I-V curve found in fuel cells

Independent of the chemistry of the fuel cell, the main reactions take place at a three-phase interface between fuel (hydrogen containing compound and oxygen), electrolyte and catalyst. This limits the area where the reactions take place, causing a low power density in fuel cells. However, because the oxygen is typically taken from the atmosphere, high energy densities can be achieved with fuel cells.

1.2.3. Fuel Cell/Battery System

The FCB system combines the operating principle of a (high energy density) fuel cell with a (high power density) battery and has been proposed previously [11,19–21]. The main

reactions of an FCB system are summarized in Fig. 1.4, which shows the reaction of the negative and positive electrode during (a) battery mode, (b) fuel cell mode, and (c) FCB mode.

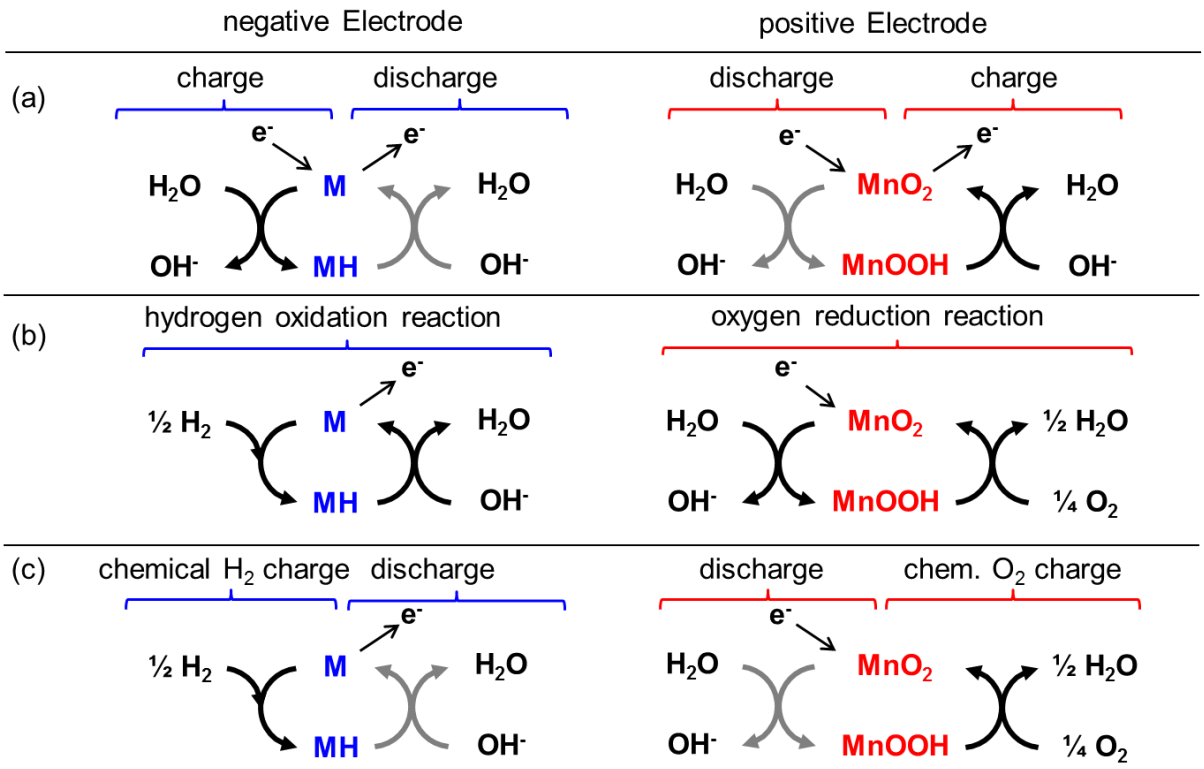

Fig. 1.4: Main reactions taking place at the negative and positive electrode of FCB systems in (a) battery mode, (b) fuel cell mode, and (c) FCB mode.

As a negative electrode material for the FCB system, an AB_5 type MH was chosen, which is also used as the negative electrode in NiMH batteries. This metal alloy can be electrochemically cycled to work under battery mode [22] by reducing to protonated metal alloy and re-oxidizing to deprotonated metal alloy. In fuel cell mode, the metal hydride works as catalyst for the hydrogen oxidation reaction. Lastly, in FCB mode, discharged metal alloy can be charged with hydrogen and subsequently discharged electrochemically by releasing an electron.

As the positive electrode for the FCB system, MnO_2 has been chosen as it can work during the three different operating modes. In battery mode, the MnO_2 is electrochemically cycled by reducing MnO_2 (charged) to MnOOH (discharged) and oxidizing MnOOH back to MnO_2. In fuel cell mode, MnO_2 works as a catalyst for the oxygen reduction reaction (ORR). In FCB mode, discharged MnOOH is chemically charged with oxygen to form MnO_2 and H_2O as a by-product, followed by an electrochemical discharge step according to battery mode.

Fig. 1.4 highlights the similarities among the different modes. In both battery and FCB mode, there can be a time delay between charging and discharging, meaning energy is stored in the electrodes themselves. In addition, the electrochemical discharge process is identical and all processes take place at two-phase interfaces. The difference of these modes is that in battery mode, the input energy during charging is electrical energy, whereas in FCB mode, the input energy during charging is chemical energy (from hydrogen and oxygen). The overall reactions are thus different among battery mode and FCB mode. The overall reaction is what is equivalent in fuel cell and FCB mode; in fuel cell mode, the input energy is also chemical energy and the output is electrical energy and water, as is the case in FCB mode. However, in fuel cell mode both electrodes work only as catalyst, which means that energy is not stored in the electrodes. Thus, in fuel cell mode the chemical energy supply and electrical energy output occur at the same time and reactions occur at a three-phase interface.

The FCB mode thus combines the advantages of battery and fuel cell mode. The FCB mode allows for electrochemical storage in the electrodes, which allows for a short but high power discharge burst due to the two-phase interface. And because the input energy is hydrogen and oxygen (which can be taken from the environment), a high energy density can be achieved.

Suitable applications for the FCB could be stationary applications for the grid or hybrid fuel cell cars. In case of stationary applications, the FCB system could stabilize the grid through ancillary services. Fluctuations in the grid's frequency and voltage occur rapidly, thus the FCB could balance the quick, but typically short fluctuations in battery mode. For example, if the frequency suddenly drops due to an outage of a power plant below a certain threshold, the FCB system could discharge rapidly in battery mode to supply a sufficient burst to stabilize the frequency. Analogously, the FCB system could electrochemically be charged for a short time in case of a too high frequency. In addition, in case of long periods of surplus power due to high use of intermittent renewables, energy from wind and solar could be stored in hydrogen. During times of high power demand and low renewables output then, hydrogen could fuel the FCB system which could work under fuel cell mode to supply power.

The functioning of the FCB system would be similar in a vehicle. During acceleration, a high power output is required which could be supplied by electrochemically discharging the FCB according to battery mode. Once accelerated, the vehicle only needs little power and instead, a high energy density is required to achieve a long range. Thus, during cruising, the operating mode would be switched from battery to fuel cell mode by supplying hydrogen and oxygen to the FCB system. During breaking, kinetic energy could be transformed into electrochemical energy by switching the FCB back into battery (charge) mode, thus allowing to store energy which would otherwise be wasted in the form of heat. Due to inefficiencies between charging (breaking) and discharging (accelerating), the state of charge of the FCB would decrease during driving. This loss could be balanced out by supplying hydrogen and oxygen during stand-by phases, thus chemically charging the FCB system.

Previous studies found that the chemical charge rate of the negative and positive electrode with hydrogen and oxygen, respectively, are considerably different. As can be seen in Fig. 1.5, discharged metal hydride could be recharged to ca. 70% within just 10 min [22]. In contrast to that, the positive electrode could only be charged with oxygen to ca. 13 % within 1 h [20]. It is thus obvious that the chemical charging of MnOOH has to be accelerated in order to allow for a better over-all performance of the FCB system.

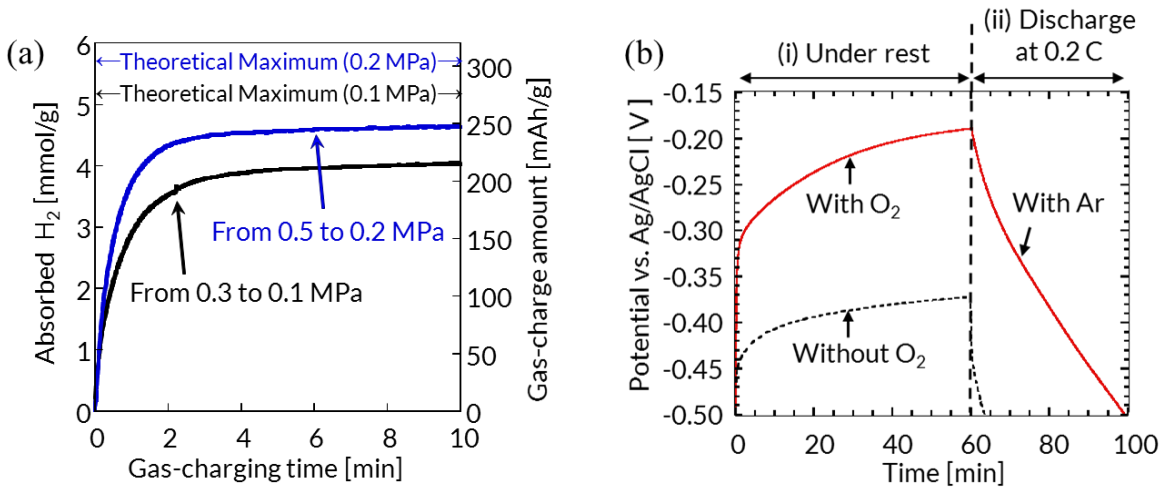

Fig. 1.5: Comparison of chemical charging rate of (a) negative electrode and (b) positive electrode

In previous work, highly pressurized oxygen dissolved in electrolyte was found to improve the chemical charge rate of MnO_2 [23], however, the results were still far from being satisfying. Additional work at the positive electrode was thus required to advance the over-all capabilities of the FCB system.

In the next subchapter, more details about MnO_2 are given and its functioning during different modes is evaluated.

1.3. Manganese Dioxide as Positive Electrode Material in FCB System

Using MnO_2 as the positive electrode in FCB system provides several advantages, such as low cost, high abundance, and environmental compatibility [24–26], but the main reason for using MnO_2 as positive electrode is because it is capable of fulfilling following minimum requirements for each operating mode in the FCB system:

- Battery mode: electrochemical redox cyclability
- Fuel cell mode: catalytic capability to reduce oxygen
- Fuel cell/battery mode: chemical charging with oxygen

These modes are explained more in depth in the forthcoming sub-chapters, after a general introduction into MnO_2.

1.3.1. Physical Properties

Manganese is a transition metal abundantly present in the earth's crust and its market price is accordingly very low, as shown in Fig. 1.6. Manganese can be present in various oxidation states and as part of different compounds. In this work, the most important material is MnO_2, in which manganese is in its quaternary oxidation state. Other compounds that are of importance in this work are MnOOH, in which Mn is in its tertiary oxidation state and hausmannite (Mn_3O_4) in which half of Mn is in the tertiary and half in the secondary oxidation state.

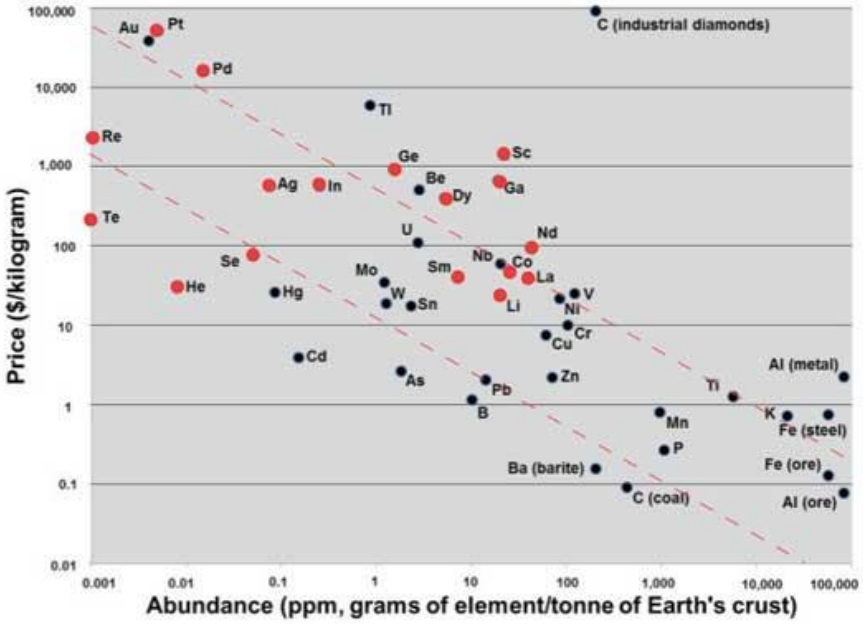

Fig. 1.6: Elemental price of the chemical elements vs. crustal abundance [27]

In case of MnO_2, the basic building block is a MnO_6 octahedral which, depending on its alignment, creates different crystal structures. Several different MnO_2 crystal structures exist (typically distinguished by a Greek letter), with some of the historically most analyzed compounds being α-, β-, γ-, and δ-MnO_2. These crystal structures are shown in Fig. 1.7 [28]. All of the structures differ by the allocation of the MnO_6 octahedron, leading to compounds with different void spaces. The largest void space with an interlayer separation of ~7 Å is found in δ-MnO_2, followed by α-MnO_2 which consists of a combination of 1×1 and 2×2 tunnel structures with interlayer separations of 1.89 Å and 4.6 Å, respectively. The smallest void spaces are observed in γ-MnO_2 (combination of 1×1 and 1×2 tunnels with interlayer separations of 1.89 Å and 2.3 Å, respectively) and β-MnO_2 (1×1 tunnels with an interlayer separation of 1.89 Å) [29–31].

A lot of comparative studies among different crystal structures have been conducted by various researchers for different applications, including as electrodes in supercapacitors [32–

35], as positive electrodes in lithium ion batteries [36–40], as positive electrodes in alkaline batteries [41–43] and as catalyst for oxygen reduction in fuel cells [44,45]. For the use as positive electrode in FCB systems, previously only γ-MnO_2 has been used and no analysis of other compounds was conducted.

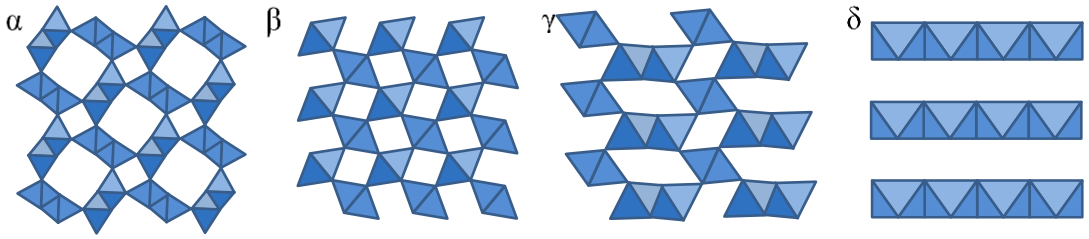

Fig. 1.7: Tunnel structures of α-, β-, γ-, and δ-MnO_2 structures, showing that the void space decrease according to δ > α > γ > β.

A comparatively new material, which has been studied much less than other compounds in alkaline batteries, is λ-MnO_2, shown in Fig. 1.8. This material was first obtained by Hunter (1981) by acid treatment of $LiMn_2O_4$ [46]. Upon removal of lithium ions of $LiMn_2O_4$, which can be done by soft chemical methods (either electrochemical or acid leaching) the compound sustains its spinel structure, in which the Mn ions occupy the 16d sites in *Fd3m*. The result is a three-dimensional array of corner-sharing tetrahedral [47]. During the last two decades, λ-MnO_2 has attracted a lot of attention as positive electrode material in lithium ion batteries because spinel structures provide a stable three-dimensional interstitial space for unrestricted diffusion of lithium ions through the crystal lattice [40,48–50].

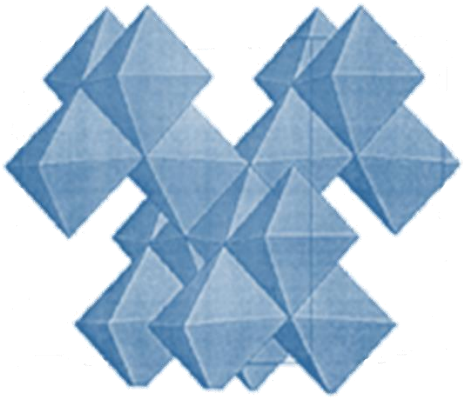

Fig. 1.8: Crystal structure of λ-MnO_2

1.3.2. Battery mode:

MnO_2 is commonly used in primary (i.e., non-rechargeable) alkaline household batteries, highlighting its benefits (such as low cost) but also indicating its main shortcoming: poor recharge ability [51]. Several studies discuss strategies to improve its cyclability in an alkaline environment, such as by adding dopants [52,53] or limiting its discharge potential [51,54]. In battery mode, the electrochemical redox reaction of MnO_2 as positive electrode material is as follows:

$$Mn^{IV}O_2 + OH^- \underset{\text{charge}}{\overset{\text{discharge}}{\rightleftharpoons}} Mn^{III}OOH + H_2O + e^-. \qquad (1.14)$$

The proton intercalation and removal during electrochemical cycling can strongly affect the crystal structure. For the application as positive electrode in alkaline batteries, a lot of effort was put into understanding the crystal structure transformation during discharge. Depending on the initial crystal structures, different paths have been observed. α-MnO_2 was found to transform during discharge in a two-step process first into Mn_3O_4 and upon further discharge into $Mn(OH)_2$ in 9 M KOH [55]. β-MnO_2, in contrast, was found to be reduced in a one-step directly to $Mn(OH)_2$ [55]. γ-MnO_2 transforms during discharge first into amorphous phase,

which, upon further discharge, transforms into $Mn(OH)_2$ [55,56]. δ-MnO_2 was found to transform into Mn_3O_4 during discharge [57]. No similar study about λ-MnO_2 could be found.

The resulting structure after discharge is crucial for assessing the cyclability and thus the applicability in a FCB. While $Mn(OH)_2$ was found to be rechargeable and to be transformed into δ-MnO_2 during charge [57], Mn_3O_4 is known to not be electrochemically rechargeable [58]. It is thus crucial to inhibit the formation of Mn_3O_4, which can be done for example by limiting the discharge capacity. In case of γ-MnO_2, it was found that if the discharge is stopped at -0.4 V vs. Hg/HgO, the discharge is limited to a 1 electron reaction, thus forming only MnOOH but no Mn_3O_4. MnOOH can then be recharged to form MnO_2 [20]. However, the recharge may not necessarily form pure γ-MnO_2. An extensive research performed by Donne *et al*. [58–60], which helped understand the paths involved during cycling of γ-MnO_2, found that γ-MnO_2 slowly transforms into δ-MnO_2 during cycling. This is a non-desirable transformation [61] as δ-MnO_2 can transform into Mn_3O_4 [57].

1.3.3. Fuel cell mode:

In fuel cell mode, the MnO_2 functions as catalyst for the ORR. It is well known that MnO_2 can function as an ORR catalyst to reduce oxygen according to the $4e^-$ transfer or the $2e^-$ transfer. In a $4e^-$ transfer following reactions occur [62,63]:

$$MnO_2 + H_2O + e^- \leftrightarrow MnOOH + OH^-, \quad (1.15)$$

$$MnOOH + \frac{1}{2}O_2 \leftrightarrow (MnOOH + O_{ads}), \quad (1.16)$$

$$(MnOOH + O_{ads}) + e^- \leftrightarrow MnO_2 + OH^-. \quad (1.17)$$

And according to a $2e^-$ transfer, following reactions occur:

$$MnO_2 + H_2O + e^- \leftrightarrow MnOOH + OH^-, \quad (1.18)$$

$$MnOOH + O_2 \leftrightarrow MnOOH + O_{2,ads}, \quad (1.19)$$

$$MnOOH + O_{2,ads} + e^- \leftrightarrow MnO_2 + HO_2^-. \quad (1.20)$$

The peroxide ion is then either degraded directly by MnO_2 which is known to have high catalytic capabilities toward peroxides:

$$2HO_2^- \rightarrow 2OH^- + O_2. \quad (1.21)$$

Alternatively, the peroxide ion is degraded by following disproportionation reaction which makes the $2e^-$ transfer an overall quasi $4e^-$ oxygen reduction path [64–66]:

$$HO_2^- + H_2O + 2e^- \rightarrow 3OH^-. \quad (1.22)$$

Several researchers [54,62,67,68] investigated the effect of the MnO_2 crystal structure on the electrocatalytic activity for ORR in fuel cell mode. They reported that α- and δ-MnO_2, which have a large void space, exhibit higher electrocatalytic activity than other MnO_2 crystal structures, such as β-MnO_2. Reasons for the high electrocatalytic activity of α-, and δ-MnO_2 were proposed to be due to fast adsorption of reactants and desorption products into and out of structure because of the large void space [54]. However, considering the physical properties of oxygen, it seems unlikely that oxygen absorbs into the crystal lattice. Instead, the bond strength is more likely to be the main parameter affecting the ORR rate. According to Stoerzinger *et al.*, it is well accepted that the rate limiting step of ORR in Mn containing materials is the hydroxide displacement by O_2 [69]. In case of MnO_2 this reaction is as follows:

$$MnO(OH) + O_2 + e^- \rightarrow MnO(OO) + OH^-. \quad (1.23)$$

The bond strength between Mn and OH is thus crucial for the ORR rate: the longer the bond, the weaker its force and therefore the faster the ORR rate [69]. The Mn–O bond length

of several MnO_2 structures is summarized in Table 1.3. Due to the structural properties of β- and γ-MnO_2, different Mn–O bond lengths can be observed in those materials.

Table 1.3: Mn–O bond lengths of different MnO_2 crystal structures in protonated and proton-free state

Crystal form	Mn–O bond length in MnO_2 [Å]	Ref.
α	1.90	[70]
β	1.88 and 1.90	[71]
γ	From 1.88 to 1.97	[72]
δ	1.93	[73]
λ	1.95	[74]

1.3.4. Fuel cell/battery mode:

In FCB mode, MnO_2 is first electrochemically discharged to MnOOH as in battery mode:

$$MnO_2 + OH^- \rightarrow MnOOH + H_2O + e^-. \quad (1.24)$$

After electrochemical discharge, MnOOH can be chemically charged with oxygen according to following reaction:

$$MnOOH + \frac{1}{4}O_2 \rightarrow MnO_2 + \frac{1}{2}H_2O. \quad (1.25)$$

In previous work by Choi *et al.* it was suggested that the rate limiting step was the oxidation reaction, and the proton diffusion rate in MnO_2 and/or dissociation of oxygen on MnO_2 should be improved to increase the chemical charging rate [23]. It was shown that increasing the density of dissolved oxygen in the electrolyte (by pressurizing the cell) increases the charge rate.

It was then claimed that the chemical charge rate of discharged MnOOH is constant [23]. As such, it was proposed that at a pressure of 1.0 MPa, γ-MnO_2 could be charged at a rate of 0.5 mAh/(g·min), which resulted in a theoretical required time to reach full charge of 10.3 h. To verify this claim, the same chemical charging experiment was conducted by first fully discharging (electrochemically) a γ-MnO_2 electrode, followed by chemical charging with oxygen for 48 h. This was considerably more than the required 10.3 h, but to account for any kind of losses, extra charge time was added to the experiment.

In Fig. 1.9, the resulting electrochemical discharge curves after chemical oxygen charging for 1 h and 48 h are shown.

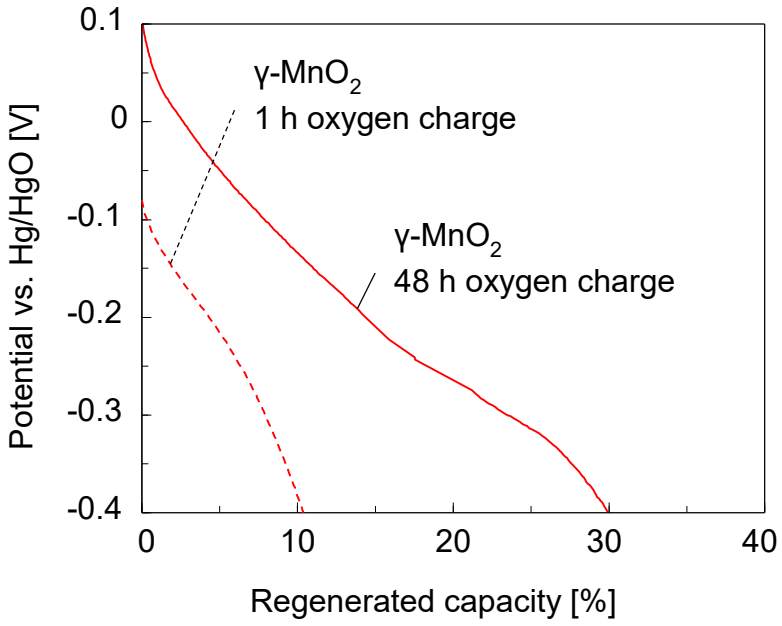

Fig. 1.9: Discharge curves of chemically charged γ-MnO_2H for 1 h and 48 h

It can be seen that after 1 h, ca. 11% of the theoretical capacity (33.9 mAh/g) could be discharged, which equals to a charge rate of 0.56 mAh/(g·min) and is thus similar to the previously suggested 0.5 mAh/(g·min) [23]. After 48 h, however, the charged capacity was

only 30% of the theoretical capacity (92.0 mAh/g), which equals to a charge rate of 0.032 mAh/(g·min) and means that in contrast to the previous claim, the charge rate is **non**-linear. It is thus clear that to improve the chemical charge rate with oxygen, a better understanding of the chemical oxygen charge mechanism needs to be gained.

1.4. Objective of this work

The objective of this work can be split into three major parts. The first objective was to identify the most promising MnO_2 crystal structures to be used as positive electrode in FCB systems. In Chapter 2, different crystal structure were synthesized and capacity and stability analysis was conducted during battery mode which allowed for a quick analysis of the capabilities of different MnO_2 crystal structures for the FCB system. The most promising crystal structures were then chosen for the next part of this dissertation.

Secondly, the chemical oxygen charging was analyzed in depth in order to better understand the underlying mechanism of chemical charging with oxygen. In Chapter 3, a novel measurement technique was employed which allowed for constant tracking of the potential during chemical oxygen charging. By knowing the chemical oxygen charge curve, the charge rate could be deducted which showed three distinct stages within one hour. In Chapter 4, the effect of morphology on the chemical charge rate could be analyzed by comparing the chemical oxygen charge curves of two different materials. Different physical properties, such as crystal structure, O–H bond length, and surface area were found to affect the charge rate during different stages.

The third objective was to improve the performance of the electroactive material. This included downsizing of the MnO_2 particles and coating with a catalyst, both of which were

expected to be beneficial for the chemical charge rate of MnO_2. This was done in Chapter 5. In addition, a fibrous electrode was manufactured to assess the possibility of using an alternative, binder-free design.

The focus throughout this work was on the chemical oxygen charging of MnO_2. Nevertheless, most chapters also analyzed the capability of different MnO_2 samples to work under battery mode and/or fuel cell mode. First and foremost, analyzing the fuel cell mode and battery mode also helped understand chemical charging mechanism. But in addition to that, it helped verify whether the different MnO_2 samples can fulfill all operating modes of the FCB system and are thus suitable as positive electrode in a FCB system.

Chapter 2 Effect of MnO_2 Crystal Structure on Chemical Charging

Abstract

The crystal structures and electrochemical properties of α-, β-, γ-, and δ-MnO_2, synthesized by a redox method under various synthesis conditions, were studied for the application of MnO_2 as a positive electrode in a fuel cell/battery (FCB) system and compared with commercial γ- and λ-MnO_2. The effects of potassium ion concentration (0–10 M) and temperature (60–160°C) on the morphology of synthesized MnO_2 were investigated by X-ray diffraction, scanning electron microscopy, and the Brunauer-Emmett-Teller method. In addition, the charge and discharge characteristics, and life cycle performance of MnO_2 as a positive electrode in an FCB system, were investigated by sweep voltammetry and potentiometry. The results indicate that four different crystal structures were obtained by different synthesis conditions: three tunnel structures (α-, β-, and γ-MnO_2) and one layered structure (δ-MnO_2). The effects of precipitation conditions were mapped and summarized in a phase diagram. Electrochemical testing showed that MnO_2 with small tunnel structures (i.e., β- and γ-MnO_2) exhibit better life cycle performance than either large tunnel structure α-MnO_2 or layered δ-MnO_2. Based on XRD analysis carried out after cycling, a schematic diagram is proposed to explain the degradation of the different MnO_2 compounds.

2.1. Introduction

The goal of this chapter was to identify possible MnO_2 crystal structures for FCB systems. For an MnO_2 crystal structure to be suitable as positive electrode material in FCB systems, two of the basic conditions are capacity and stability. Firstly, the structure has to be sufficiently stable in order to inhibit transformation into Mn_3O_4 or another non-rechargeable structure. Secondly, the crystal structure has to have a satisfyingly high capacity. Although there is no strict limit which can be defined as satisfying or not, it is suggested here that if the capacity is below 50% of the theoretical maximum, the capacity is too low to be considered for future work.

MnO_2 with different crystal structures were synthesized by a redox method. Four different MnO_2 crystal structures, i.e. α-, β-, γ-, and δ-MnO_2, could be obtained by varying two main conditions of the synthesis bath, namely KCl concentration and temperature. The effect of alkali metals, such as K^+, Na^+, or Li^+, as a template during MnO_2 synthesis has been reported before [28,29,75,76] and this chapter confirms that the K ions are readily capable of influencing the synthesized crystal structure. The findings were mapped in a phase diagram to summarize the effect of both KCl concentration and temperature on the synthesized crystal structure.

Seven different samples (two of each γ- and δ-MnO_2, and one of each α- and β- and λ-MnO_2) were analyzed during electrochemical redox cycling to measure their capacity and after electrochemical cycling, XRD measurements were conducted to analyze the crystal stability. The stability was analyzed under battery mode due to the fact that electrochemical cycling allowed for an easier and faster way than cycling under FCB mode. It was shown previously that MnO_2 behaves very similarly during chemical and electrochemical charging in terms of crystal changes [23]. The reason for this behavior is likely because during both chemical and

electrochemical charging, protons are removed from the crystal lattice. Furthermore, it is likely that the electrochemical charging is more debilitating than the chemical charging as in battery mode, the charged capacity is much higher than in FCB mode, thus removing more protons from the lattice, which leads to more strain on the crystal structure. Thus, if a crystal structure is stable under battery mode, it is likely also stable under FCB mode.

2.2. Experimental

All chemicals used in the current study were of analytical grade and used without further purification. Different MnO_2 structures were obtained via a redox method according to the following reaction [77]:

$$2NaMnO_4 + 3MnSO_4 + 2H_2O \rightarrow 5MnO_2 + Na_2SO_4 + 2H_2SO_4. \quad (2.1)$$

In a typical synthesis, 50 mL of 0.08 M $NaMnO_4$ (Sigma-Aldrich, USA) were mixed under stirring with 50 mL of 0.12 M $MnSO_4 \cdot 5H_2O$ (Kanto Chemical, Japan), and then heated either in a beaker (if synthesis temperature ≤90°C) or a Teflon-sealed autoclave (if synthesis temperature ≥120°C). The manganese of the permanganate was thereby reduced from the septivalent to the tetravalent state, while the manganese ion of manganese sulfate was oxidized from the divalent to the tetravalent state. Thus, the molar ratio of $NaMnO_4$:$MnSO_4$ used in this method was chosen at 2:3 to balance the valence during the reaction (2.1). Potassium chloride (KCl, Wako Pure Chemical Industries, Japan) was also added to the mixture, with contents varying from 0 M to 10 M, to analyze the effects of the potassium ion concentration on the system. Furthermore, the effects of temperature were analyzed at a range between 60°C and 160°C. The synthesis time was 1 h for temperatures ≤90°C and 3 h for temperatures ≥120°C.

The reason for using different synthesis times is because the two different reaction vessels required different times to heat up. In beakers, the reaction needed 1 h to be completed, which was indicated by the disappearance of the red color in the solution coming from the permanganate. For samples synthesized in autoclaves, the reaction time had to be increased to 3 h because of the heat-up time of the autoclave in air. A summary of all compositions analyzed herein is shown in Table 2.1. After synthesis, the samples were filtered three times with distilled water and dried for 24 h at 80°C in air.

Table 2.1: Overview of synthesis conditions of all experiments.

	Mn-source				
#	Oxidant	Reductant	Synthesis temp. [°C] (synthesis time [h])	KCl addition [mol/L]	Crystalloid structure
1	$NaMnO_4$	Mn_2SO_4	60 (1)	0	γ
2	$NaMnO_4$	Mn_2SO_4	60 (1)	0.1	δ
3	$NaMnO_4$	Mn_2SO_4	60 (1)	0.2	δ
4	$NaMnO_4$	Mn_2SO_4	60 (1)	1	δ
5	$NaMnO_4$	Mn_2SO_4	60 (1)	10	δ
6	$NaMnO_4$	Mn_2SO_4	90 (1)	0	γ
7	$NaMnO_4$	Mn_2SO_4	90 (1)	0.1	γ
8	$NaMnO_4$	Mn_2SO_4	90 (1)	0.2	γ
9	$NaMnO_4$	Mn_2SO_4	90 (1)	0.5	γ/α
10	$NaMnO_4$	Mn_2SO_4	90 (1)	1	δ
11	$NaMnO_4$	Mn_2SO_4	90 (1)	2	δ
12	$NaMnO_4$	Mn_2SO_4	90 (1)	10	δ
13	$NaMnO_4$	Mn_2SO_4	120 (3)	0	γ
13-2	$KMnO_4$	Mn_2SO_4	120 (3)	0	α
14	$NaMnO_4$	Mn_2SO_4	120 (3)	0.02	γ/α
15	$NaMnO_4$	Mn_2SO_4	120 (3)	0.05	α
16	$NaMnO_4$	Mn_2SO_4	120 (3)	0.2	α
17	$NaMnO_4$	Mn_2SO_4	120 (3)	1	α
18	$NaMnO_4$	Mn_2SO_4	120 (3)	10	α
19	$NaMnO_4$	Mn_2SO_4	160 (3)	0	β
20	$NaMnO_4$	Mn_2SO_4	160 (3)	0.02	β/α
21	$NaMnO_4$	Mn_2SO_4	160 (3)	0.05	α
22	$NaMnO_4$	Mn_2SO_4	160 (3)	0.2	α
23	$NaMnO_4$	Mn_2SO_4	160 (3)	1	α
24	$NaMnO_4$	Mn_2SO_4	160 (3)	10	α
25	$KMnO_4$	$MnCl_2$	4 (24)	NaOH: 0.3	δ

In the following sections, to distinguish the different samples and establish a consistent nomenclature, the name of the compound consists of the crystal structure followed by the synthesis temperature in °C, synthesis time in hours, and KCl concentration in mol/L. For example, 'α 120-3-0.2' refers to α-MnO_2 synthesized at 120°C for 3 h with 0.2 M KCl. The only exceptions from this nomenclature are commercial materials and δ-cold, which was synthesized according to an alternate redox method [78]. In this case, a 0.112 M $MnCl_2 \cdot 4H_2O$ solution was slowly mixed with a 0.3 M NaOH and 0.1 M $KMnO_4$ solution in an ice bath and aged for 1 d at room temperature.

Electrolytic γ-MnO_2 manganese dioxide (EMD, Tosoh Corp., Japan) was used as received. λ-MnO_2 was obtained by chemical delithiation of $LiMn_2O_4$ (BET surface area: 0.4 m^2/g, Mitsui Kinzoku, Japan) in a 0.1 M nitric acid solution for 24 h under stirring [46]. This treatment removed the lithium ions from the crystal lattice of the $LiMn_2O_4$ without damaging its spinel structure. Typically, ca. 10% of the initial Li ions remain within the lattice [46]. Slurries of the active materials were prepared by mixing carbon black (CB, 50 nm diameter, Mitsubishi Chemical, Japan) and MnO_2 with ethylene-vinyl acetate (EVA, Tosoh Corp.) in ca. 100°C xylene solution at a weight ratio of MnO_2:CB:EVA = 100:15:10. The slurry was pasted onto a 500-µm-thick nickel foam, dried in air at room temperature for 24 h, and pressed at 40 MPa to obtain 2 cm × 4 cm-sized electrodes. The MnO_2 loading of all samples was between 12 and 16 mg/cm^2. Three-electrode cells were assembled with the active electrode, a nickel foam counter electrode, and an Hg/HgO reference electrode. A porous 120-µm-thick polypropylene sheet and a 6-M KOH solution were used as separator and electrolyte, respectively.

The crystal structures of the MnO_2 samples were analyzed using an X-ray diffractometer (XRD; Cu Kα radiation, XRD Miniflex, Rigaku Corp., Japan). The diffraction patterns were

measured between θ/2θ = 10° and 80°. Scanning electron microscopy (SEM; Tabletop Microscope TM3030, Hitachi-Hitec, Japan) was used to further characterize the morphology of the samples. The average specific surface area of the MnO_2 samples was determined by the Brunauer–Emmett–Teller (BET) nitrogen adsorption method (Belsorp-max, BEL Japan). Electrochemical tests, namely cyclic voltammetry (CV) and galvanostatic charge/discharge analysis, were conducted with a galvanostat/potentiostat (Analytical 1480 Multistat, Solartron) at 25°C. See Appendix B for more details about measurement techniques.

2.3. Results and Discussion

2.3.1. Crystal Structure and Morphology Analysis

After synthesis, samples were analyzed by XRD. It was found that pure crystal structures of four different MnO_2 materials, i.e., α-, β-, γ-, and δ-MnO_2, could be obtained simply by varying the synthesis temperature and KCl content of the redox method. This highlights the usefulness of redox synthesis to obtain various MnO_2 compounds. The different crystal structures were obtained simply by changing the two main parameters described.

The effect of synthesis condition – K ion concentration and temperature – on the crystal structure is summarized in Fig. 2.1. This phase diagram gives an overview of the influence of (a) KCl concentration and (b) temperature on the synthesized crystal structure. At low or no KCl concentration β- or γ-MnO_2 were synthesized, while at higher KCl concentration α- or δ-MnO_2 were synthesized. By altering the synthesis temperature, the structure could be further influenced, with syntheses at low temperatures resulting in γ- or δ-MnO_2 and high temperatures resulting in α- or β-MnO_2.

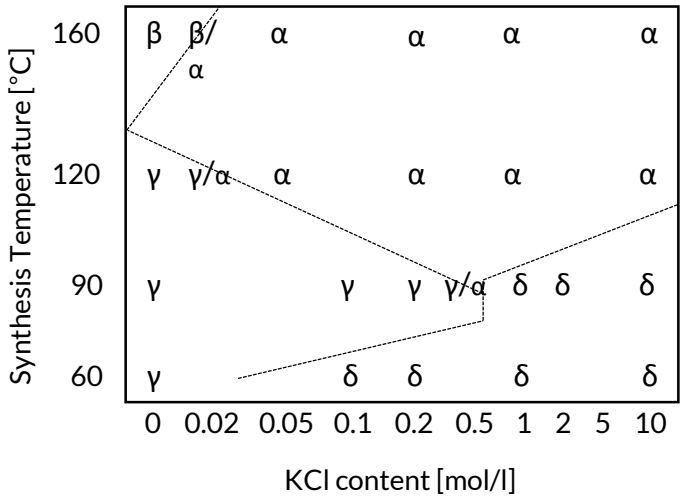

Fig. 2.1: MnO_2 crystal structure phase diagram with KCl content and synthesis temperature as variables.

Fig. 2.1 confirms the ability of KCl to influence the MnO_2 crystal structure during synthesis, as shown in the introduction. However, the templating capability is by no means restricted to K ions but can also be translated to Na ions. Because of the smaller size of Na ions (116 pm for Na^+ vs. 152 pm for K^+ [79]), it is expected that their influence on the crystal formation is lessened. To prove this expectation, MnO_2 was synthesized in a similar manner to the reaction shown in eq. (2.1), but with $KMnO_4$ used as the oxidant instead of $NaMnO_4$ (sample #13-2 in Table 2.1). At a synthesis temperature of 120°C and no KCl addition, the XRD results, shown in Fig. 2.2, reveal an α-structure for this composition – in contrast to γ-MnO_2 when $NaMnO_4$ is used as the oxidant. Nevertheless, despite the presence of Na ions, the densest MnO_2 structure, i.e., β-MnO_2, could be obtained by increasing the synthesis temperature to a sufficiently high level.

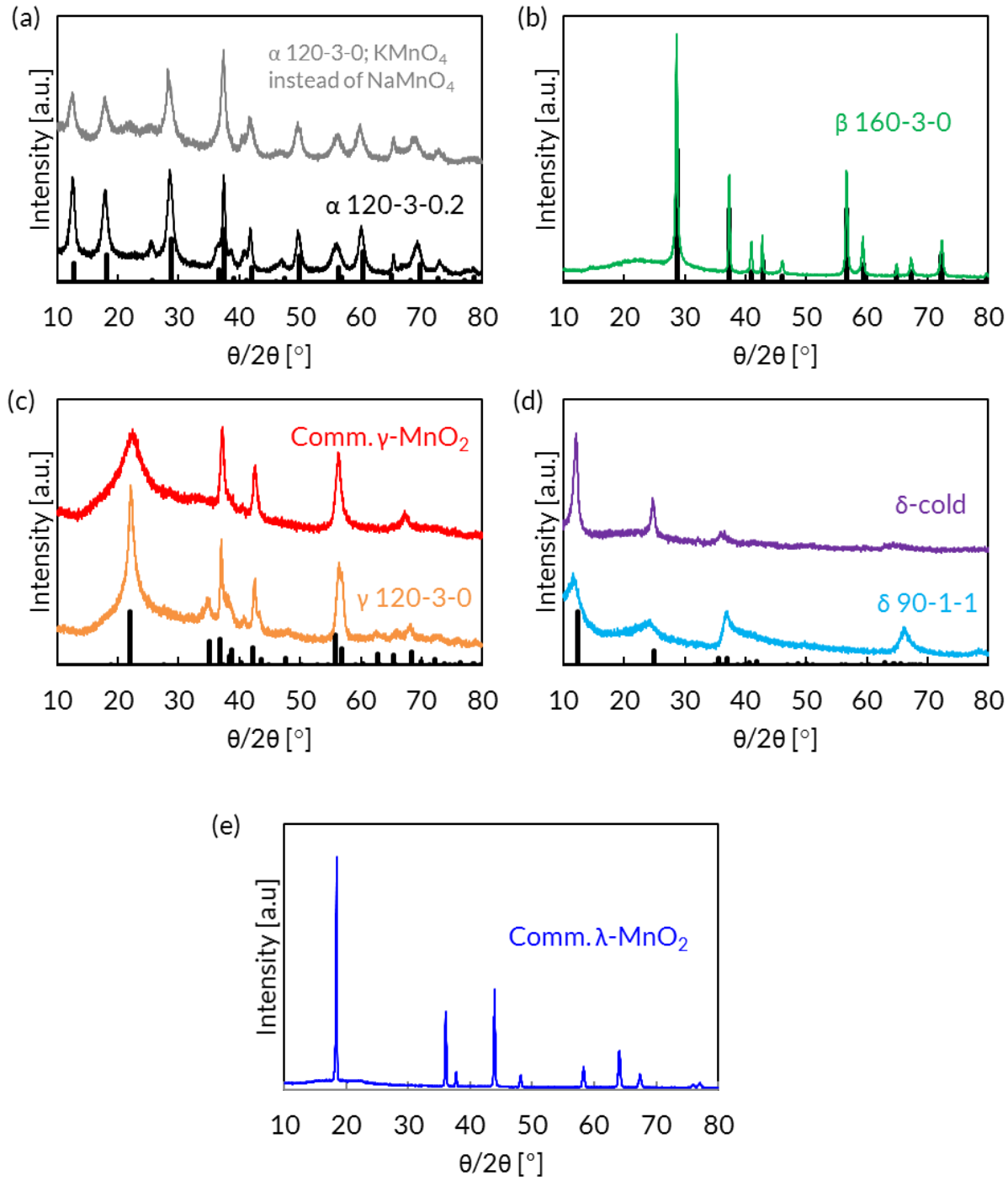

Fig. 2.2: XRD patterns of various MnO_2 samples with corresponding powder diffraction files. a) α-MnO_2 with JCPDS 44-141, b) β-MnO_2 with JCPDS No. 24-0735, c) γ-MnO_2 compounds with JCPDS No. 44-142, and d) δ-MnO_2 compounds with JCPDS No. 43-1456, e) commercial λ-MnO_2.

This leads to a second observation. At higher temperatures denser structures were synthesized, which was also found by others with a hydrothermal-electrochemical method [80]. It is expected that this is due to thermodynamic reasons, where at higher temperatures the

balance seems to shift toward denser structures. It is hypothesized that at high temperatures, large void spaces cannot be sustained and break into denser structures. This is achieved at comparatively low temperatures during synthesis and requires higher temperatures if the crystal structure is already formed. As such, other studies have shown phase change during thermogravimetric analysis, where γ-MnO_2 was shown to be transformed into β-MnO_2 at 210–280°C [81] or δ-MnO_2 into α-MnO_2 at 470°C [82]. Overall, the synthesized products could be well reproduced. Only at syntheses around 90°C and 1 M KCl, i.e. at the boundary between the synthesis of α-, γ-, and δ-MnO_2, small changes in temperature could change the resulting structure. For example, at too high temperatures (ca. 95°C), instead of δ-MnO_2, α-MnO_2 was synthesized.

Representative XRD patterns of all five crystal structures are plotted in Fig. 2.2 by means of seven samples. Pure α-MnO_2 was obtained at a synthesis temperature of 120°C with 0.2 M KCl or by replacing $NaMnO_4$ with $KMnO_4$ and no KCl addition. Highly crystalline β-MnO_2 was obtained at 160°C without KCl addition. With the same solution but by lowering the temperature to 120°C, γ-MnO_2 was obtained rather than β-MnO_2. The synthesized material was compared with commercial γ-MnO_2, which proves the γ-structure of the latter and also highlights the improved crystallinity of the herein synthesized γ-MnO_2. MnO_2 synthesized at 90°C with the addition of 1 M KCl showed all peaks that correspond to δ-MnO_2, with an additional peak at 58°, which could not be allocated to another material. Thus, another method to synthesize δ-MnO_2 was used to obtain pure phase δ-MnO_2, which also served as the reference material in electrochemical testing.

For SEM analysis, seven samples were chosen. α-MnO_2 120-3-0.2, β-MnO_2 160-3-0, γ-MnO_2 120-3-0, and δ-MnO_2-cold were chosen because they showed intense peaks by XRD

analysis and required no or little amounts of KCl to be added. δ-MnO_2 90-1-1, and commercial γ-MnO_2 were also analyzed with SEM as they were chosen as a reference in electrochemical analysis. In addition, the SEM of λ-MnO_2 is shown. The SEM images of the seven samples are shown in Fig. 2.3. A direct correlation between synthesis temperature and particle size was observed. At elevated synthesis temperatures in autoclaves, rod- and needle-like structures were obtained, whereas at lower temperatures, larger particles were obtained. α-MnO_2 120-3-0.2, β-MnO_2 160-3-0, and γ-MnO_2 120-3-0 are a few micrometer-long needles/rods that are a few tens of nanometers wide. One-dimensional shapes are frequently found in hydrothermal MnO_2 syntheses [34,83,84] and the resulting shape is claimed to be obtained because of a spontaneous and preferential process dependent on reaction conditions [85]. δ-MnO_2 90-1-1 resulted in particle sizes of up to a few micrometers, which is slightly larger than commercial γ-MnO_2. Synthesis of δ-MnO_2-cold resulted in very large particles, which had to be ground carefully before electrochemical analysis. λ-MnO_2 consisted of fairly well shaped octahedral with similar particle sizes to commercial γ-MnO_2.

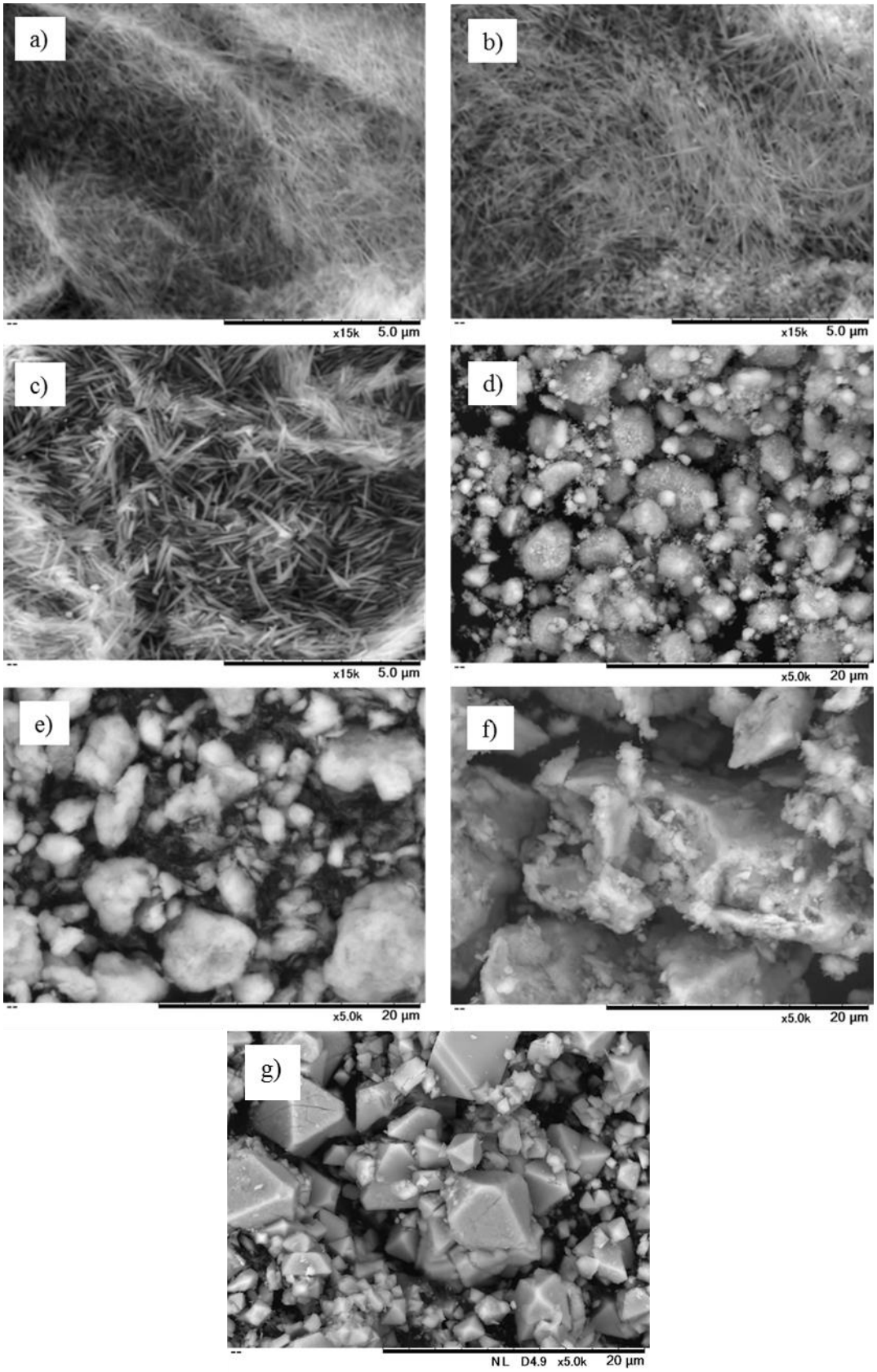

Fig. 2.3: SEM images of a) α-MnO_2 120-3-0.2 b) β-MnO_2 160-3-0, c) γ-MnO_2 120-3-0, d) commercial γ-MnO_2 (Tosoh), e) δ-MnO_2 90-1-1, and f) δ-MnO_2-cold. Magnification is 15,000× for a), b), and c) and 5,000× for d), e), and f).

The surface area, pore volume, and average pore diameter of the seven samples were measured with BET. First, 0.2 g of each sample was heated to 200°C for 6 h to remove any organic impurities. Surface measurement was done with high purity nitrogen as adsorbate gas at -196°C and details about the surface area were obtained by plotting p/p_0 versus $p/(V_a \cdot p - V_a)$. Thereby, p is the partial vapor pressure of nitrogen gas in Pascale, p_0 the saturated pressure of nitrogen gas in Pascale, and V_a the volume of gas adsorbed at 0°C and 1.013×10^5 Pa in milliliters. Points between $p/p_0 = 0.05$ and 0.3 were used for linearization and for all samples the linear regression was below 0.9975.

The results are summarized in Table 2.2. It was found that the needle- or rod-like structure did not necessarily result in a higher surface area. Instead, the highest surface area was found in δ-MnO_2 90-1-1, which can be ascribed to a combination of large pore volume and low average pore diameter. It was found that to increase the surface area, syntheses at lower temperatures and higher K ion concentration are preferred. The only exception to this was for δ-MnO_2, which had a small surface area and pore volume.

Table 2.2: BET surface area of selected compounds.

Compound	Surface area [m^2/g]	Pore volume [cm^3/g]	Average pore diameter [nm]
α 120-3-0.2	68.5	0.6343	37.02
β 160-3-0	27.3	0.2086	50.57
γ 120-3-0	41.7	0.5010	48.10
Comm. γ-MnO_2	51.5	0.1384	10.75
δ 90-1-1	93.9	0.6227	26.54
δ cold	31.8	0.0927	11.68
Comm. λ-MnO_2	14.5	0.0120	2.86

2.3.2. Electrochemical Characterization

To assess the capabilities of all samples as possible positive electrode materials in FCB systems, the seven samples were analyzed for their electrochemical performance. The pasted electrodes were first analyzed with linear sweep voltammetry from open circuit potential to −1.0 V vs. Hg/HgO. The discharge cut-off potential for life cycle testing was defined based on these results. All samples were then cycled for 31 cycles to further compare the different compounds. As an initial step, the maximum capacity was identified by discharging at 30.8 mA/g – which corresponds to a 0.1 C rate based on their maximum theoretical capacity of 308 mAh/g (one-electron reduction reaction of MnO_2). Then, the samples were cycled at 0.2 C based on their first discharge capacity 30 times.

Linear sweep voltammetry was conducted to identify the potential of the reduction peak of all samples according to eq. (2.2):

$$MnO_2 + H_2O + e^- \rightarrow MnOOH + OH^-. \qquad (2.2)$$

Fig. 2.4 highlights that the reduction peak differed considerably among the compounds. α-MnO_2 120-3-0.2 showed the most intense peaks at a potential of approximately −0.4 V vs. Hg/HgO. The highest potential is found in commercial λ-MnO_2 with a curve reaching its peak at −0.16 V vs. Hg/HgO. The lowest peak, both in terms of intensity and potential, was found in β-MnO_2 160-3-0, with its maximum at a potential of −0.45 V vs. Hg/HgO. Based on these results, the cut-off potential was chosen at −0.5 V vs. Hg/HgO for all samples to ensure complete discharge while minimizing unnecessary over-discharge.

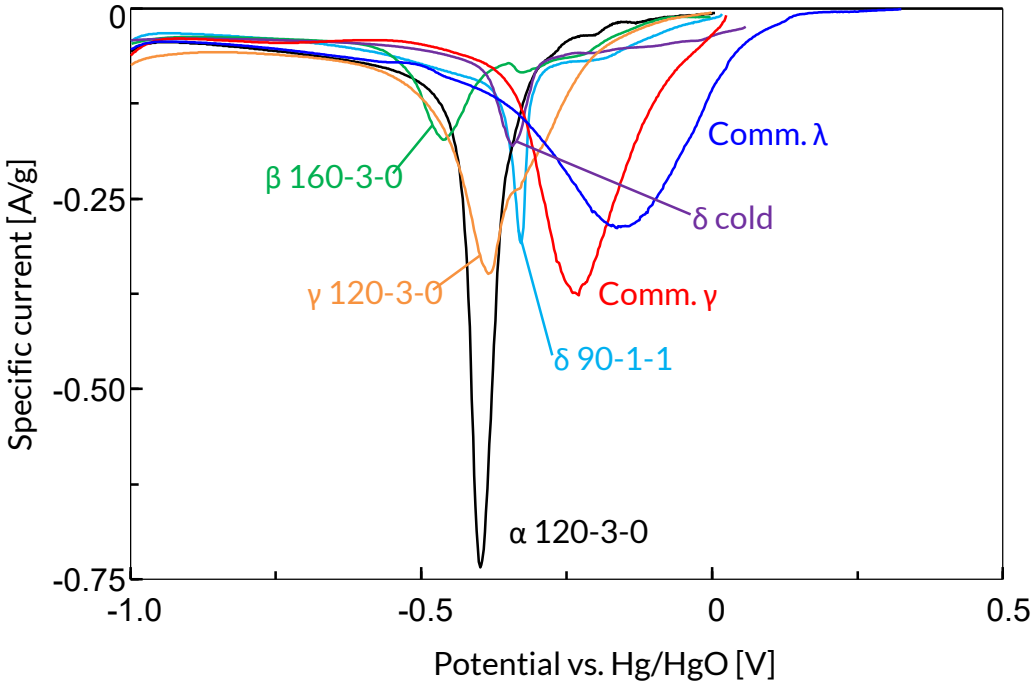

Fig. 2.4: Linear sweep voltammetry of different materials at 0.1mV/s from open circuit to -1.0 V vs. Hg/HgO

The results of the first discharge curve, shown in Fig. 2.5, mirrored the findings of the linear sweep voltammetry. α-MnO_2 120-3-0.2 showed a very stable discharge potential during the first discharge. It also featured the highest capacity (341 mAh/g), which is higher than its theoretical maximum of 308 mAh/g. This difference is expected to be due to the creation of Mn_3O_4, as shown in the last part of this section. Commercial γ-MnO_2 and γ-MnO_2 120-3-0 also featured relatively high discharge capacities with 93.1% and 80.2%, respectively, of their theoretical maximum. Their discharge profile offered a less stable plateau but did provide a constantly decreasing potential during discharge. Also, this finding goes hand in hand with the linear sweep voltammetry analysis, where broader peaks were found for γ-compounds. In contrast to α- and γ-MnO_2, both β- and δ-MnO_2 compounds revealed rather low discharge capacities with values between 119 and 166 mAh/g. Commercial λ-MnO_2 showed an average capacity among all samples of 200 mAh/g.

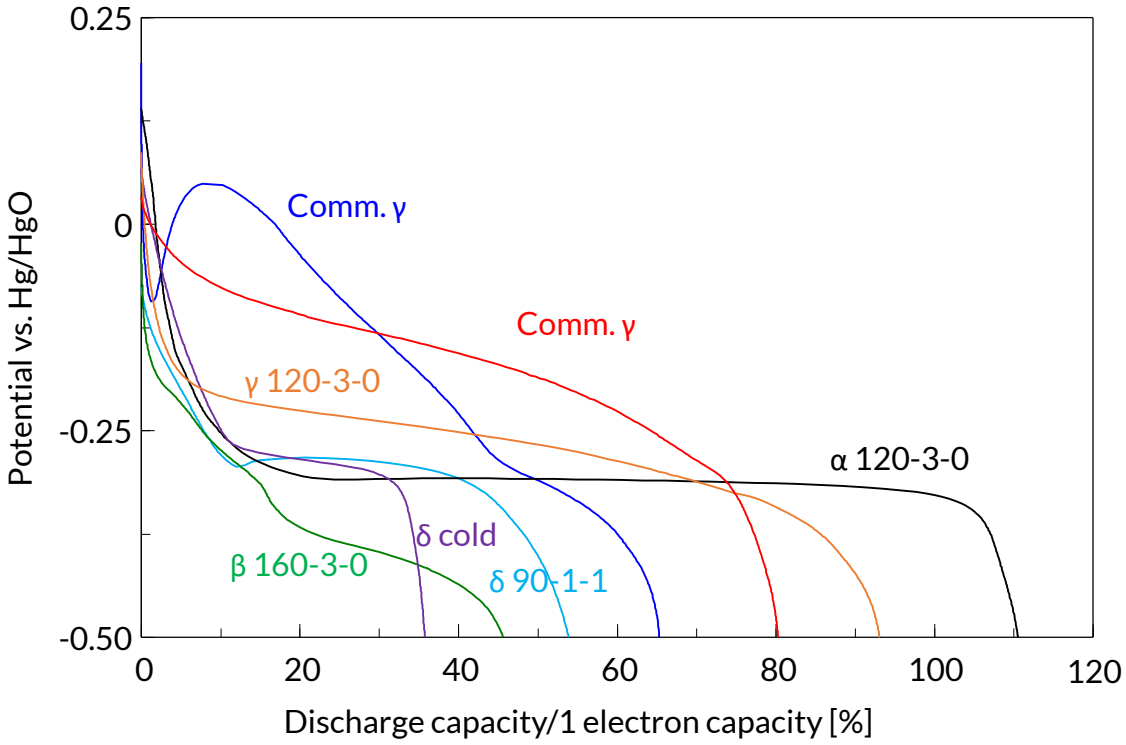

Fig. 2.5: 1st discharge curves of various compounds.

From these results, the crystal structure was found to have a strong effect on the initial discharge capacity, but also the particle shape has a substantial effect on the capacity usage. The particles in δ-MnO_2 cold were the largest among the samples analyzed in this work and the same material showed the lowest discharge capacity. The reason for the poor capacity utilization is expected to be due to the poor proton diffusion and possibly low electronic conductivity of MnO_2.

Also the particle shape was found to affect the results. γ-MnO_2 120-3-0 and commercial γ-MnO_2 have a similar crystal structure, as shown in Fig. 2.2 (c), but the former shows a much lower discharge voltage. In order to find a possible explanation for this behavior, electrochemical impedance spectroscopy was conducted and SEM images of the pasted electrodes were taken. In Fig. 2.6 (a), it can be seen that γ-MnO_2 120-3-0 had a considerably larger impedance compared to commercial γ-MnO_2. The reason for this difference is likely to

be due to difficulties in dispersing the slurries homogenously. The SEM image in Fig. 2.6 (b) shows conglomeration of MnO_2+CB+EVA when rod-type γ-MnO_2 120-3-0 was used. Similar conglomeration was found with all rod/needle shaped MnO_2 compounds and are likely to cause the higher impedance due to poor interconnection of the network. In contrast to that, more spherically shaped particles led to a homogenous dispersion, as shown representatively for commercial γ-MnO_2 in Fig. 2.6 (c). This explains the lower impedance of commercial γ-MnO_2 and thus higher discharge potential compared to γ-MnO_2 120-3-0. Hence, it can be concluded that nano-rod/needle-like structures are unsuitable for the type of electrodes used in this work.

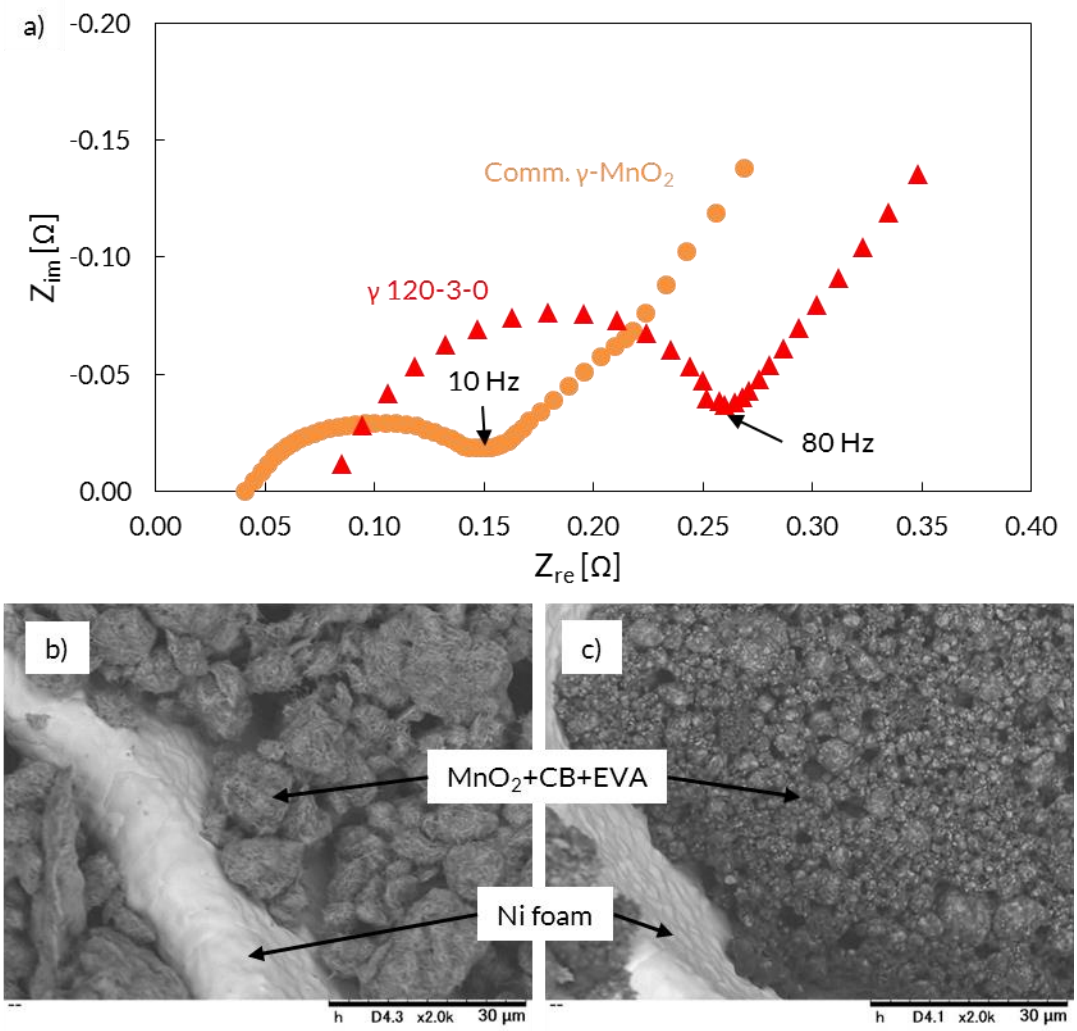

Fig. 2.6: (a) Nyquist plots of commercial γ-MnO_2 and γ-MnO_2 120-3-0. SEM images of pasted (b) γ-MnO_2 120-3-0 and (c) commercial γ-MnO_2 on nickel foam.

After the first discharge, all compounds were cycled at 0.2 C – based on the discharge capacity of the first discharge – with cut-off potentials at −0.5 V vs. Hg/HgO and +0.5 V vs. Hg/HgO for discharge and charge, respectively. The lower cut-off potential was chosen according to linear sweep voltammetry analysis. At −0.5 V vs. Hg/HgO the major amount of active MnO_2 was expected to be reduced while simultaneously limiting the creation of electrochemically stable (i.e., non-rechargeable) structures [86]. During charge, a cut-off potential was implemented to limit phase transformation and oxygen evolution reaction (OER) according to the following equation:

$$4OH^- \rightarrow O_2 + 2H_2O + 4e^-. \quad (2.3)$$

The results of the cycle performance are summarized in Fig. 2.7. α-MnO_2 120-3-0.2, which showed a very promising first discharge, was very poorly cyclable, similar to observations from other studies [87]. It lost almost its entire capacity after the first discharge cycle and could afterwards be cycled only at a very low level, well below 20 mAh/g. β-MnO_2 160-3-0 also lost capacity between the first and second cycle but hit its minimum after three cycles on a considerably higher level than α-MnO_2 120-3-0.2. In addition, it afterwards continuously increased its capacity, which is assumed to be due to a steadily increased amount of activated MnO_2. After 31 cycles, the capacity leveled off at around 78 mAh/g. Commercial γ-MnO_2 was the only compound for which only a small capacity loss between the first two cycles was observed. However, both commercial γ-MnO_2 and γ-MnO_2 120-3-0 were steadily losing capacity as the cycle number increased and were the only two compounds with a continuously downward trending curve. Nevertheless, after 31 cycles, they still offered the highest capacities. Similar to α- and β-MnO_2, both δ-compounds experienced a considerable drop in capacity in the first few cycles but then stabilized at around 40 mAh/g. Commercial λ-MnO_2 was found to lose a considerable amount capacity during the first few cycles (which was shown in the

previous chapter to be due to partial transformation into δ-MnO_2), but later the capacity loss per cycle was very similar to that of commercial γ-MnO_2 and γ-MnO_2 120-3-0, indicating a similar stability.

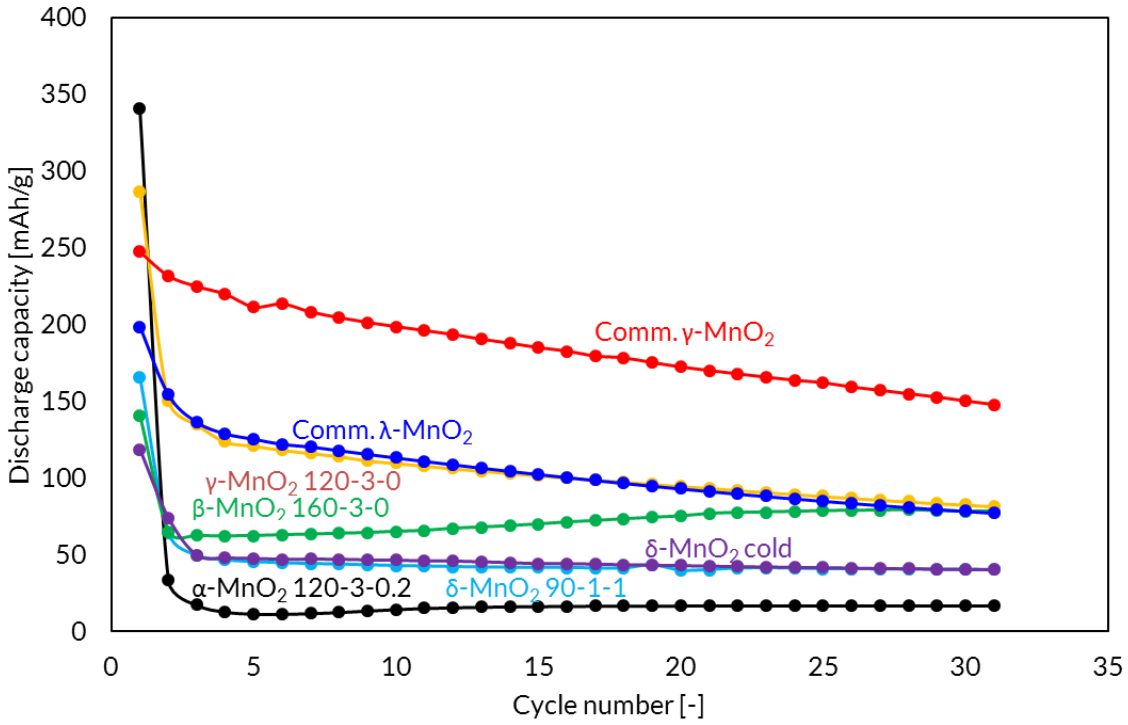

Fig. 2.7: Discharge capacity and capacity retention of various compounds during first 31 cycles. ×: α-MnO2 120-3-0.2; ●: Comm. γ-MnO_2; ▲: γ-MnO2 120-3-0; +: β-MnO2 160-3-0; ■: δ-cold; ♦: δ-MnO2 90-1-1

These results show that the life cycle performance primarily depends on the crystal structure rather than morphology. δ-cold and δ-MnO_2 90-1-1 were found to have the lowest and highest surface area, respectively, yet they show very similar capacity retention from the third cycle onwards. Similarly, the capacity of commercial γ-MnO_2 and γ-MnO_2 120-3-0 both steadily faded during cycling, even though their particle shape was very different. In contrast, α-MnO_2 120-3-0.2, β-MnO_2 160-3-0, and γ-MnO_2 120-3-0, all of which showed similar morphologies, had very different behaviors during cycling.

To identify the reasons for capacity loss, after the 31 cycles the samples were first recharged at 0.2 C until a cut-off potential of 0.5 V vs. Hg/HgO and then analyzed with XRD. The results are shown in Fig. 2.8. α-MnO_2 120-3-0.2 showed the most significant crystal change with complete transformation into δ-MnO_2 and Mn_3O_4. The presence of the latter explains why α-MnO_2 120-3-0.2 showed a very high initial discharge. In Mn_3O_4, the manganese is in its secondary and tertiary oxidation state, thus indicating an over-discharge. Additionally, Mn_3O_4 is known to not be cyclable in an alkaline environment [53], hence explaining the poor cyclability of α-MnO_2 120-3-0.2.

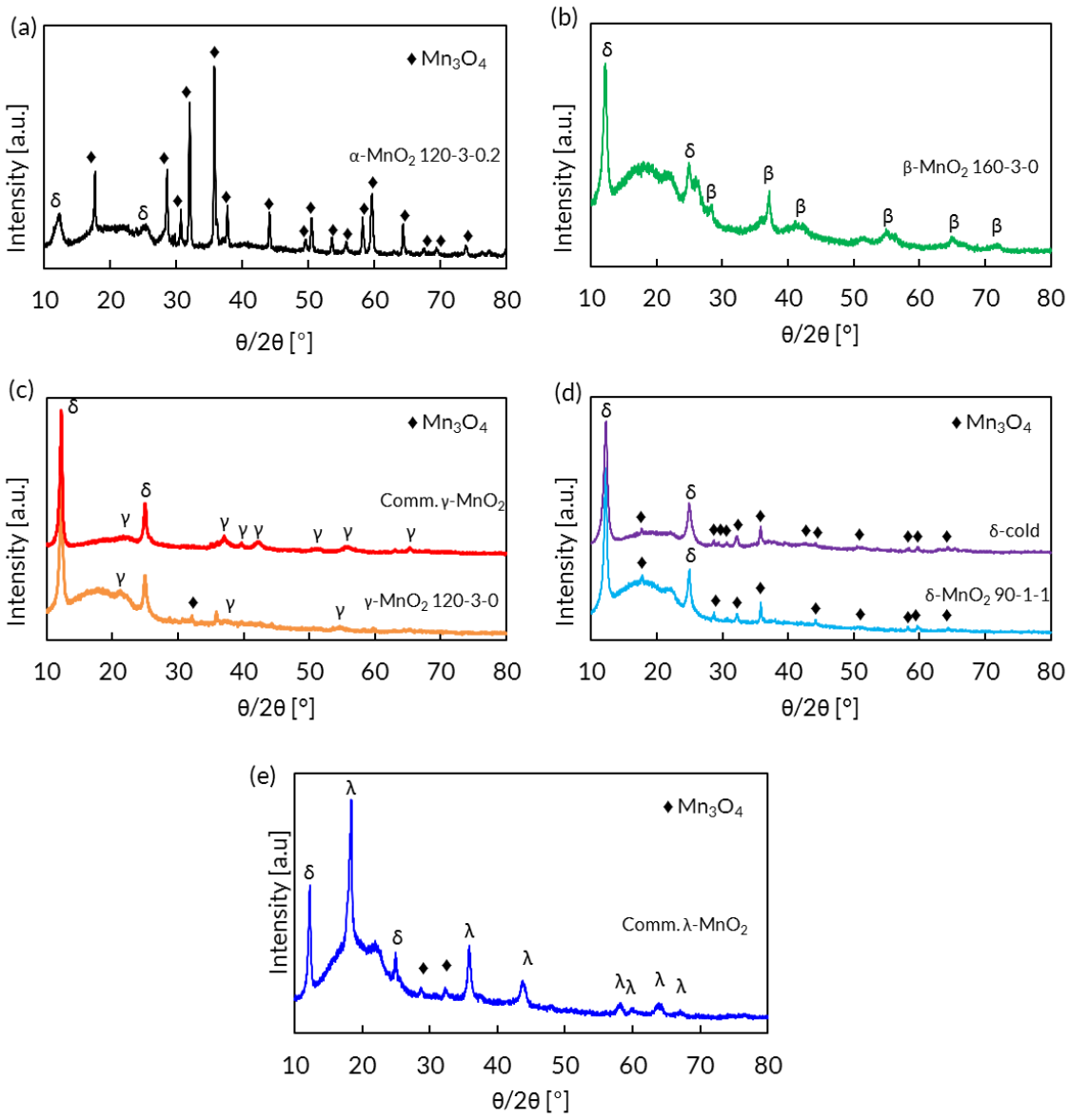

Fig. 2.8: XRD spectra of samples after cycling. a) α-MnO_2 120-3-0.2, b) β-MnO_2 160-3-0, c) Comm. γ-MnO_2 and γ-MnO_2 120-3-0, d) δ-cold and δ-MnO_2 90-1-1, e) comm. λ-MnO_2.

β-MnO_2 also showed transformation into δ-MnO_2, but no Mn_3O_4 could be identified. Additionally, in contrast to α-MnO_2, XRD analysis after cycling still showed clearly visible peaks belonging to its initial phase, i.e., β-MnO_2. Similar observations were made with γ-MnO_2, but the peaks corresponding to δ-MnO_2 were considerably stronger than γ-MnO_2, indicating a more advanced crystal transformation. Furthermore, slight Mn_3O_4 peaks could be identified. In δ-MnO_2, besides peaks belonging to δ-MnO_2, traces of Mn_3O_4 were found, thus explaining its slow but steady degradation. In case of commercial λ-MnO_2, considerable amounts transformed into δ-MnO_2 and traces of Mn_3O_4 were also observed. However, the initial structure was still clearly visible, indicating a higher stability compared to commercial γ-MnO_2.

Based on these findings, a mechanism for how the morphology of manganese oxide compounds changes during cycling is proposed. A schematic summary is shown in Fig. 2.9. The poor cycling performance of α-MnO_2 is ascribed to the formation of electrochemically stable Mn_3O_4, and the remaining capacity measured after the second cycle is ascribed to the formation of δ-MnO_2. δ-MnO_2 is shown to be cyclable, but with a relatively low capacity compared with its theoretical maximum. It also showed transformation into Mn_3O_4, but at a considerably slower rate than for α-MnO_2, Furthermore, visual observations of the electrodes after cycling showed an intense wash-off of the electroactive material of δ-MnO_2 electrodes. It is suggested that the layered structure expands and shrinks during cycling, which results in disintegration of the MnO_2+CB+EVA mixture. The loss in capacity of γ-MnO_2 could be attributed to transformation into δ-MnO_2 and a similar process occurs with β-MnO_2, but at a slower pace. Also λ-MnO_2 transforms into δ-MnO_2 but at a yet slower rate than β-MnO_2.

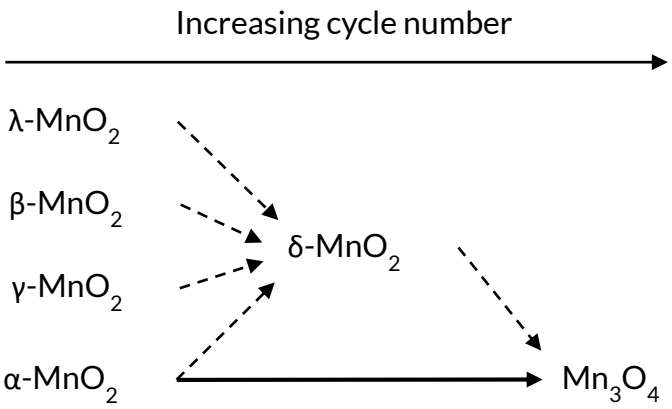

Fig. 2.9: Proposed crystalline structure change of different MnO_2 structures during cycling in alkaline media between -0.5 V vs. Hg/HgO and 0.5 V vs. Hg/HgO.

2.4. Conclusion

In this work, different MnO_2 crystal structures were successfully synthesized via a redox method. By altering synthesis temperature and K ion concentration, MnO_2 with different tunnel structures were systematically synthesized. It is concluded that the large K ions work as templates during the redox reaction between the peroxide and manganese ions. With high K content, MnO_2 compounds with large tunnel structures can be obtained. The reverse was observed by increasing the synthesis temperature. It is assumed that at high synthesis temperatures, denser compounds were created because of thermodynamic balance.

The samples were analyzed with different methods, mainly focusing on electrochemical studies. Several conclusions can be made:

- On a one-discharge basis, the capabilities of the different crystal structures decrease according to: $\alpha > \gamma > \lambda > \delta \approx \beta$
- In terms of cyclability, α-MnO_2 shows the poorest performance, with a high capacity fading after first discharge. The highest capacity is found in γ-compounds, although they suffer from constant fading. The main reason for capacity loss is expected to be the creation of Mn_3O_4.

Henceforth, the focus is set on γ- and λ-MnO_2 as possible materials for positive electrode in FCB systems as these materials show the best stability. A better stability is beneficial for durability and it also allows for an easier analysis in the forthcoming chapters, as the effect of a transformation into other manganese oxides (such as Mn_3O_4) does not need to be considered.

Chapter 3 Chemical Charging Mechanism of MnO_2 with Oxygen

Abstract

Two different crystal structures, i.e. γ-MnO_2 and λ-MnO_2 were used to analyze the chemical charge mechanism of discharged MnOOH with oxygen in alkaline electrolyte. Highly pressurized oxygen gas dissolved in electrolyte was used to charge MnOOH. The resulting chemical charge curves were compared with the electrochemical charge curves in order to identify how the chemical charge rate changed within one hour. For both electrodes, three distinct stages could be observed. Stage one was dominated by the dissolution and adsorption of oxygen on the electroactive material. In the second stage, surface MnOOH was charged which could be confirmed by a constant charge rate. In the last stage, the charge rate decreased which is proposed to be due to proton diffusion limitations.

3.1. Introduction

A simplified chemical charging mechanism of the positive electrode with oxygen is shown in Fig. 3.1. In the first step, dissolved oxygen in the electrolyte diffuses to and adsorbs rapidly at the surface of the MnOOH particles [23,66]. In the second step, surface MnOOH is charged with the adsorbed oxygen to form MnO_2 and H_2O. Finally, in the third step, proton diffusion from the bulk to the surface takes in order to charge the bulk of the particles [23,88].

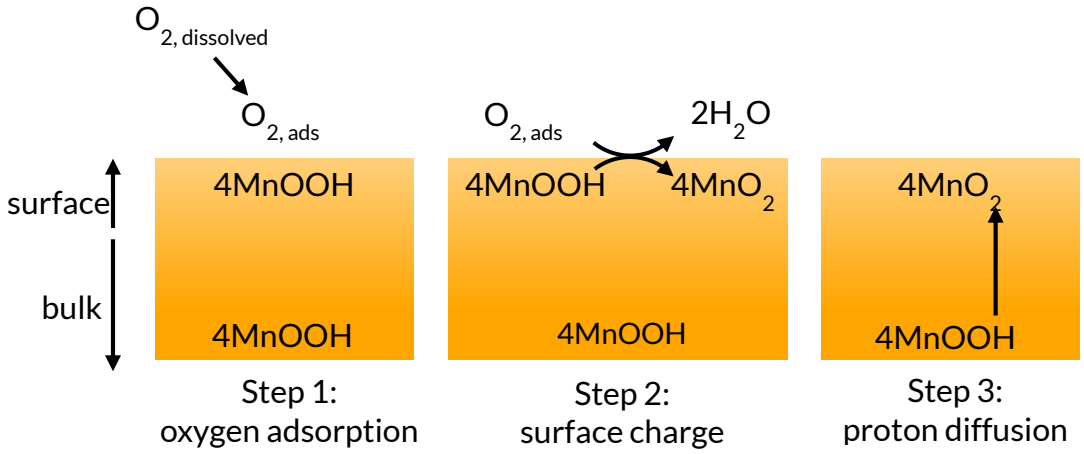

Fig. 3.1: Three stages of chemical oxygen charging of MnOOH

However, there are still several unknowns, such as how exactly the surface oxidation mechanism works and what the rate limiting step is. Two different samples, namely γ-MnO_2 and λ-MnO_2 were chosen in this chapter. To allow for more information about the charge mechanism, the data acquisition method was improved compared to previous work [23]. Instead of focusing on the discharge capacity after different charge times, the potential was measured in real-time during chemical charging.

3.2. Experimental

The same γ- and λ-MnO_2 samples as in the previous chapter were used. The preparation of electrodes and three-electrode cells was done according to the same procedures and characterization was done with the same methods and equipment.

Fig. 3.2 shows the experimental set-up used for chemical charging with oxygen tests. Oxygen was supplied via a tube (0.8 mm diameter) that was inserted close to the active electrode. The set-up enabled the oxygen to be supplied at an elevated pressure (1.0 MPa). The oxygen was supplied at a flow rate of 50 mL/min in all cases.

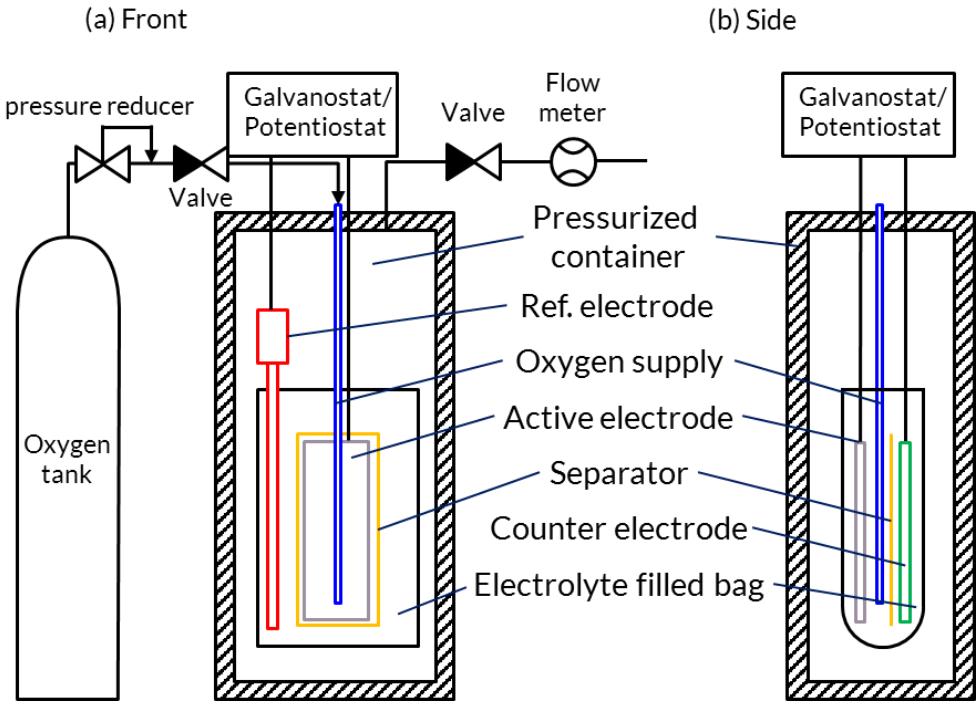

Fig. 3.2: Set-up of pressurized vessel to supply oxygen to sample during regeneration with oxygen and ORR measurement. The side view in (b) only shows the layered assembly of the half-cell

The chemical charging measurement was conducted in three steps. First, γ-MnO_2 and λ-MnO_2 were discharged at 30.8 mA/g (0.1 C) until a potential of -0.4 V vs. Hg/HgO, then kept at open circuit condition for 12 h and finally discharged again at 0.1 C to the same cut-off

potential. By performing this protocol, a complete discharge of both electrodes was assumed. Secondly, the samples were inserted into a pressure vessel to be charged chemically for 1 h with oxygen at a pressure of 1.0 MPa. Lastly, to determine the total amount of regenerated MnO_2, both electrodes were electrochemically discharged in atmospheric conditions at 0.1 C.

3.3. Results and discussion

3.3.1. Physical properties of MnO_2 and cyclic voltammograms

In Fig. 3.3 (a) and (b) the XRD patterns of γ- and λ-MnO_2 are show. All of the peaks of γ- and λ-MnO_2 were found to be present without any impurity peaks. Furthermore, the intensity of the γ-MnO_2 peaks was found to be well below the intensity of those of λ-MnO_2, indicating a higher crystallinity for the latter.

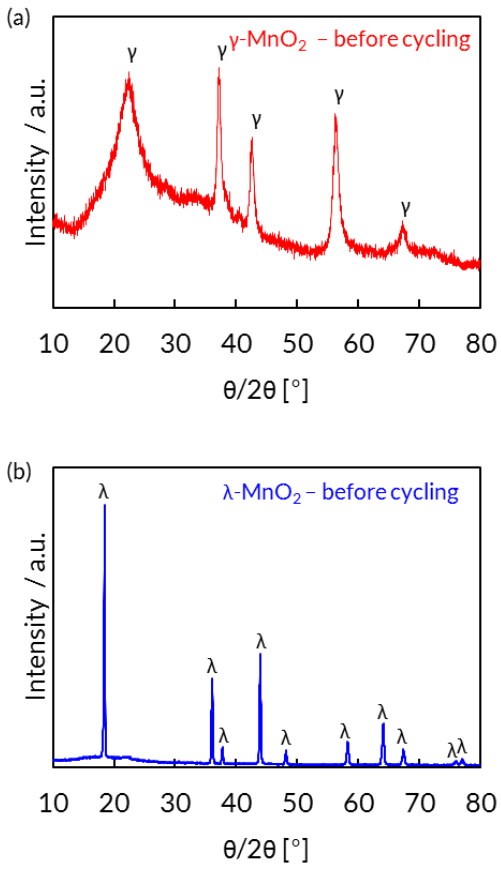

Fig. 3.3: X-ray diffraction patterns of pristine (a) γ-MnO_2 and (b) λ-MnO_2.

The SEM images of the γ- and λ-MnO_2 samples are shown in Fig. 3.4 (a) and (b), respectively. Both the γ- and λ-MnO_2 samples were observed to contain particles of up to several micrometers in diameter. The particles of γ-MnO_2 had various shapes, whereas most of the λ-MnO_2 particles were well-shaped octahedra. The measured BET surface area of the λ-MnO_2 sample (14.5 m^2/g) was lower than that of the γ-MnO_2 sample (51.5 m^2/g). This was caused by the smoother surface of the particles in the λ-MnO_2 sample.

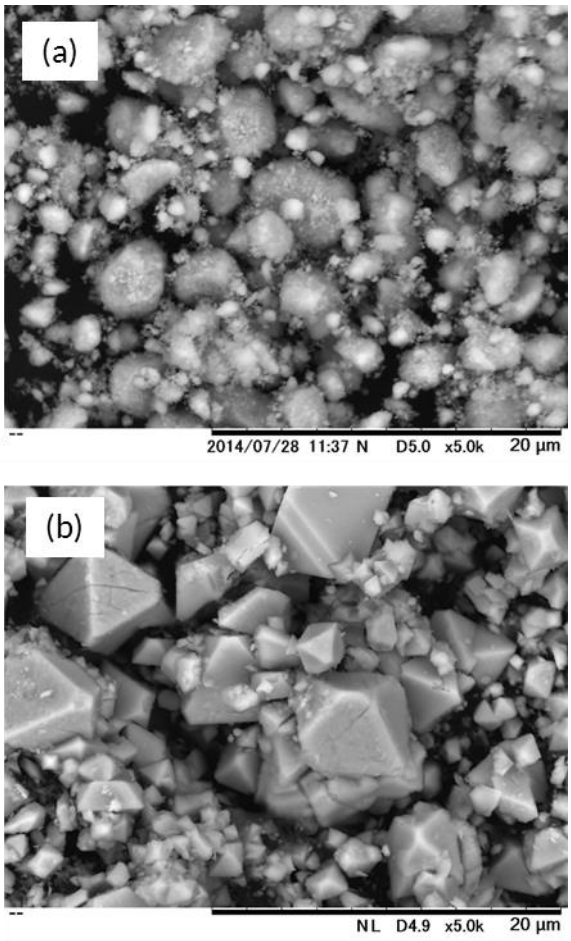

Fig. 3.4: Scanning electron microscopy images of pristine (a) γ-MnO_2 and (b) λ-MnO_2.

The CV curves of γ- and λ-MnO_2 measured at a cycling rate of 0.1 mV/sec for 5 loops between −0.4 V and 0.5 V vs. Hg/HgO are shown in Fig. 5. Both the reduction and oxidation peaks of γ-MnO_2 were observed to become weaker in intensity as the cycle number increased, indicating degradation of the γ-MnO_2. Furthermore, in case of γ-MnO_2, two oxidation and

reduction peaks were observed which may be attributable to phase transformations between γ- and δ-MnO_2 [89]. In contrast, the intensity of the peaks of λ-MnO_2 remained comparatively stable, indicating a slow degradation of λ-MnO_2. The intensities of the peaks were however weaker than those of γ-MnO_2 which indicated better proton diffusion of the latter. It was found that towards 0.5 V vs. Hg/HgO, bubbles were created which was likely caused by oxygen evolution reaction. Thus, the charge cut-off potential for both γ- and λ-MnO_2 in battery mode (electrochemical charge/discharge cycling) was set at 0.5 V vs. Hg/HgO.

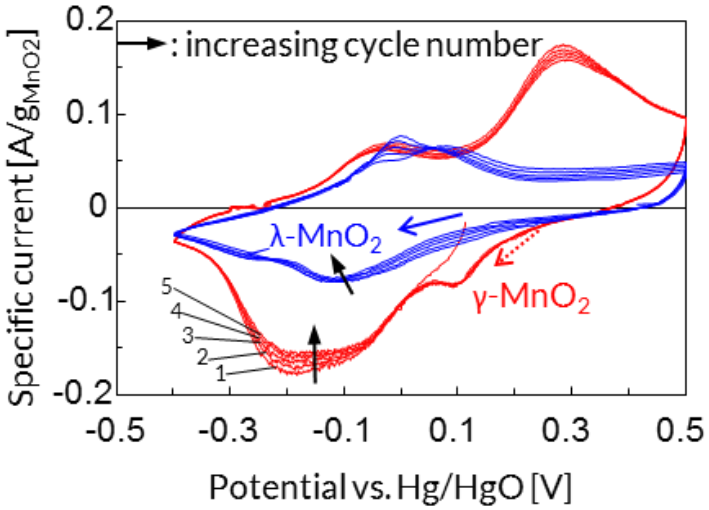

Fig. 3.5: CV curves of γ-MnO_2 and λ-MnO_2 comprising five loops between −0.4 V and +0.5 V vs. Hg/HgO. All CV cycles were conducted at 0.1 mV/s.

3.3.2. Chemical charging of MnO_2 with oxygen

After one-electron discharge reaction of the γ- and λ-MnO_2 electrodes, the electrodes were chemically charged with highly pressurized oxygen gas at 1.0 MPa. The chemical charge curves of the electrodes are shown in Fig. 3.6 (a). The potentials of both electrodes rapidly increased after the initiation of oxygen flow and after 1 h of oxygen charging, the potentials of γ- and λ-MnO_2 reached -0.033 V vs. Hg/HgO and 0.037 V vs. Hg/HgO, respectively. After chemical charging, the electrodes were electrochemically discharged in ambient conditions at

0.1 C. The electrochemical discharge curves are shown in Fig. 3.6 (b). It was observed that both electrodes were chemically charged by oxygen. The regenerated capacities of the γ-MnO_2 and λ-MnO_2 samples were determined to be 33.7 mAh/g and 37.1 mAh/g, respectively. The electrodes were subsequently chemically charged with oxygen and electrochemically discharged for a total of 10 times according to the same procedure as in the first cycle in order to verify the possibility of MnO_2 to be chemically oxygen charged. The cumulative charge capacities are shown in Fig. 3.6 (c). The cumulative charge capacity of both electrodes exceeded the theoretical capacity of 308 mAh/g which thus proofs that the electrodes were chemically charged with oxygen. It is likely that the cumulative charge would have been even higher if additional cycles had been carried out. The cumulative capacity of γ- and λ-MnO_2 after 10 cycles were 333.5 mAh/g and 399.6 mAh/g, respectively.

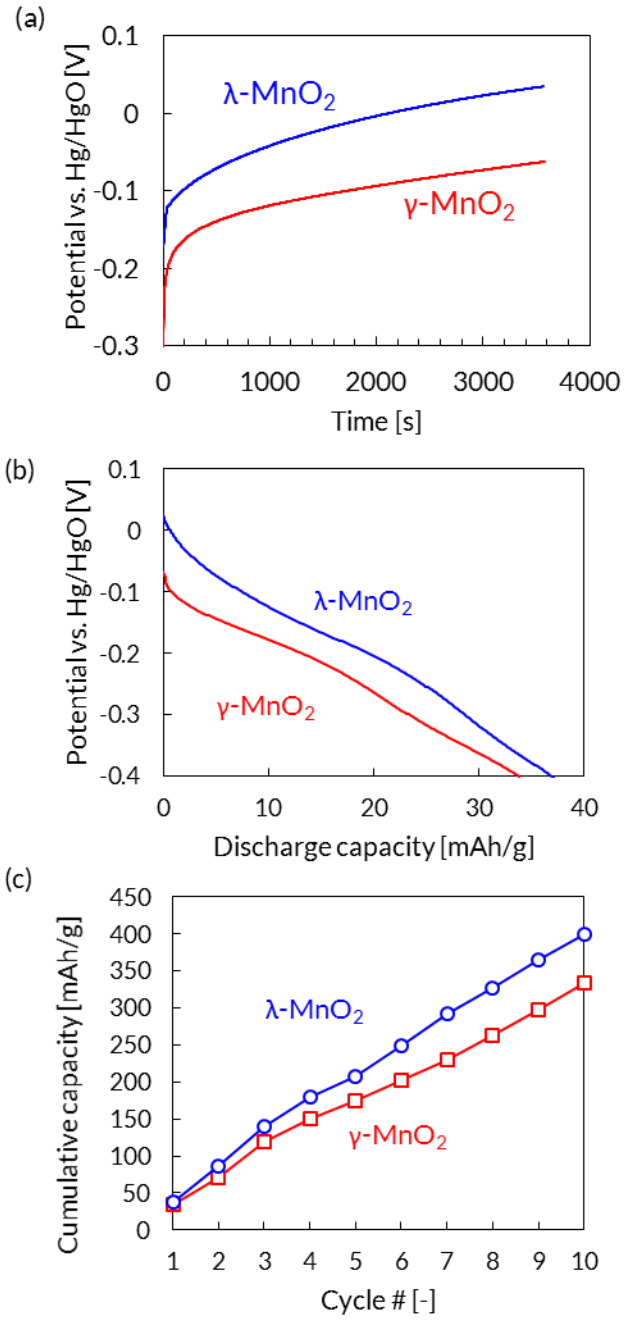

Fig. 3.6: (a) potential evolution of γ-MnO_2 and λ-MnO_2 during chemical charging at 0.1 C, (b) subsequent electrochemical discharge curves, (c) cumulative discharge capacity of 10 FCB cycles

To identify the charged capacity throughout chemical charging, the chemical charge curves were compared with the electrochemical charge curve (at 0.1 C), shown in Fig. 3.7 (a). During the electrochemical charge, every potential referred to a certain amount of charged capacity in mAh/g. The charged capacity during chemical oxygen charging could thus be approximated

by referencing the potential during chemical oxygen charging with the potential during electrochemical charge and the according charged capacity. The resulting charged capacity during oxygen charging increased as shown in Fig. 3.7 (b).

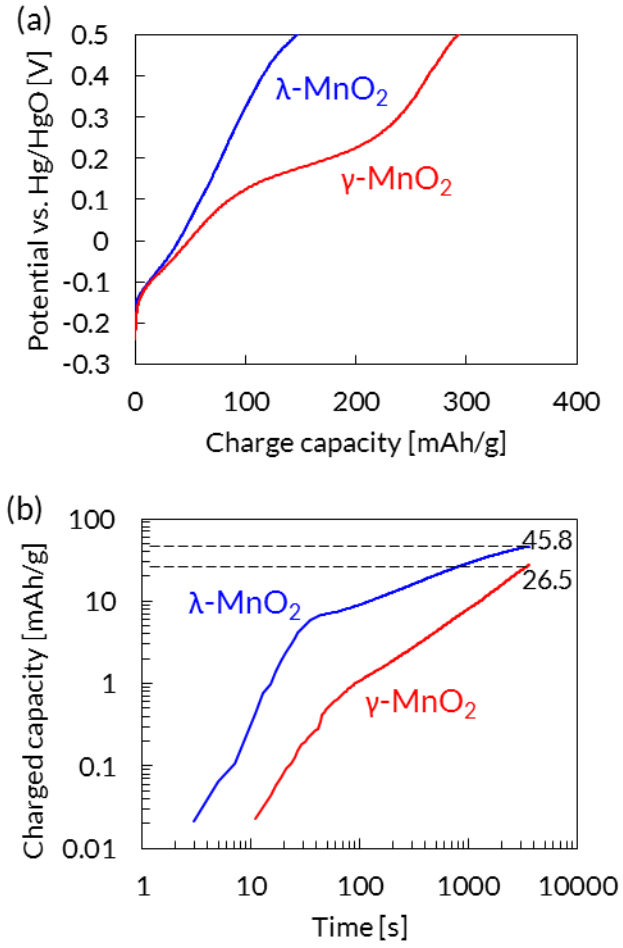

Fig. 3.7: (a) electrochemical charge curves and (b) calculated chemical charge cruves of γ- and λ-MnO_2

Clearly, this is only an approximation, as during electrochemical charge a charge transfer resistance leads to an increased voltage. However, it was found that implementing a charge transfer resistance mostly affected the calculated chemical charge capacity during the first tens of seconds, i.e. the time frame which was not analyzed in depth in this work. The calculated capacities after 1 h of oxygen charging were 26.5 and 45.8 mAh/g for γ-MnO_2 and λ-MnO_2, respectively. These values are within a reasonable range compared to the actual charged capacities measured through electrochemical discharge (31.9 mAh/g and 36.8 mAh/g,

respectively), although the charged capacity particularly in case of λ-MnO_2 seems to be overestimated with this method.

As pointed out in this chapter's introduction, the chemical charging of MnOOH starts at the surface and bulk MnOOH is charged by proton diffusion to the surface. In order to identify the different stages, the deviations of the charged capacities (Fig. 3.7 (b)) were calculated and shown in Fig. 3.8 (a) and (b). For both γ- and λ-MnO_2 electrodes three distinct regions could be detected. During the first tens of seconds big fluctuations were observed which probably occurred due to unstable oxygen concentrations in the electrolyte because of the start of oxygen gas supply. This transition time was difficult to repeat and is therefore not analyzed further in this dissertation. It was named stage 0. Thereafter, in stage 1, the charge rate was constant and it is proposed that during this time, chemical charging of the surface of MnOOH was the rate determining step. In stage 2, the charge rate slowed down which was supposedly due to proton diffusion limitations.

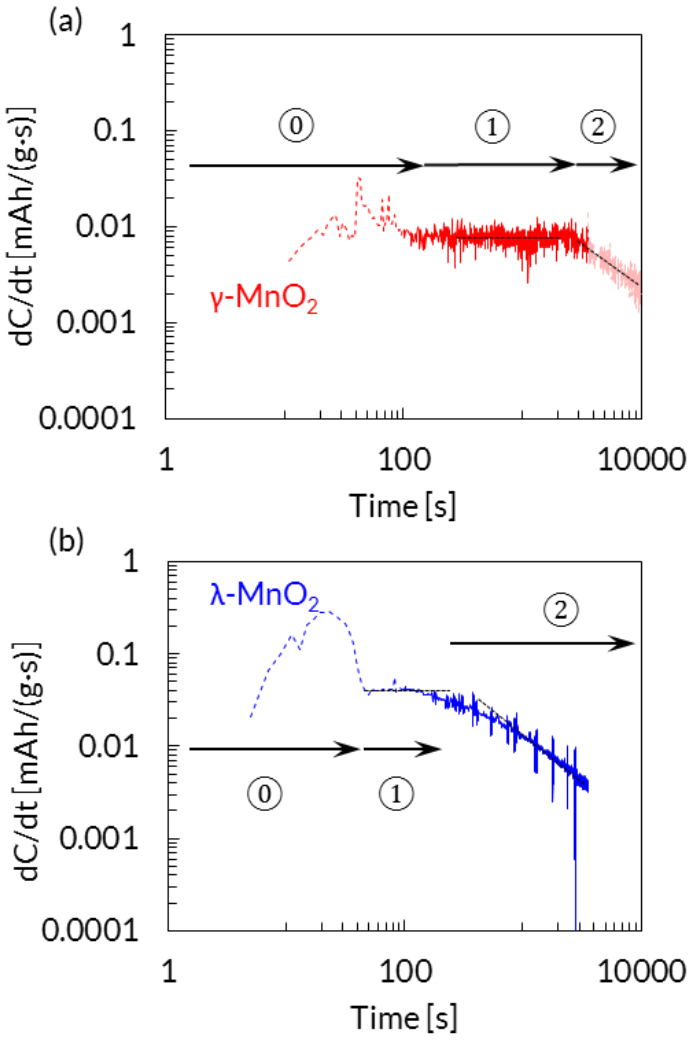

Fig. 3.8: change in charge rate of (a) γ-MnO_2 and (b) λ-MnO_2 during chemical charging with oxygen. In both electrodes, three stages were observed. In (a), data of extended charge step is shown in order to clearly highlight the three phases of γ-MnO_2

The reaction rate (r) for chemical charging of MnOOH with oxygen can be represented according to following equation:

$$r = \frac{d[Mn^{4+}]}{dt} = -\frac{d[Mn^{3+}]}{dt} = k\,[Mn^{3+}]^n[O_2]^m. \qquad (3.1)$$

Thereby [x] is the concentration of each respective element [M], t is the time [s], k is the reaction constant, and n and m are the partial reaction orders ≥ 0.

It can be considered that during chemical oxygen charging, oxygen diffusion, oxygen adsorption, surface oxidation and proton diffusion were possible rate limiting steps. After the transition time, it is unlikely that oxygen diffusion and adsorption were the rate limiting step as these reactions were found to be rapid by others [90]. Thus, it is likely that surface oxidation or proton diffusion were the rate limiting steps.

As can be seen in Fig. 3.8 (a) and (b), the reaction rates were constant in stage 1, which implies that during that stage, the concentration of surface MnOOH and adsorbed oxygen was constant. Thus, the proton and oxygen diffusion were quick enough to keep the concentration of MnOOH and oxygen at the surface sufficiently high to sustain a constant reaction rate r. Hence, the rate limiting step in stage 1 during chemical charging with oxygen was likely chemical charging of the surface. Surface charging in turn can be split into two reactions, i.e. (i) charge transfer and (ii) proton removal.

During charge transfer, electrons pass from MnOOH onto the adsorbed oxygen. The oxidation state of Mn ions thus increase from the tertiary to quaternary state as follows:

$$Mn^{III}OOH + \frac{1}{2}O_{2,ads} \rightarrow Mn^{IV}OOH + \frac{1}{2}O_{2,ads}^{2-}. \qquad (3.2)$$

After charge transfer, protons have to be removed from the MnOOH lattice. In previous work [23], it was suggested that after oxygen adsorption, oxygen dissociates and reacts with protons to form MnO_2 and H_2O. However, due to structural incompatibility, the oxygen molecules are unlikely to be directly degraded to water as this would require a simultaneous dissociation and uptake of four protons and four electrons per oxygen molecule. Instead, an intermediate degradation into hydrogen peroxide (H_2O_2) is likely, which was suggested previously by Llompart *et al.* [88]. The reaction was proposed to be as follows:

$$2MnOOH + O_2 \rightarrow 2MnO_2 + H_2O_2. \quad (3.3)$$

H_2O_2 subsequently degenerates, which is well known to proceed rapidly on MnO_2 [91]

$$H_2O_2 \rightarrow H_2O + \frac{1}{2}O_2. \quad (3.4)$$

A detailed degradation mechanism of hydrogen peroxide on MnO_2 can be found elsewhere [91]. It is thus likely that after charge transfer, only hydrogen is transferred from the crystal to the adsorbed oxygen and a not hydroxide ion, as is the case in ORR (shown in eq. 1.23).

$$Mn^{IV}OOH + \frac{1}{2}O_{2,ads}^{2-} \rightarrow Mn^{IV}O_2 + \frac{1}{2}H_2O_2. \quad (3.5)$$

Due to the formation of hydrogen peroxide, the rate at which it is degenerated shall be calculated here in order to assess whether it has a considerable effect on the chemical charge rate of MnOOH with oxygen. It was shown previously by Kanungo *et al.* [91] that the conversion rate of H_2O_2 into O_2 in pH 14 was approximately 0.4 $ml_{O2}/(g_{MnO2}\cdot s)$ of the least active MnO_2 compound. Under the assumption of O_2 being an ideal gas (1 mol = 22.4 L), the conversion rate equaled 17.9 $\mu mol_{O2}/(g_{MnO2}\cdot s)$. 4 moles of MnOOH can be oxidized with a mole of oxygen and the molar mass of MnO_2 is 86.9 g/mol. Thus, the calculated total time (τ) to decompose all H_2O_2 created during oxygen charging is:

$$\tau = \left(86.9\frac{g_{MnO_2}}{mol_{MnO_2}} \cdot 4\frac{mol_{MnO_2}}{mol_{O_2}} \cdot 17.9\frac{\mu mol_{O_2}}{g_{MnO_2}\cdot s}\right)^{-1} = 161s. \quad (3.6)$$

The peroxide degradation is therefore unlikely to considerably affect the overall oxygen charge kinetics and is thus excluded from deeper analysis in this dissertation.

As can be seen in Fig. 3.8 (a) and (b), after a constant chemical charge rate with oxygen in stage 1, the reaction rate slowed down in stage 2. According to eq. (3.1), this means that the

availability of surface Mn^{3+} and/or adsorbed oxygen decreased. To identify whether a lack of Mn^{3+} or lack of oxygen caused the slow-down, additional considerations have to be made. During chemical charging with oxygen, a water film was formed on the MnO_2 surface. Oxygen thus had to diffuse through this layer to continue the chemical charging process. Similarly, protons had to diffuse from the bulk to the surface of the particles. In both cases, the diffusion was thus crucial. In case of oxygen diffusion in water, the diffusion coefficient is ca. $2.10 \cdot 10^{-9}$ $m^2\ s^{-1}$ [92], which is comparatively quick. In case of solid state diffusion of protons in γ-MnO_2, the diffusion coefficient is several order of magnitude higher, i.e. between 10^{-12} and 10^{-24} $m^2\ s^{-1}$ [93]. Thus, in stage 2, the reason for the slow-down of the chemical charge rate can be ascribed to the proton diffusion from bulk to the surface.

Considering the observations made in this chapter, it is suggested that the chemical oxygen charge mechanism of discharged MnOOH proceeds according to following reactions. (For the forthcoming equations, the indices s and b stand for surface and bulk, respectively.) First, oxygen is rapidly dissolved into the electrolyte and adsorbed on the surface of MnOOH:

$$O_{2,gas} \rightarrow O_{2,diss} \rightarrow O_{2,ads}. \qquad (3.7)$$

Thereafter, adsorbed oxygen oxidizes surface Mn^{3+} to Mn^{4+}, whereby oxygen transforms into negatively charged peroxide.

$$2Mn^{III}OOH_s + O_{2,ads} \rightarrow 2Mn^{IV}OOH_s \cdot (O_2^{2-})_{ads}. \qquad (3.8)$$

Next, protons at the surface are transferred to the adsorbed negatively charged peroxide. This transforms MnOOH into MnO_2 and protonates the charged peroxide:

$$2Mn^{IV}OOH_s \cdot (O_2^{2-})_{ads} \rightarrow 2Mn^{IV}O_{2,s} + H_2O_{2,ads}. \qquad (3.9)$$

It shall be noted that the proton transfer may not necessarily be complete and instead intermediary HO_2^- can also be created. In either case, due to the high catalytic activity of MnO_2, peroxide (or its ion) will be quickly degraded. The following reaction can thus be assumed to be fast:

$$H_2O_{2,ads} \rightarrow H_2O + \frac{1}{2}O_{2,ads}. \qquad (3.10)$$

Finally, bulk MnOOH is oxidized by proton diffusion from bulk to the surface according to following reaction:

$$Mn^{III}OOH_b + Mn^{IV}O_{2,s} \rightarrow Mn^{IV}O_{2,b} + Mn^{III}OOH_s. \qquad (3.11)$$

These reaction are graphically summarized in Fig. 3.9.

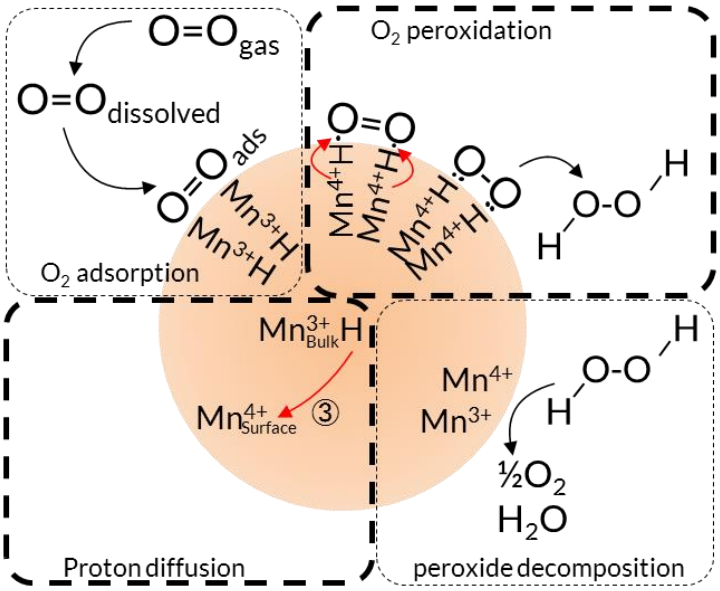

Fig. 3.9: Detailed overview of the chemical charging mechanism of MnOOH with oxygen.

3.4. Conclusions

In this chapter the chemical oxygen charging of discharged MnO_2 (i.e. MnOOH) was analyzed. In order to get a better understanding of the underlying mechanism, the potential during chemical charging was referenced with the potential during electrochemical charging,

based on which the chemical charge rate was deducted. Three distinct stages could be identified which were assigned to oxygen adsorption, surface oxidation and proton diffusion. It was found that after the transition time, surface oxidation was the initial rate limiting step followed by proton diffusion.

Limited comparisons between γ- and λ-MnO_2 have been made in this chapter. Although both materials showed the same three distinct phases, considerable differences among each charge rates were observed. In the next chapter, those differences are analyzed in depth and reasons for the different findings are discussed.

Chapter 4 Surface Reaction and Proton Diffusion During Chemical Charging

Abstract

Two different crystal structures, i.e. γ-MnO_2 and λ-MnO_2 were used to identify how various physical properties, such as surface area, tunnel structure, and O–H bond strength, affect the chemical oxygen charge rate. It was found that the crystal morphology of the MnO_2 plays a crucial role during chemical oxygen charging. Limitation of crystal distortion during proton intercalation and weak O–H bonds are crucial to achieve fast surface oxidation. Large surface area was found to be particularly crucial for proton diffusion. It was found that λ-MnO_2 is a promising material as positive electrode in fuel cell/battery systems because it showed limited crystal distortion after electrochemical discharge and had weak O–H bonds. The here used γ-MnO_2 had a high surface area which was ascribed as the main reason for its fast proton diffusion. To confirm these findings, both electrodes were tested under fuel cell mode and battery mode. It was claimed that the former helped understand the processes occurring at the surface and the latter helped comprehend the solid state diffusion. For all modes, X-ray diffraction analysis was conducted to assess the crystal stability of both species. γ-MnO_2 was found to exhibit strong crystal distortions, whereas λ-MnO_2 mainly suffered from amorphization.

4.1. Introduction

In this chapter, the chemical oxygen charge mechanism was analyzed further in depth. In particular, the differences between γ- and λ-MnO_2 were studied in order to identify what effect physical properties have on the chemical oxygen charge rate. The two samples had a different crystal structure (1D tunnel structure in γ-MnO_2 and 3D tunnel structure in λ-MnO_2), different O–H bond lengths and different surface areas. In the first part, both samples were compared under FCB mode, for which the chemical charge rate curve, introduced in Chapter 3, was used for further analysis. Next, the I-V curves of both samples were measured to better understand the surface reactivity of both electrodes and electrochemical redox cycling was conducted to draw conclusions about the proton diffusion. For every part, XRD analysis was conducted to analyze the stability of both electrodes under different conditions. This also allowed for verification whether λ-MnO_2 could be used as an alternative to γ-MnO_2 in a fuel cell/battery system.

The same experimental apparats were used as in previous chapters. In addition, Electrochemical impedance spectroscopy (EIS) measurements were carried out using a frequency response analyzer (1255B, Solartron). The frequency response was measured between 0.01 Hz and 100 kHz with an AC amplitude of 10 mV and a scan rate of 10 points per decade.

4.2. Results and discussion

4.2.1. Fuel cell/battery mode

As explained in the previous chapter, the charging of MnOOH first occurs at the surface, which in itself is split into charge transfer and proton removal, followed by bulk charging. The discussion of this chapter follows therefore the outline shown in Fig. 4.1, together with verification under fuel cell mode and battery mode.

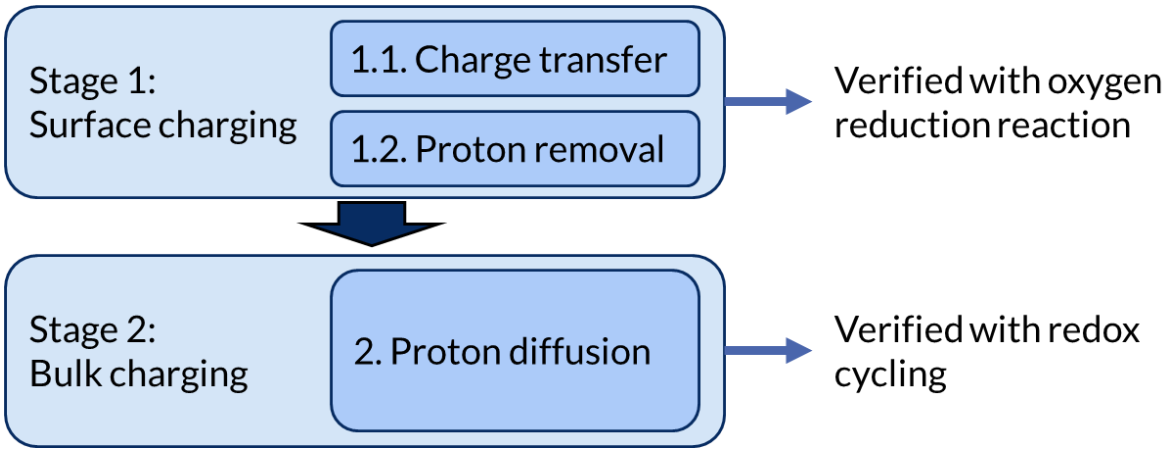

Fig. 4.1: Discussion outline of this chapter

The surface charge rate can be quantified with the chemical charge curve shown in Fig. 4.2. In case of γ-MnO_2, the calculated chemical charge rate with oxygen was 8.0 μAh g^{-1} s^{-1} throughout most of the chemical charge step, which was very close to the value of 8.3 μAh g^{-1} s^{-1} identified previously with a similar set-up and conditions [23]. This supports the methodology introduced in Chapter 3 to measure the charge rate during chemical charging with oxygen. In case of λ-MnO_2, the chemical charge rate after the transition was 40 μAh g^{-1} s^{-1}, which is 5 times faster than that of γ-MnO_2.

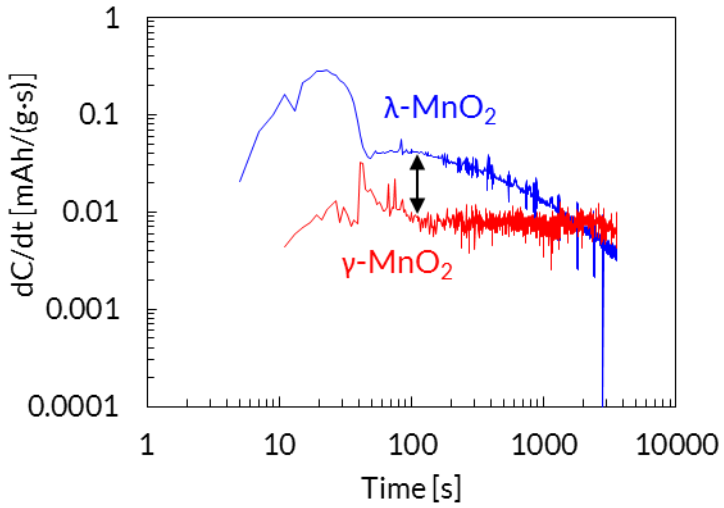

Fig. 4.2: Chemical charge rate of γ- and λ-MnO_2 with oxygen at 1.0 MPa.

This is a surprising result considering the surface area, which was 51.5 m^2/g and 14.5 m^2/g for γ-MnO_2 and λ-MnO_2, respectively. The surface specific oxygen charge rate of λ-MnO_2 was thus 17.5 times higher than that of γ-MnO_2. Clearly, the surface area might have changed after discharge, but it is unlikely that the change in surface area itself accounted for the large difference in surface specific chemical charge rate between γ-MnO_2 and λ-MnO_2.

Fig. 4.2 furthermore shows that λ-MnO_2 moved from stage 1, surface charging, to stage 2, bulk charging, much earlier than γ-MnO_2. It can be considered that due to a faster surface charging, λ-MnO_2 inevitably had to move earlier to stage 2. But in addition to that, the point at which the chemical charging moved from stage 1 to stage 2 was also affected by the proton diffusion. The faster the diffusion, the longer surface charging remained the rate limiting step. Because proton diffusion became the rate limiting step in λ-MnO_2 very early, it is possible that the proton diffusion was slower than in γ-MnO_2.

Surface charging – charge transfer

EIS measurements were conducted in order to verify the differences between γ-MnO_2 and λ-MnO_2. The equivalent circuit model used for the calculations herein consisted of an uncompensated solution resistance (R_{sol}), a charge transfer resistance (R_{ct}), a constant phase element (CPE), and a Warburg element. R_{sol} and R_{ct} are the solution resistance from the reference electrode to the MnO_2 electrode current collector and the resistance to charge transfer at the electrode-electrolyte interface, respectively. As shown in Fig. 4.3 (a), the semi-circle of discharged λ-MnO_2 was much smaller (R_{ct} = 8 Ω) than that of discharged γ-MnO_2 (R_{ct} = 22 Ω), which indicated that the charge transfer resistance of λ-MnO_2 was approximately 2.75 times lower than that of γ-MnO_2. To support this claim, the activation energy of the charge transfer was measured.

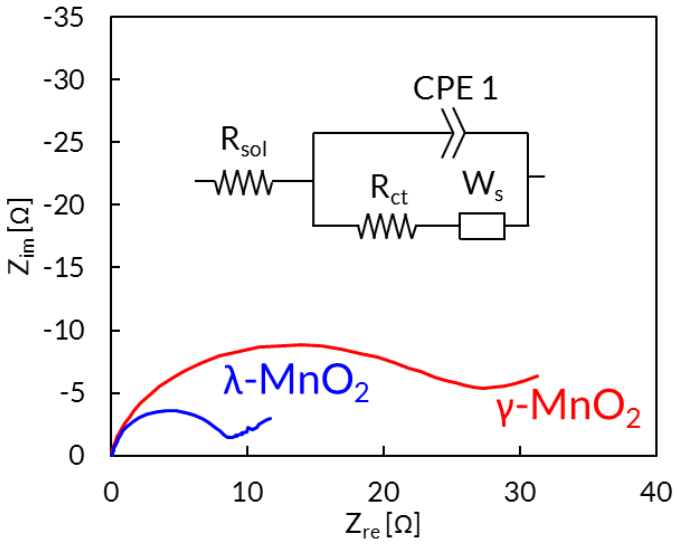

Fig. 4.3: (a) electrochemical impedance spectroscopy curves of protonated ($MnOOH_{0.8}$) γ-MnO_2 and λ-MnO_2 with equivalent circuit model and

The activation energy was measured by the Arrhenius method. According to the Arrhenius function, the reaction rate and activation energy are related according to following formula:

$$k_{ct} = k_0 \exp\left(-\frac{E_a}{RT}\right). \quad (4.1)$$

Thereby is k_{ct} the charge-transfer reaction rate, k_0 is a pre-factor, E_a is the activation energy [kJ K^{-1} mol^{-1}], R is the universal gas constant [8.314 kJ/mol] and T is the absolute temperature [K]. The charge-transfer reaction, in turn, could be calculated according to following equation [94]:

$$k_{ct} = \frac{RTV_m}{n^2F^2AR_{ct}C_{H+}^{\frac{1}{2}}}\left(x(1-x)\right)^{-\frac{1}{2}}. \quad (4.2)$$

Thereby is V_m the mole volume of MnO_2 [mol cm^{-3}], n is the number of exchanged electrons [-], F is the Faraday constant [96485 s A mol^{-1}], A is the surface area [cm^2], c_{H+} is the proton concentration [cm^{-3}], and x is the mole fraction of MnO_2 [-]. Thus, the reaction rate k_{ct} is linearly proportional to the temperature T and inversely proportional to the charge transfer resistance R_{ct} (all other parameters are considered constant):

$$k \propto T/R_{ct} \quad (4.3)$$

On a typical Arrhenius plot, the logarithm of the reaction rate k is plotted on the ordinate and 1/T on the abscissa and the activation energy is calculated by measuring the slope. To simplify the analysis, instead of calculating k_{ct}, $\ln(T/R_{ct})$ was plotted on the ordinate to identify the activation energy. R_{ct} was measured at different temperatures, namely at 10°C, 20°C, 30°C, 40°C, and 50°C according to the equivalent circuit model as in Fig. 4.3. The resulting Arrhenius plot is shown in Fig. 4.4.

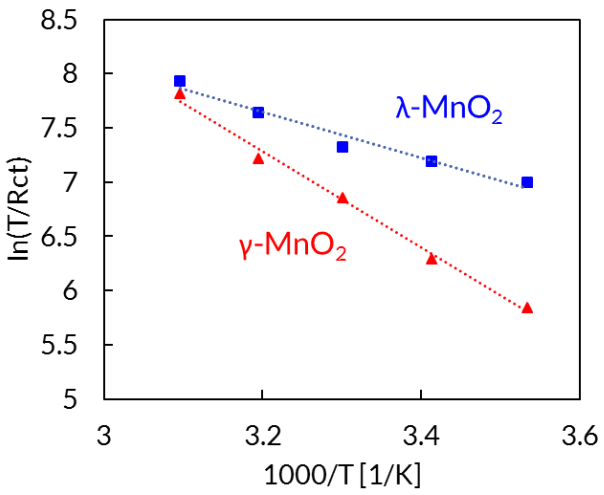

Fig. 4.4: Arrhenius plot of discharged γ- and λ-MnO_2.

The slopes were calculated according to the least squares method. The values and the derived activation energies are summarized in Table 4.1. These values confirm that charge transfer reaction occurred more rapidly in discharged λ-MnO_2 than in discharged γ-MnO_2.

Table 4.1: Slope and activation energies of γ- and λ-MnO_2

	Slope -Ea/R [K]	Activation energy [kJ/mol]
γ-MnO_2	4424	36.8
λ-MnO_2	1806	17.5

Crystal Field Theory

Although the chemical charge curves, EIS measurements, and activation energy analysis all suggested that the surface of discharged λ-MnO_2 is charged more rapidly with oxygen, it is unclear why this was the case. To identify a possible reason for these findings, theories of quantum chemistry were used.

It was found that besides the crystal structure, also the state-of-charge (SOC) had a large influence on the charge transfer resistance. The charge transfer resistance was measured at different SOC, showing that both γ- and λ-MnO_2 have a low charge transfer resistance at high SOC and a high charge transfer resistance at low SOC. In case of γ-MnO_2, the charge transfer resistance started to surge at an SOC of 60%, where its R_{ct} was 0.6 Ω, to 22.0 Ω at an SOC of 80%. In λ-MnO_2, the R_{ct} started to increase considerably from an SOC of 40% (0.3 Ω) and reached a charge transfer resistance of 7.6 Ω at an SOC of 80%. The R_{ct} vs. SOC plot is shown in Fig. 4.5.

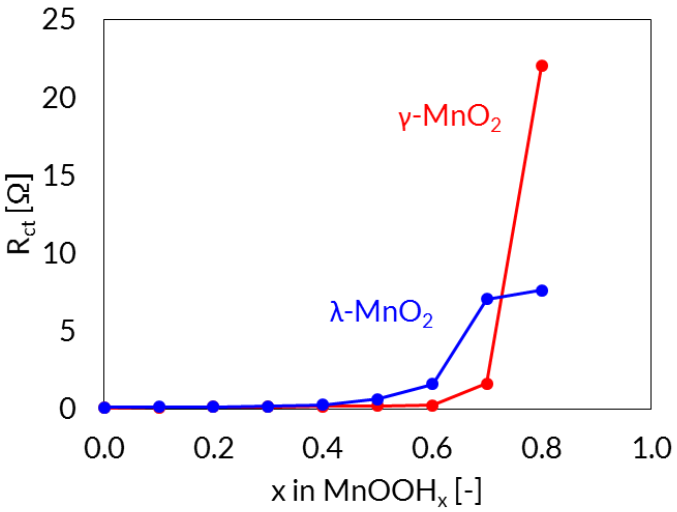

Fig. 4.5: Dependency of charge-transfer resistance on state of charge

The reason for this increased charge transfer resistance is likely Jahn-Teller distortion. The crystal field theory qualitatively describes how the bond strength of metal-ligand (here: Mn–O) bonds affects the energy of the system [95]. Due to the static electric field produced by the surrounding oxygen, the degeneracies of the d orbital of Mn are broken. This results in a field splitting in a MnO_6 octahedal according to Fig. 4.6. Six covalent p bonds between Mn and O are present and the three valence electrons from Mn occupy the d_{xy}, d_{xz}, d_{yz}, orbital. This leaves the $d_{x^2-y^2}$ and d_{z^2} unoccupied and at a higher energy level because these orbitals are further

away from the ligands and therefore experience less repulsion. The three lower-energy orbitals and two higher-energy orbitals are usually denoted as t_{2g} and e_g, respectively. The difference between t_{2g} and e_g is equal to the crystal-field splitting energy Δ_{Oct}.

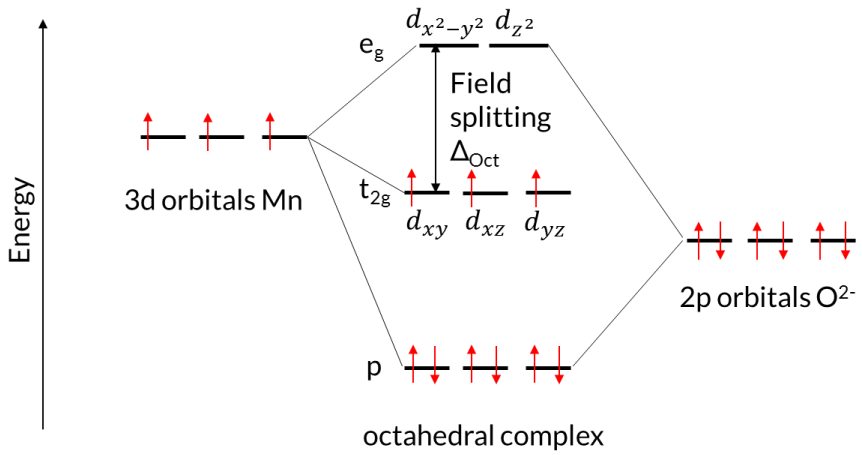

Fig. 4.6: Energy level of MnO_6 octahedron

Due to a comparatively small Δ_{Oct}, MnO_2 is considered a high-spin compound, wherefore upon increasing the oxidation state from tetravalent to trivalent state, the electron jumps into the e_g level, namely the d_{z^2} orbital. This creates a spatially degenerate electronic ground state which, according to the Jahn-Teller theorem [96], leads to a geometrical distortion to remove that degeneracy. In case of MnO_6 octahedra, this leads to an elongation of the octahedral.

This elongation of the bonds can be measured with x-ray absorption and has been done previously by others [71,72,97,98]. The bond lengths are summarized in Table 4.2. γ-MnO_2 – which is typically analyzed by measuring the bond lengths separately of birnessite (1×1 tunnels) and ramsdellite (2×1 tunnels) – shows a more intense elongation of the octahedral structure than λ-MnO_2.

Table 4.2: Mn-O bond lengths of charged and discharged γ- and λ-MnO_2

	γ-MnO_2 [Å]		λ-MnO_2 [Å]
	Birnessite	Ramsdellite	
MnO_2	1.88 – 1.90	1.82 – 1.97	1.92
MnOOH	1.88 – 2.34	1.90 – 2.34	1.93 – 2.16

This geometrical change of the octahedral obviously affects the crystal lattices, wherefore a change of the MnO_6 octahedral can also be observed with XRD analysis. Therefore, the XRD patterns of γ- and λ-MnO_2 were studied before and after electrochemical discharge. The patterns are shown in Fig. 4.7.

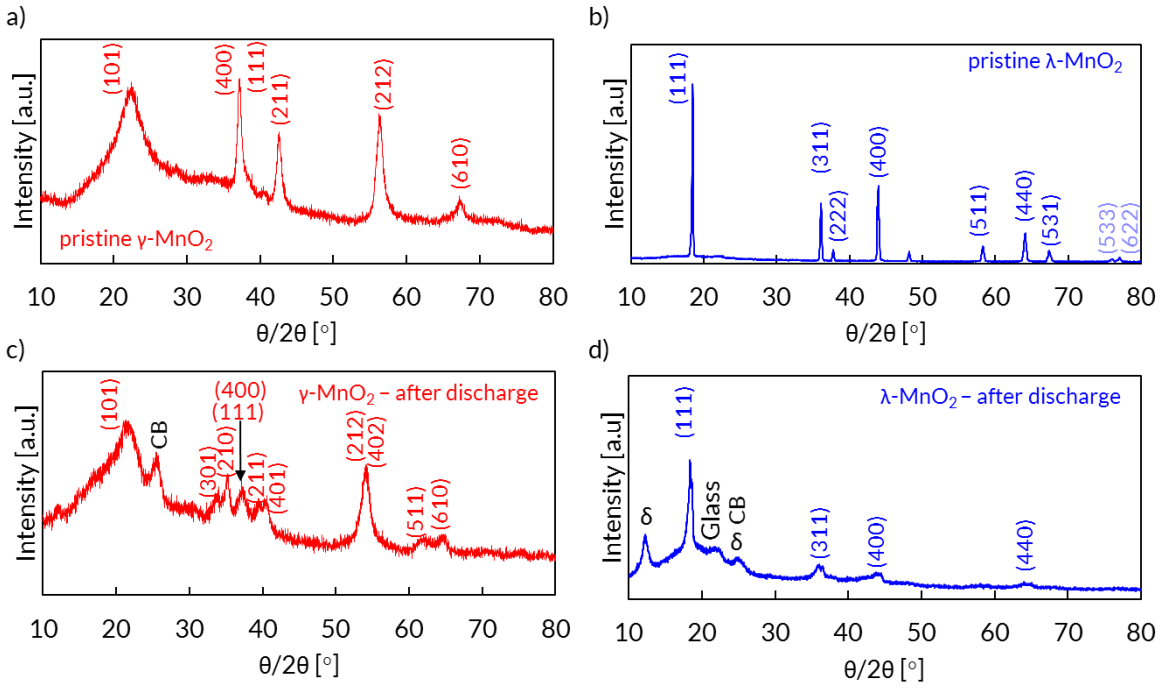

Fig. 4.7: X-Ray diffraction patterns of pristine and electrochemically discharged γ- and λ-MnO_2.

The crystal lattice parameters were calculated according to Bragg's law [99] (see Appendix B for additional details), and summarized in Table 4.3. The results confirm that the structural parameters change considerably more in case of γ-MnO_2 than λ-MnO_2 upon complete discharge.

Table 4.3: Crystal lattice parameters of charged and discharged γ- and λ-MnO_2

	γ-MnO_2		λ-MnO_2	
axis	MnO_2	MnOOH	MnO_2	MnOOH
a	8.93	10.84	8.23	8.23
b	2.89	3.16	8.20	8.23
c	4.43	4.34	8.54	8.65

This geometrical distortion directly affected the energy levels and thus the charge transfer resistance. As shown in Fig. 4.8, in case of MnOOH, the valence band is the d_{z^2} orbital and the conduction band is the $d_{x^2-y^2}$ orbital. The energy level of the conduction and valance band dictate the speed of a reaction because it is energetically favorable to add electrons to a low-lying conduction band or to extract electrons from a high-lying valence band [100]. Thus, the smaller the gap, i.e. the smaller the geometrical distortion, the higher the chemical reactivity.

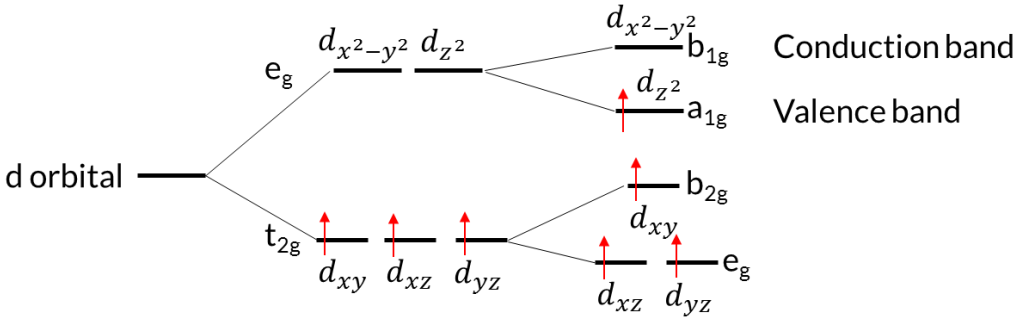

Fig. 4.8: Band gap in MnOOH

The charge-transfer resistance is therefore directly dependent on the geometry of the MnO_6 octahedra and their allocation. The larger the distortion, the larger the band gap and thus the larger the charge transfer resistance. The main reason for a large charge-transfer resistance in MnOOH is likely due to the Jahn-Teller distortion. But in addition, as was summarized in Table 4.2, γ- and λ-MnO_2 also have different Mn-O bond lengths in charged state, i.e. where Jahn-Teller does not occur. These distortions likely affect the charge-transfer resistance as well,

wherefore not only Jahn-Teller distortion, but any kind of crystal distortion is suggested to affect the charge-transfer resistance.

The band-gap can be measured via scanning tunneling spectroscopy. This technique allows to measure the density of electrons as a function of their energy. This density of states (DOS) pattern λ-MnO_2 is shown in Fig. 4.9 and shows that the band gap of bulk λ-MnO_2 is 1.7 eV [101]. To the knowledge of the author, no such measurement was conducted on γ-MnO_2, wherefore Ramsdellite MnO_2 (2×1 tunnel structure) shall be used as reference. In that material, the band gap energy is 2.2 eV [102], i.e. 0.5 eV higher than that of λ-MnO_2. This confirms that the bandgap in λ-MnO_2 is indeed smaller which allows for a faster removal of the electron in MnOOH.

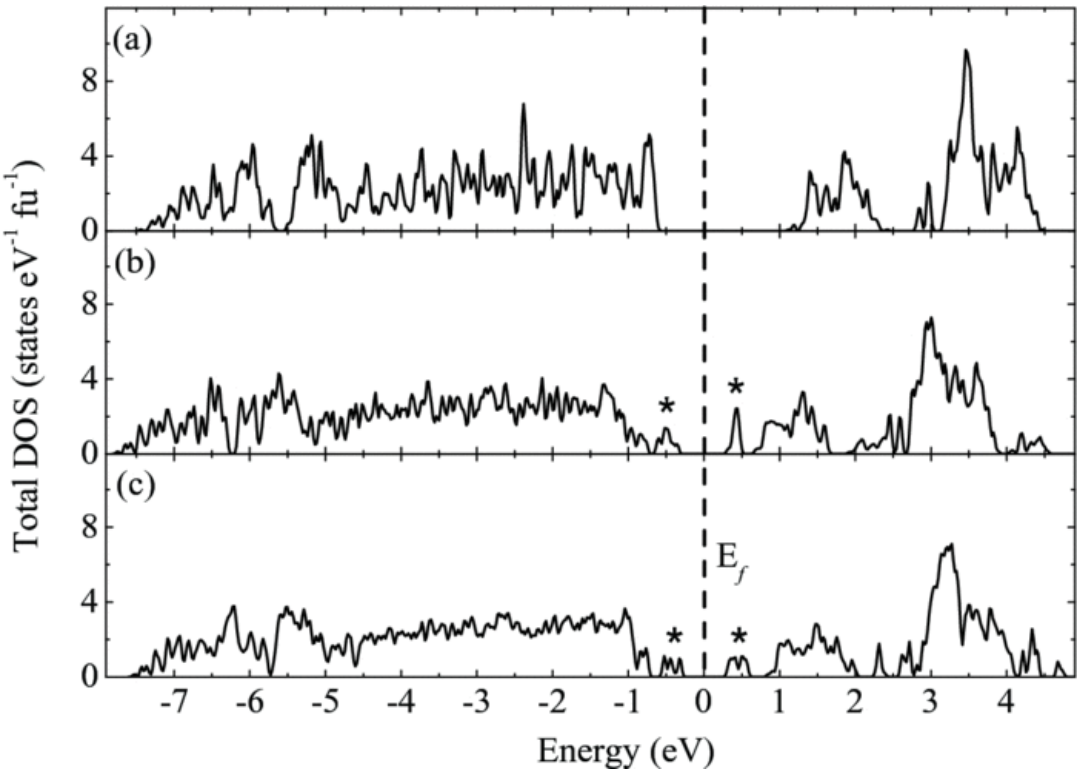

Fig. 4.9: Total DOS of (a) bulk λ-MnO2, (b) relaxed ideal λ-MnO2(001), and (c) relaxed reconstructed λ-MnO2(001). The Fermi level is set to 0 eV [101]

Surface charging – proton removal

As discussed in the previous chapter, during oxygen charging at the surface, after charge was transferred to the adsorbed oxygen, protons were removed from the crystal lattice. The rate at which protons could be removed is likely dependent on the O–H bond strength in MnOOH. A bond strength is inversely proportional to its length which can be measured with X-ray absorption spectroscopy. Kohler *et al.* [97] found that the O–H bond lengths of discharged γ-MnO_2 are 0.81 and 0.98 Å (two different values because of ramsdellite and pyrolusite structure in γ-MnO_2, both of which possess two different O–H bond lengths) and Ammundsen *et al.* [103] found that the O–H bond lengths of discharged λ-MnO_2 are 1.10 Å. The O–H bond is thus considerably longer in λ-MnO_2 than γ-MnO_2, resulting in easily removable protons during oxygen charge which allowed for faster surface charging of λ-MnO_2 during chemical charging with oxygen.

Bulk charging - diffusion

After chemical charging of the surface, in stage 2, proton diffusion became the rate limiting step. To quantify the activation energy of proton diffusion in γ- and λ-MnO_2, following formula was used [104]:

$$D = \left(\frac{RT}{\sigma A F^2 \sqrt{2} c_{H^+}}\right)^2. \qquad (4.4)$$

Thereby σ is the Warburg pre-factor [Ω] which was identified via EIS. The diffusion is therefore proportional according to following equation:

$$D \propto \left(\frac{T}{\sigma}\right)^2. \qquad (4.5)$$

Hence, for the Arrhenius plot, $\ln(T^2/\sigma^2)$ was used as the ordinate and linear regression was done according to the least squares method. The activation energies for γ- and λ-MnO_2 were

quantified as 5.35 kJ/mol and 12.55 kJ/mol, respectively, suggesting a faster diffusion in γ-MnO_2.

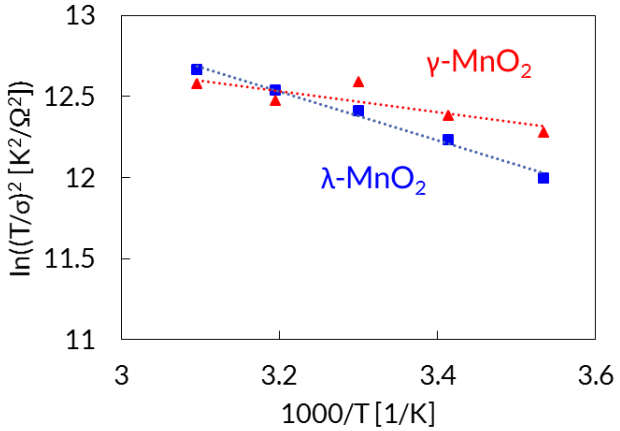

Fig. 4.10: Arrhenius plot for proton diffusion

With eq. 4.5 it was also possible to quantify the diffusion coefficient. The solid state diffusion coefficient D was calculated to be $4.96 \cdot 10^{-26}$ m^2 s^{-1} for γ-MnO_2 and $2.12 \cdot 10^{-25}$ m^2 s^{-1} for λ-MnO_2. The reason for the higher diffusivity in λ-MnO_2 may be the larger O–H bond length, which allowed for a weaker lock-in of the protons and thus allows for a higher proton mobility [105]. It should be noted though that the surface specific values are based on the BET surface area of the pristine materials. During electrochemical discharge, the surface area may change which would affect the calculated diffusion coefficient.

However, not the diffusion coefficient by itself dictated how quickly protons diffused to the surface but the solid state proton diffusion, which, according to Browning *et al.* (2005), can be correlated with A√D [93]. The basic idea behind this value is to compare the volume out of which protons diffuse, for which the surface area and diffusion length are required. The typical diffusion length L is proportional to √D [106], wherefore calculating A√D is a simple way to compare the diffusion of different materials. By considering the surface area, the calculated A√D values of γ-MnO_2 and λ-MnO_2 are $1.15 \cdot 10^{-11}$ m^3 $s^{-1/2}$ g^{-1} and $6.72 \cdot 10^{-12}$ m^3 $s^{-1/2}$ g^{-1},

respectively. The proton diffusion was thus 1.7 times faster in γ-MnO_2 compared to λ-MnO_2, which is a similar difference as the activation energy. This supports that proton diffusion, and thus bulk charging, is faster in γ-MnO_2 and highlights the importance of surface area.

These observations made during surface charging and proton diffusion can explain why the points where the chemical charging moved from stage 1 to stage 2 differed considerably among γ- and λ-MnO_2, as shown in Fig. 4.2. The charge rate of γ-MnO_2 stayed constant until 2900 s, whereas the charge rate of λ-MnO_2 slowed down after 130 s already. In γ-MnO_2, the surface oxidation was slower but proton diffusion was faster than λ-MnO_2, wherefore the chemical charge rate remained the rate limiting step during most of the charge step. This also explains why in previous research, a constant chemical oxygen charge rate was claimed for γ-MnO_2 [23]. In those measurements, the charge time was 20, 40, or 60 min, i.e. within the time frame of almost constant charge rate. If the charge time had been increased (or if λ-MnO_2 had been used), it is likely that a non-linear relationship between charged capacity and time would have been observed. In contrast to γ-MnO_2, λ-MnO_2 showed a high surface oxidation rate but slow proton diffusion, wherefore the proton diffusion was the rate limiting step during most of the chemical charging process.

4.2.2. Fuel cell mode

In order to verify the faster reaction rate at the surface of λ-MnO_2, both electrodes were tested under fuel cell mode. To evaluate the ORR, the samples were first fully discharged at 0.1 C to −0.4 V vs. Hg/HgO and then exposed to oxygen flow for 5 h to re-oxidize their surface and achieve a stable voltage. These two steps were conducted to allow for a better comparison between fuel cell mode and FCB mode, as in FCB mode, the electrodes also need to be electrochemically discharged prior to chemical oxygen charge. Thereafter, a constant current

was applied at different C-rate (from 0.01 C to 1 C) while oxygen was supplied. The resulting curves of γ- and λ-MnO_2 are shown graphically in Fig. 4.11. Because it was found that the potential did not immediately reach the final set potential but levelled off only after a few minutes, every current was applied for 1 h, which was found to be sufficient to achieve a constant potential. The reason for this slow stabilization was the intrinsic storage capacity of MnO_2. At the beginning of each step, electrochemical discharge was likely to be dominant before ORR led to a constant potential.

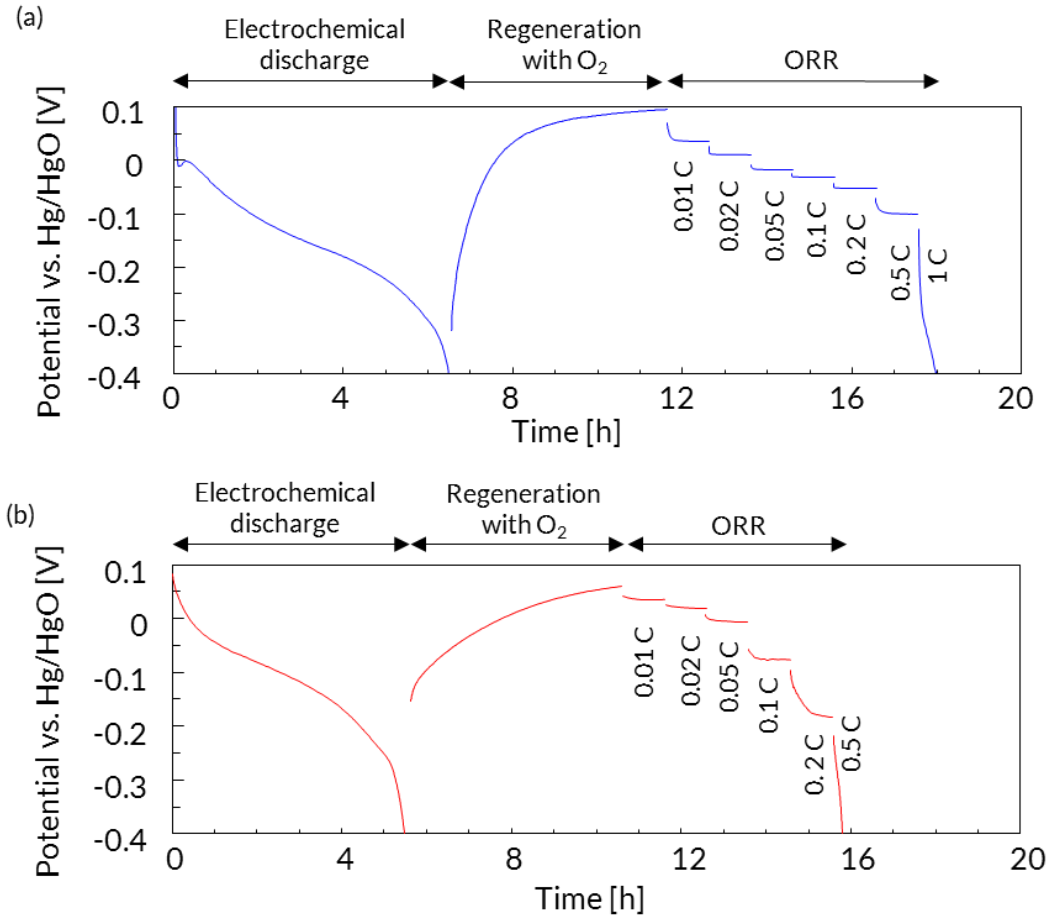

Fig. 4.11: Sequence used to measure the oxygen reduction reaction rate of MnO_2, showing typical voltage evolution during each step for (a) λ-MnO_2 and (b) γ-MnO_2.

The resulting I-V curves of the ORR experiments are shown in Fig. 4.12 where all the current rates which did not hit the cut-off voltage are shown. It was found that γ-MnO_2 could

be discharged at a current density of 7.0 mA/cm^2 (equivalent to 0.2 C) without reaching the cut-off potential. At 7.0 mA/cm^2, a potential of −0.182 V vs. Hg/HgO was measured. When the current was increased to 17.5 mA/cm^2 (0.5 C), the cut-off potential of −0.4 V vs. Hg/HgO was reached after 11 min. In contrast, λ-MnO_2 exhibited a higher oxygen reduction rate. Even at 17.5 mA/cm^2 (0.5 C), a steady potential of −0.101 V vs. Hg/HgO was observed in spite of the considerably smaller surface area of the material. At 35.0 mA/cm^2 (1 C), the cut-off potential was reached after 24 min.

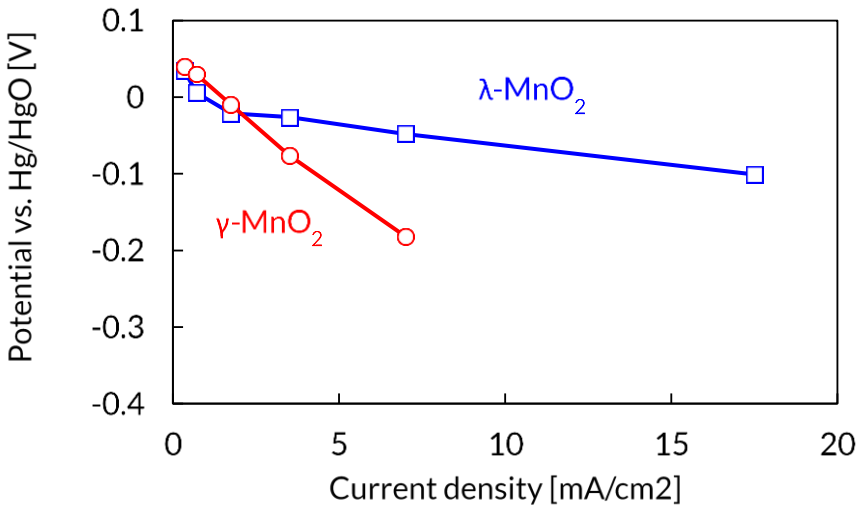

Fig. 4.12: I-V curves of γ-MnO_2 and λ-MnO_2.

Although λ-MnO_2 showed a faster ORR rate than γ-MnO_2, the difference was smaller than in stage 1 during the chemical charge rate (40 µAh/(g·min) and 8 µAh/(g·min) for λ-and γ-MnO_2, respectively). The reason for the comparatively slower ORR of λ-MnO_2 is likely due to the different mechanism of chemical charging with oxygen and ORR. In ORR, it was suggested that the adsorbed oxygen displaces the OH^- ion at the surface, wherefore the reaction rate is mostly dependent on the Mn–O bond strength [69]. In protonated γ-MnO_2 the Mn–O bond length is 2.04 Å [107] and in protonated λ-MnO_2 the Mn–O bond length is 2.01 Å [108]. The

Mn–O bond strength is thus weaker in protonated γ-MnO_2 than in λ-MnO_2 which would allow for a faster ORR in γ-MnO_2.

The reason why the ORR rate of λ-MnO_2 was still faster than that of γ-MnO_2 is likely due to its high charge transfer resistance. In a previous study by Lima *et al.* [90], it was proposed that the electron transfer from MnO_2 to the adsorbed oxygen is crucial during ORR. It is thus suggested that during ORR, the hydroxide can be removed slightly faster in γ-MnO_2 than in λ-MnO_2, but due to the much lower charge transfer resistance of the latter, the overall ORR rate is faster in λ-MnO_2.

ORR analysis is therefore to a limited extent a suitable method to analyze the surface charge rate of MnO_2 during chemical oxygen charging. During both ORR and chemical oxygen charging, charge transfer affects the reaction rate. However, during ORR, the Mn–O bond lengths are crucial whereas during chemical charging with oxygen, the O–H bond length defines the rate at which protons are removed from the lattice. Hence, even though both the chemical charging with oxygen and the ORR take place at the surface of the electroactive material, the processes are not equal. This makes ORR analysis an indicator to analyze chemical oxygen charge rate, but only to a limited extent.

After ORR analysis, the crystal structure of the samples was analyzed by XRD to evaluate the crystal durability of each material. As shown in Fig. 4.13 (a), after ORR with γ-MnO_2, the original peaks of γ-MnO_2 were still observable without any impurity peaks. The decreased intensity can be assigned to the binder that likely covered the MnO_2 particles and amorphization of the electroactive material [20]. In contrast, in the case of λ-MnO_2, formation of δ-MnO_2 was

observed, but the original peaks assignable to the λ-structure are fairly intense wherefore it is likely that amorphization occured to a lesser, but still observable, extent than in γ-MnO_2.

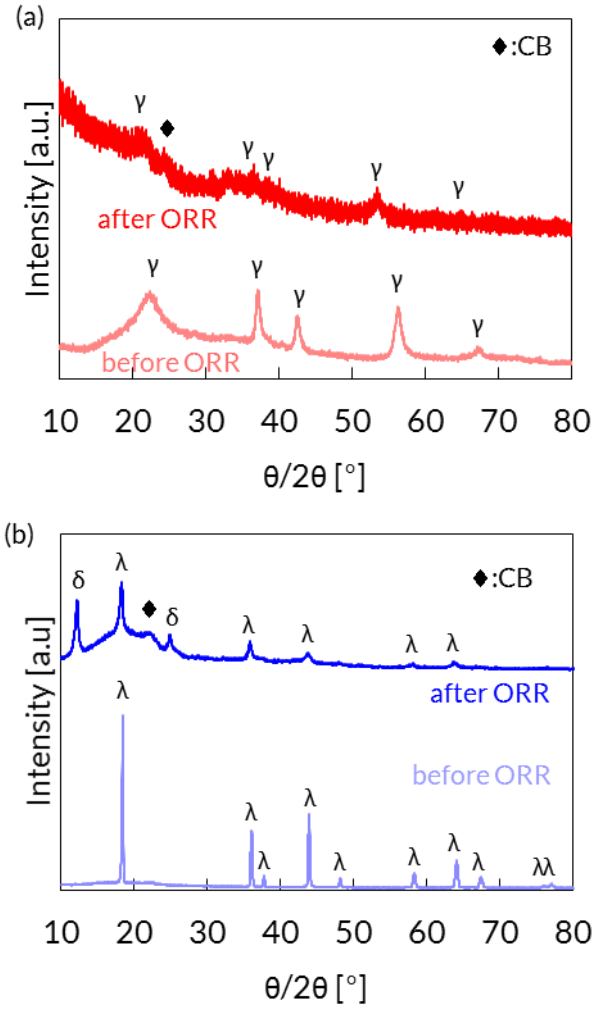

Fig. 4.13: X-ray diffraction patterns of (a) γ-MnO_2 and (b) λ-MnO_2 of used materials before and after oxygen reduction reaction measurements.

4.2.3. Battery mode

To support the different proton diffusion rate of the two samples, the electrochemical redox cycling performance of λ-MnO_2 was investigated under battery mode at charge/discharge rates of 0.1C/0.1C, 0.2C/0.2C, 0.2C/0.5C, 0.2C/1.0C, 0.2C/2.0C, and 0.2C/5.0C. The charge and discharge capacities of both γ-MnO_2 and λ-MnO_2 during 36 cycles at different charge and

discharge rates are shown in Fig. 4.14. The capacity of both electrodes decreased during the first cycles at 0.1 C/0.1 C. The subsequent cycles showed reasonably good capacity retention at the same charge/discharge rate, but the capacity decreased as the discharge rate was increased. A more significant capacity reduction was observed in the case of λ-MnO_2. During charge/discharge cycling at 0.2C/0.5C, the discharge capacity of λ-MnO_2 was only half that observed for γ-MnO_2, whereas at during subsequent 0.1C/0.1C charge/discharge cycles, the capacities of both samples were similar and recovered to 66.3% (λ-MnO_2) and 70.7% (γ-MnO_2).

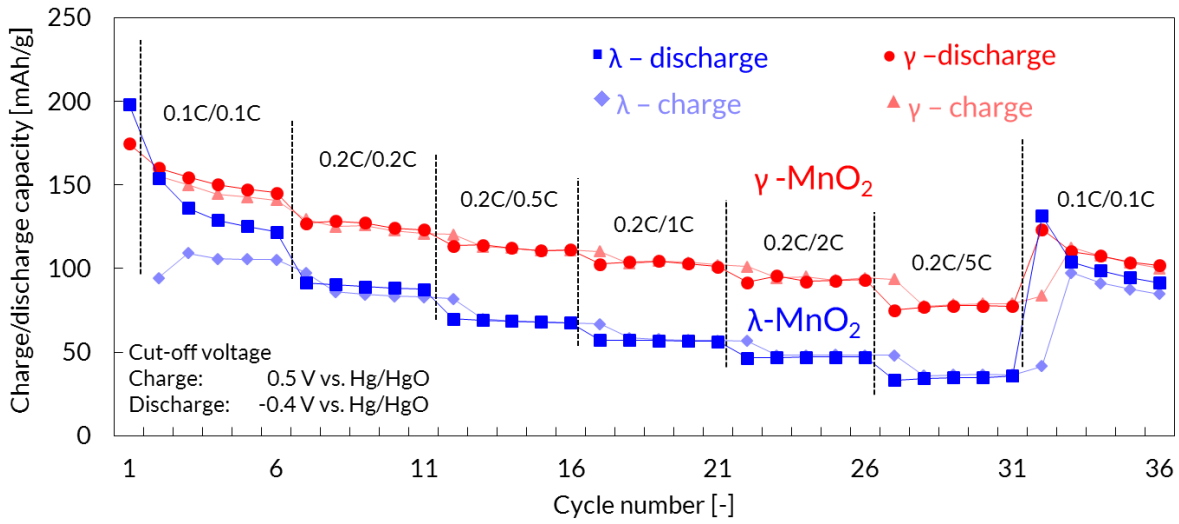

Fig. 4.14: Charge and discharge capacities of λ-MnO_2 and γ-MnO_2 at different rates.

It also has to be noted that during the first cycles, the charged capacity was lower than the discharged capacity, particularly in case of λ-MnO_2. This resulted in an apparent Coulombic efficiency of above 100%. The reason for this observation is suggested to be due to incomplete discharge during the first cycle. During the first discharge, only 198 mAh/g could be discharged, wherefore a theoretical capacity of 110 mAh/g remained in the particles. This incomplete discharge may have been due to slow proton diffusion. In the subsequent cycles, then, this remaining charge in the bulk of the particles continuously diffused towards the surface, where it allowed for a higher discharge capacity than charge capacity.

The reason for the different performance of the two materials at high discharge rate was likely their differing proton diffusivity. This observation supports the claim that proton rate of λ-MnO_2 was slower than that of γ-MnO_2. Analyzing the electrodes under battery mode thus allowed for crucial data acquisition about proton diffusion that helps asses the capability of MnO_2 during FCB mode.

In the case of both λ-MnO_2 and γ-MnO_2, the capacity decreased considerably during the first cycles. To identify the reason for the losses, XRD measurements were conducted after the first discharge and after cycling. Fig. 4.15 shows that all peaks belonging to the original γ-MnO_2 structure remained after the initial discharge and no transformation into another crystal structure occurred. Peak shifts towards higher d-values were observed, which may have been caused by Jahn–Teller distortion. During electrochemical charge/discharge cycles, however, a complete transformation into δ-MnO_2 was observed.

In contrast, λ-MnO_2 was found to transform partially into δ-MnO_2 after the first discharge. The reduction in the capacity of the λ-MnO_2 during the first few electrochemical charge/discharge cycles was thus attributable to its crystal transformation into δ-MnO_2. After 36 cycles, however, XRD patterns still revealed clear peaks belonging to λ-MnO_2 structure, suggesting a higher crystal stability of λ-MnO_2 despite its lower discharge cut-off potential compared with that of γ-MnO_2.

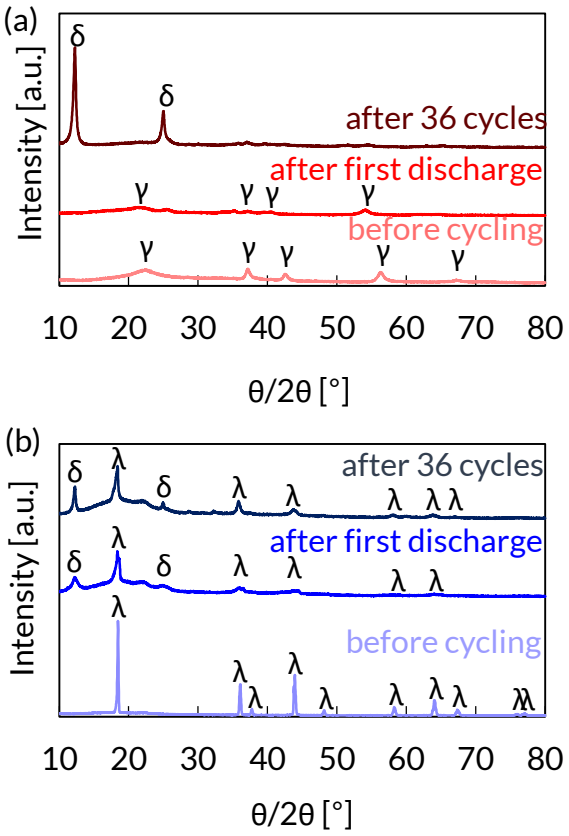

Fig. 4.15: X-ray diffraction patterns of as-used samples and samples after first discharge and after 36 cycles at different rates. (a) γ-MnO_2, (b) λ-MnO_2.

Thus, for electrochemical cycling, it can be summarized that γ-MnO_2 showed better performance at high C-rate than λ-MnO_2. This finding supports the claim that proton diffusion became more quickly the rate limiting step in λ-MnO_2 than in γ-MnO_2 during chemical charging with oxygen. The faster proton diffusion of γ-MnO_2 was due to its high surface area because proton diffusion ($A\sqrt{D}$) is directly proportional to surface area [109]. The stability of the γ-structure, however, was found to be poor, and resulted in its continuous transformation into layered δ-MnO_2. This is non-desirable because δ-MnO_2 has been shown to have poor electrochemical stability in Chapter 2. In contrast, although the λ-MnO_2 sample showed poor performance at high C-rate, its crystal structure was more stable during the electrochemical cycling. Transformation into δ-MnO_2 appeared to mainly occur during the first few cycles.

4.3. Conclusions

Two different MnO_2 crystal structures, i.e. γ-MnO_2 and λ-MnO_2, were used in this chapter in order to assess the effect of various different properties, such as surface area, crystal structure, and O–H bonding on the chemical charge rate with oxygen. Both compounds showed an approximately equivalent regenerated capacity after 1 h, but it was found that the underlying reaction rates were very different among these materials. In case of λ-MnO_2, the surface was found to oxidize rapidly, but the diffusion of protons from the bulk to the surface was observed to strongly limit the particle oxidation rate. In contrast to that, in γ-MnO_2 the surface oxidation was found to be the rate limiting step over most of the chemical charging step.

The reason for these findings were proposed to be due to the crystal morphology of MnO_2. The spinel structure of λ-MnO_2 led to high structural stability, which limited geometrical distortion and thus led to only small increase in charge transfer resistance during protonation. Furthermore, the O–H bond was found to be weaker in λ-MnO_2 which allowed for faster proton removal from the crystal lattice. The slower proton diffusion was mainly ascribed to its lower surface area. In contrast to that, γ-MnO_2 showed strong Jahn-Teller distortion during protonation leading to large charge transfer resistance. Furthermore, strong O–H bonds resulted in slow proton removal from the lattice. Due to the large surface area of γ-MnO_2, proton diffusion was comparatively fast.

In this chapter it was thus also found that λ-MnO_2 is a very promising material for application in FCB owing to its fast surface charge rate during chemical charging with oxygen, its higher crystal stability in all modes than that of γ-MnO_2 and high ORR rate despite its low surface area. Only during electrochemical cycling did γ-MnO_2 show a better performance than

λ-MnO_2, which was likely caused by its higher proton diffusion arising from its larger surface area.

Chapter 5 Performance Enhancement with Nano-Sized λ-MnO_2 and Oxygen Reduction Catalyst

Abstract

To accelerate the chemical oxygen charging rate of MnO_2, micro- and nano-sized λ-MnO_2 were synthesized and analyzed. Three different materials with different surface areas were tested according to fuel cell/battery mode, battery mode, and fuel cell mode. It was found that increasing the surface area is not only beneficial for the chemical oxygen charge rate but also positively affects the electrochemical cycling at high C-rates and oxygen reduction reaction. As such, nano-sized λ-MnO_2 could be chemically charged with oxygen to 34.1% of its theoretical capacity within 1 h at 1.0 MPa oxygen supply. In the second part, λ-MnO_2 was successfully deposited on carbon fibers to create a binder-free positive electrode. To obtain fibrous electrodes, a three-step approach was conducted. First, γ-MnO_2 was deposited onto carbon fibers electrochemically in a Mn ion containing bath. Secondly, the γ-MnO_2 was transformed hydrothermally into spinel structured $LiMn_2O_4$. Lastly, lithium ions were removed in an acidic bath to obtain λ-MnO_2. The fibers were then compared with pasted electrodes under fuel cell/battery mode to quantify the chemical oxygen charging rate. It was found that the binder free fibrous structure shows promising properties which allowed for quick chemical oxygen charge rate. Drawbacks were found in terms of mechanical stability, which led to high ohmic losses.

5.1. Introduction

In previous chapters, it was noted that λ-MnO_2 is a very promising material due to a much higher specific surface charge rate during chemical charging compared to previously used γ-MnO_2. In addition, λ-MnO_2 showed reasonable crystal and good performance under fuel cell mode. It was noted, however, that the slow proton diffusion limits even faster chemical charge rates and that a possible way to overcome this limitation is by using λ-MnO_2 with decreased particle size. In this chapter, novel λ-MnO_2 materials were synthesized with different methods to obtain particles with a smaller diameter which was expected to improve the chemical oxygen charge rate. Furthermore, the effect of the surface area on the ORR rate (fuel cell mode) and electrochemical redox cycling at different rates (battery mode) was analyzed.

In the second part of this chapter, the chemical charge rate ought to be further improved by employing a fiber structured electrode. Fibrous electrodes for FCB systems were synthesized previously by Choi *et al.* [21] and showed promising results due to (i) a better contact between electroactive material and current collector, (ii) high charge transfer rate and (iii) low overpotential [21]. In addition to that, carbon fibers do not need binder which may be advantageous for the chemical charge rate. It is likely that in pasted electrodes, the binder covered parts of the MnO_2 surface which thus inactivated some of its surface during chemical charging with oxygen. Thus, fibrous MnO_2 were expected to be advantageous in FCB system because the entire MnO_2 surface is exposed to the electrolyte. A novel method to synthesize λ-MnO_2 coated carbon fibers (CF) was introduced in this chapter and the applicability of fibrous electrodes in FCB systems was evaluated.

5.2. Experimental

As was shown in Chapter 2, cations play an important role during synthesis of different MnO_2 crystal structure. To obtain λ-MnO_2, most synthesis routes employed by other researchers are based on a two-step process, in which first spinel structured $LiMn_2O_4$ is synthesized, and subsequent Li ion removal which sustains the spinel structure and creates λ-MnO_2 [46,47,110]. λ-MnO_2 with different surface areas were prepared as follows. As a reference, commercial $LiMn_2O_4$ was received from Mitsui Kinzoku (BET surface area: 0.4 m^2/g) and treated in a 0.1 M nitric acid solution for 24 h to obtain λ-MnO_2. This material is named commercial λ-MnO_2 and is the same as in previous chapters. In another method, first, β-MnO_2 was synthesized by hydrothermal treatment of a $NaMnSO_4$:$MnSO_4$ = 2:3 solution in milliohm water at 160°C for 3 h according to Chapter 2. β-MnO_2 was then transformed into $LiMn_2O_4$ by dispersing 1 g of β-MnO_2 in a LiOH solution (molar mass of MnO_2:Li = 1:1), stirring for 30 min, adding 0.2 g of glucose and hydrothermally treating for 24 h at 180°C. To improve the crystallinity, the sample was then heated to 700°C. Finally, the sample was delithiated to obtain micro λ-MnO_2. The third sample was synthesized as follows: first, poorly crystalline $LiMn_2O_4$ was synthesized according to the combustion method [111]. For this, 2 g starch was dissolved in 50 ml milliohm water and then 0.1 mol $Mn(NO_3)_2 \cdot 6H_2O$ and 0.1 mol $LiOH \cdot H_2O$ were added while stirring the solution at ca. 100°C until a thick gel was obtained. This gel was then added into an oven at 120°C for the combustion to occur. The fine powder was then calcined at 500°C for 3h and after cool-down dispersed in a LiOH solution, to which glucose was added according to the micro λ-MnO_2 sample. The dispersion was then treated hydrothermally at 180°C for 24 h and filtered. Delithiation was conducted equivalently to the previous samples. The final powder is named nano λ-MnO_2.

For the synthesis of λ-MnO_2 coated CF, a three-step process was conducted. First, γ-MnO_2 was deposited on CF (Toho Tenax, Japan) in a Mn ion containing bath, similar to previous work [21]. Briefly, MnO_2 was deposited anodically in a bath containing $MnSO_4$ (0.66 M) and H_2SO_4 (0.34 M) onto the CF at a current density of 8 mA/cm^2 for 4 h. Thereafter, the γ-MnO_2 covered CF were transformed into $LiMn_2O_4$ covered CF by adding the fibers into a autoclave that contained a LiOH solution (80 ml, Li:Mn = 1:1) and then adding 0.2 g of glucose, which was based on the transformation synthesis introduced in the previous chapter. The autoclave was then sealed and heat-treated for 24 h at 180°. After naturally cooling the autoclave down, the fibers were removed from the solution and carefully washed with milliohm water. The fibers were then added into a nitric acid solution (pH 1) to remove the lithium ions from the crystal lattice. Finally, the fibers were washed again carefully and dried overnight at 80°C.

The same apparats as in previous chapters has been used for analysis of the resulting pristine materials and electrodes under FCB mode, fuel cell mode, and battery mode. In addition, an SEM with a higher resolution (JSM-7000F, JEOL, Japan) was used to better analyze the nano-sized samples and obtain energy-dispersive X-ray spectroscopy (EDX) maps.

5.3. Results and discussion

5.3.1. Micro- and nano-sized λ-MnO_2

Characterization

The SEM images of all samples at different magnifications are shown in Fig. 5.1. It can be seen that the particle size varied greatly among the different samples. In commercial λ-MnO_2, the well-shaped octahedra were up to several micrometers in diameter. In micro λ-MnO_2, the size distribution was fairly narrow with most particles having a diameter of approximately 1

μm. The smallest particles were found in nano λ-MnO_2, where all particles were observed to be below 100 nm.

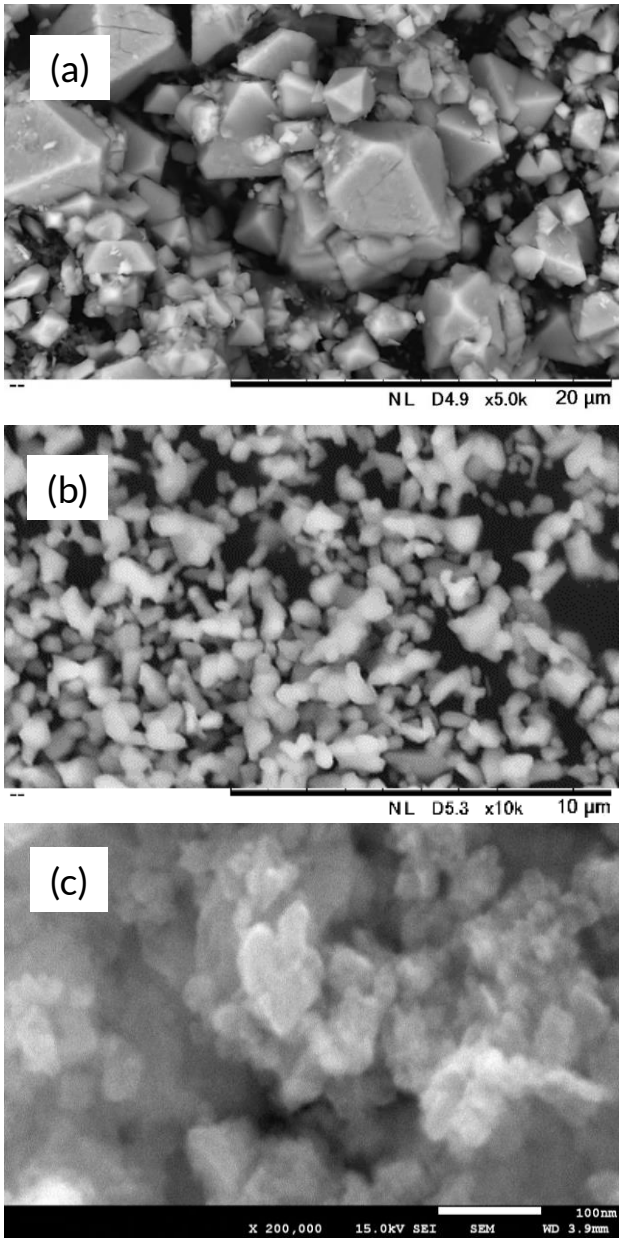

Fig. 5.1: SEM images of (a) "commercial", (b) "micro", and (c) "nano" λ-MnO_2 at different magnifications.

The measured BET surface areas reflect these observations and are summarized in Table 5.1. As the particle size decreased, the surface area increased. The surface area difference between commercial and micro λ-MnO_2 was surprisingly small, considering that the former

contained particle diameters that were much larger. It is suggested that during delithiation, particles develop cracks, as can be seen on particles in Fig. 5.1 (a), and other morphological changes, as shown by Shao-Horn et al. [112], that increase the surface area. This also explains why the surface area of the commercial particles increased from 0.4 m^2/g to 14.5 m^2/g after delithiation. By far the highest surface area was obtained in nano λ-MnO_2.

Table 5.1: BET surface area of selected samples

Sample	Surface area [m^2/g]
Commercial	14.5
Micro	23.1
Nano	77.1

The XRD patterns are shown in Fig. 5.2. The highest peaks were observed in commercial λ-MnO_2, without any impurities. In micro λ-MnO_2, all λ-MnO_2 could be identified, however, impurities of Mn_3O_4 were observed. This phase may have been created during heat-treatment at 700°C because insufficient amounts of lithium ions may have diffused into the β-MnO_2 during hydrothermal treatment. It is probable that if there was a lack of lithium ions, the spinel structure could not be established and the manganese oxide broke down into Mn_3O_4 during heat treatment. Lastly, in nano λ-MnO_2, no impurities were found and a fairly well-phased λ-MnO_2 structure was observed. The intensity of the peaks was lower than in the other samples which was likely due to the small particle size that inevitably led to a more amorphous phase.

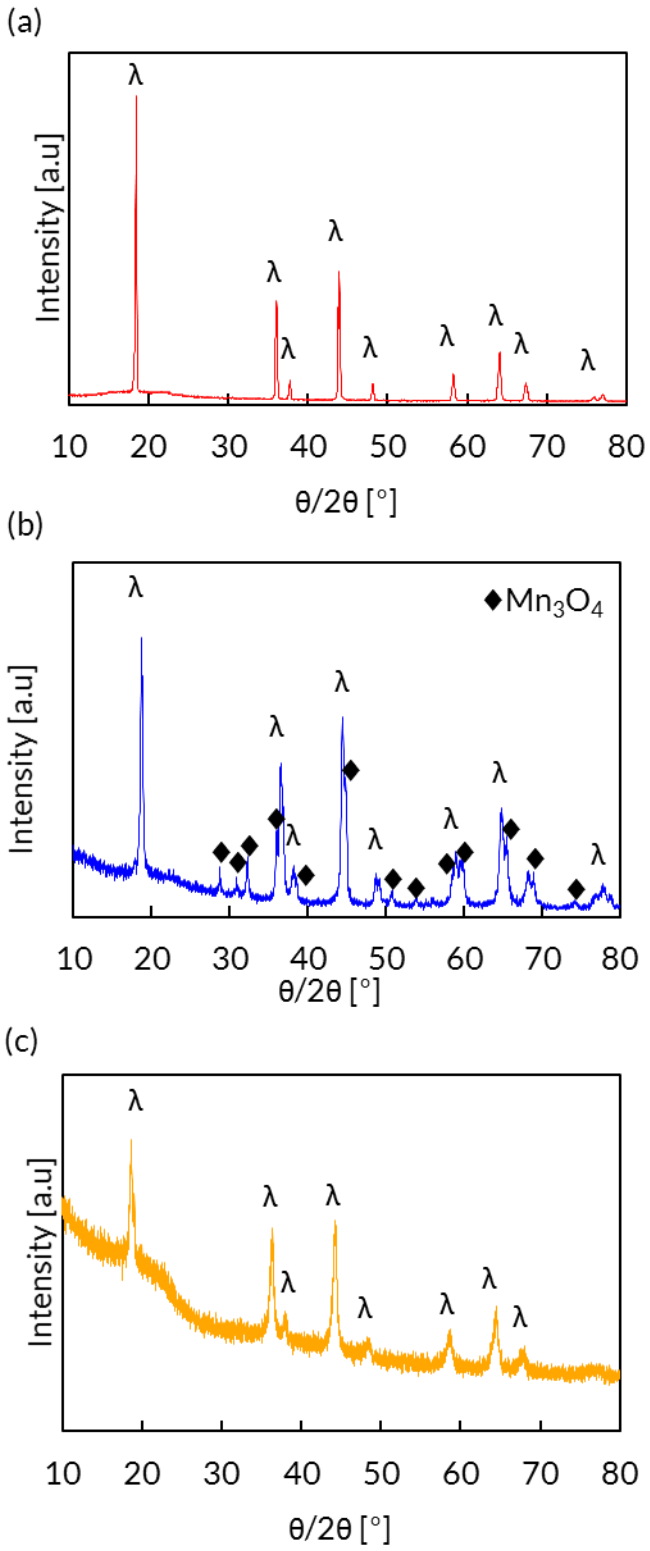

Fig. 5.2: XRD patterns of (a) “commercial”, (b) “micro”, and (c) “nano” λ-MnO_2

Chemical charging with oxygen

To analyze the chemical charge rate with oxygen, the samples were first completely discharged electrochemically (equivalent to previous chapters), then exposed to an oxygen saturated electrolyte and finally discharged electrochemically under ambient conditions at 30.8 mA/g (0.1 C) until -0.4 V vs. Hg/HgO. The electrochemical discharge curves are shown in Fig. 5.3. It was found that as the particle surface area increased, the regenerated capacity after oxygen charging increased accordingly. The regenerated capacities for commercial, micro, and nano λ-MnO_2 were 36.7 mAh/g (11.9% of the theoretical capacity), 58.2 mAh/g (18.9%), and 105.0 mAh/g (34.1%), respectively.

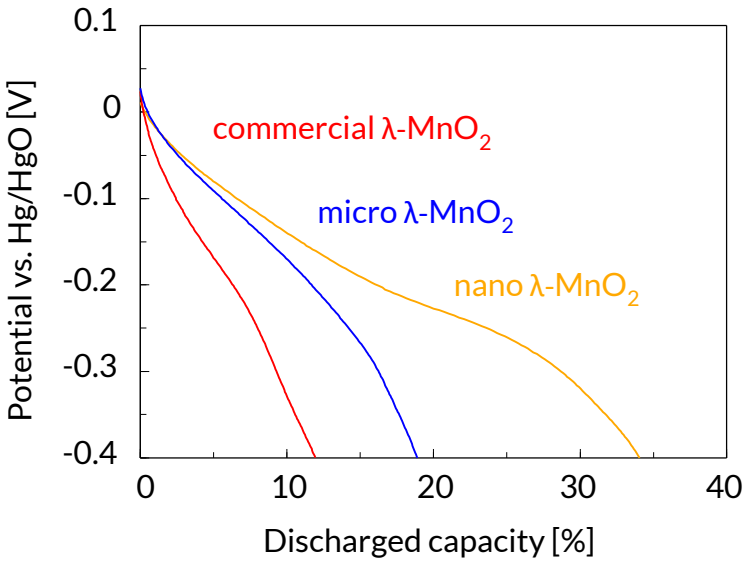

Fig. 5.3: Electrochemical discharge curves of selected samples after 1 h oxygen charge at 1.0 MPa

This result thus supports the previous claim that increasing the surface area is a promising strategy to accelerate the chemical charging rate of λ-MnO_2 with oxygen. The first reason why increasing the surface area led to increased chemical oxygen charge rate was due to a higher availability of active sites. The higher the surface area, the more Mn^{3+} sites are available for oxidation with oxygen. The second reason was that increasing the surface area led to shorter diffusion paths which allowed for faster bulk MnOOH oxidation.

Nevertheless, it has to be noted that the surface specific charge rate was not equal among the different samples. The surface specific charged capacity for commercial, micro, and nano λ-MnO_2 were 3.53, 2.52, and 1.36 mAh/m^2, respectively. It is suggested that four reasons accounted for that observation, namely crystallinity, actual surface area, doping, and nature of diffusion. Firstly, XRD analysis showed that the samples with smaller particles had a poorer crystallinity than the commercial material. The amorphous phase decreased the availability of surface λ-MnO_2 and may thus have decreased the charge rate due to a potentially lower activity of amorphous MnO_2 compared to λ-MnO_2. Secondly, the surface area measurement was based on nitrogen adsorption method, which may have suggested a higher surface area than the actual surface area reachable by electrolyte and dissolved oxygen. Thirdly, doping of the commercial material might have accelerated the chemical charge rate. It was found that the commercial material contained considerable amounts of Mg. More details are shown in Appendix C. Lastly the nature of diffusion caused a non-linear behavior between surface area and charged capacity, as shown below.

The mass diffusion can be described according to Fick's second law as:

$$\frac{\partial c(t)}{\partial t} = D\Delta c. \qquad (5.1)$$

Whereby c(t) is the time dependent concentration (in our case of protons) [mol/cm^3], t is the time [s], D is the (proton) diffusion coefficient [cm^2/s], and Δ is the second derivative. Assuming that all particles are spherically shaped, eq. 5.1 can be represented as:

$$\frac{\partial c}{\partial t} = \frac{1}{r^2}\left(\frac{\partial}{\partial r}\left(Dr^2\frac{\partial c}{\partial r}\right) + \frac{1}{\sin\theta}\frac{\partial}{\partial \theta}\left(D\sin(\theta)\frac{\partial c}{\partial \theta}\right) + \frac{D}{\sin^2\theta}\frac{\partial^2 c}{\partial \phi^2}\right). \qquad (5.2)$$

It can be assumed that there is not angular variation of the concentration, wherefore the equation can be simplified to:

$$\frac{\partial c}{\partial t} = \frac{1}{r^2}\frac{\partial}{\partial r}\left(Dr^2\frac{\partial c}{\partial r}\right). \quad (5.3)$$

It was shown by Crank [106] that for a constant diffusion coefficient and an initially uniform concentration throughout the particle, integration of this equation yields:

$$\frac{c-c_0}{c_{surf}-c_0} = 1 + \frac{2a}{\pi r}\sum_{n=1}^{\infty}\left(\frac{(-1)^n}{n}\sin\left(\frac{n\pi r}{a}\right)\left(\exp\left(-\frac{Dn^2\pi^2 t}{a^2}\right)\right)\right). \quad (5.4)$$

Thereby c is the mean concentration of protons [mol/cm^3], c_0 is the proton concentration at the beginning [mol/cm^3], c_{surf} is the proton concentration at the surface [mol/cm^3], a is the particle diameter [cm], r is the observed radius of the particle ($0 < r < a$) [cm], D the diffusion coefficient [cm^2/s], and t the time [s].

Under the assumption that during chemical charge only proton diffusion is the rate limiting step (which is not the case as shown in Chapter 3 during the first tens of seconds, but is likely a valid approximation), eq. (5.4) allows for an alternative method to calculate the diffusion coefficient D. For all three samples, the particle radius was calculated based on the BET surface area and under the assumption of a perfect spherical shape, the apparent radius a can be calculated as follows:

$$a = \frac{3}{\delta \cdot A}. \quad (5.5)$$

Whereby δ is the density [g/cm^3] and A is the specific surface area [cm^2/g]. Because the charged capacity and charge time (1 h) were known, the diffusion coefficient could be calculated numerically with equation (5.4). The results are summarized in Table 5.2.

Table 5.2 Calculated diffusion coeficient for different materials

	a [10^{-6} cm]	Charged capacity [mAh/g]	D [10^{-16} [cm^2/s]
Commercial	4.138	11.9	0.405
Micro	2.597	18.9	0.369
Nano	0.778	34.1	8.32

The diffusion coefficients lie within the values reported by others and are very similar among commercial and micro λ-MnO_2, but higher for nano λ-MnO_2. Also all values are approximately 2 – 3 orders of magnitude lower than the diffusion coefficient calculated with EIS analysis in Chapter 2. Although surprising, reports by others also show very high differences of diffusion coefficient among the same crystal structures [93]. It can be speculated that different diffusion coefficients are measured due to differences of the crystal composition (e.g. due to impurities), different crystallinity, difficulties in measuring the surface area, simplifications, etc. Simplifications include here the assumption that the particles are perfect spheres, that only diffusion dictates the proton concentration and that the diffusion coefficient is independent of proton concentration, which was found to not be the case by others [109].

With these values, the proton concentration distribution of nano λ-MnO_2 at different times could be calculated as shown in Fig. 5.4. The x-axis represents the radius of the particle (nominalized to 1) and the y-axis shows the nominalized proton density at every radius. The proton distribution is shown for 100 s, 1000 s, 1 h, 3 h, and 10 h. The curve was found to be sensitive to changes in diffusion coefficient, particle diameter and time.

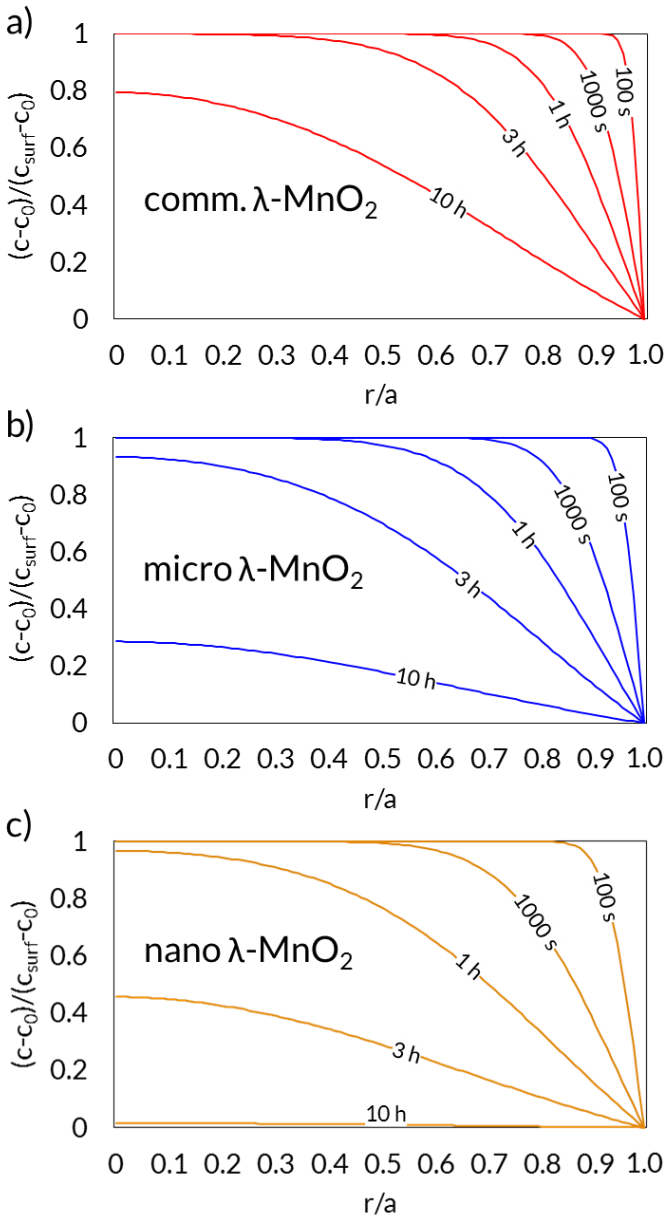

Fig. 5.4: concentration variation in a particle at different times

One can see that although at 1 h the charged capacity in nano λ-MnO_2 was much higher than in commercial and micro λ-MnO_2, at 10 h, the difference became much smaller as the particles approached complete charge. Thus, a linear dependency of charged capacity and surface area for any arbitrary charge duration was impossible.

Cyclability Analysis

In order to analyze the effect of surface area on the proton diffusion, all samples were electrochemically cycled at a constant charge of 0.2 C and discharged at different C-rates. No charge cut-off potential was implemented and the discharge cut-off potential was set at -0.4 V vs. Hg/HgO.

During the first cycles, nano λ-MnO_2 showed the highest capacity. It is probable that the small particle size which led to short diffusion paths also allowed for a more complete discharge at 0.2 C than the other materials. Accordingly, the initial capacity of micro λ-MnO_2 was higher than that of commercial λ-MnO_2. For all samples, the discharge capacity decreased as the discharge rate increased. At 2.0 C, 5.0 C and 10.0 C the discharge capacities of micro λ-MnO_2 was very similar to commercial λ-MnO_2. Only in case of nano λ-MnO_2 the capacity was considerably higher than commercial λ-MnO_2. At the fifth cycle at 10.0 C discharge rate, the discharge capacities were 4.96 mAh/g, 5.83 mAh/g, and 15.44 mAh/g for commercial, micro and nano λ-MnO_2, respectively. It is likely that the comparatively high discharge capacity at 10.0 C of nano λ-MnO_2 was due to the short diffusion path. As noted previously, the characteristic proton diffusion, defined as $A\sqrt{D}$, is linearly dependent on the surface area, which can explain why the capacity at high C-rates was highest in nano λ-MnO_2

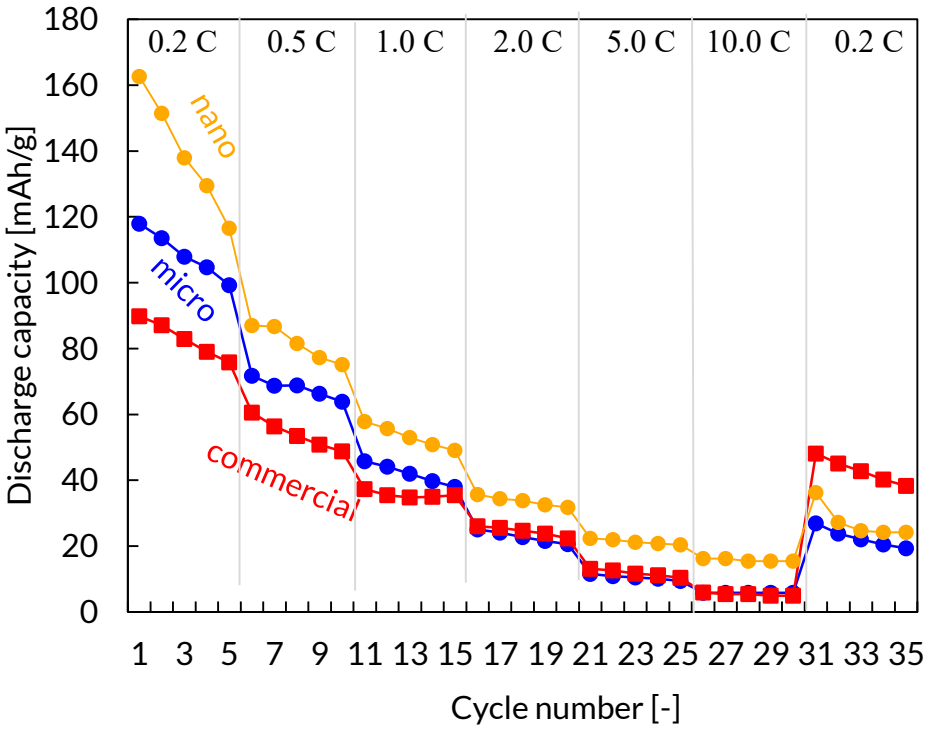

Fig. 5.5: Discharge capacity of selected samples at 0.2 C charge and different discharge rates

After decreasing the cycling rate to 0.2 C in the 31st cycle, the discharge capacities of commercial, micro and nano λ-MnO_2 were 48.2 mAh/g, 27.0 mAh/g and 36.3 mAh/g, respectively. Commercial λ-MnO_2 thus showed the best stability and a somewhat similar stability was observed between micro and nano λ-MnO_2. To identify the source of degradation, the crystal structure after electrochemical cycling was analyzed via XRD. It was found that both nano and micro λ-MnO_2 completely transformed into an amorphous state and that no peak referring to any Mn containing compound could be identified. In comparison, commercial λ-MnO_2 still showed the initial peaks, with a slight transformation into δ-MnO_2, as already shown in Chapter 2. Nevertheless, its peaks are considerably weaker than the pristine materials, wherefore it is likely that also this material became amorphous during electrochemical cycling.

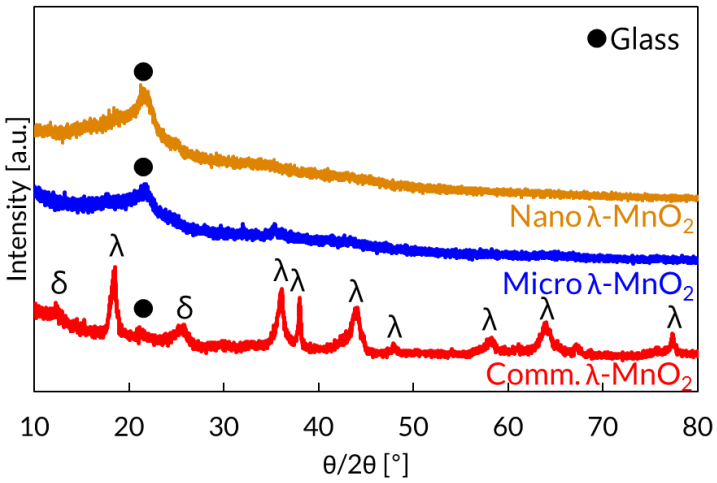

Fig. 5.6: XRD of nano, micro and commercial λ-MnO_2 after electrochemical cycling

Several reasons are likely to have caused a faster amorphization of the small particles. Firstly, because of the smaller diffusion path, more of the electrochemical material was protonated and deprotonated during cycling, thus leaving less bulk material non-discharged. In commercial λ-MnO_2, it is likely that some of its bulk material was not cycled during battery mode wherefore the spinel structure could be sustained. This bulk material likely resulted in the characteristic λ-MnO_2 peaks during XRD analysis. Secondly, another possible reason for the degeneration is a non-optimized MnO_2:CB:EVA ratio. For all samples, the same ratio was used (100:15:10 wt.%), however, due to the increased surface area, particularly in nano λ-MnO_2, an increased amount of binder may be required to obtain a stable electrode. In addition to that, mixing in a mortar may not have led to a well-mixed slurry for nano particles and different manufacturing methods and/or binders might need to be introduced to overcome these problems.

The increased resistance between current collector and active material in nano λ-MnO_2 could be measured with EIS. The measured solution resistance R_s, which is affected by the contact resistance at the interface between electroactive material and current collector [113]

was identified to be 0.07 Ω in commercial λ-MnO_2 and 0.11 Ω in nano λ-MnO_2. Smaller sized particles therefore result in a higher contact resistance between electroactive material and current collector.

Oxygen Reduction Reaction

To assess the capabilities of all samples to run under fuel cell mode, the samples were first discharged to -0.4 V vs. Hg/HgO, then exposed for 5 h to oxygen bubbling at 1.0 MPa at open circuit, and finally different currents were applied for 1 h according to previous chapters. The I-V curves of all three samples are shown in Fig. 5.7. The commercial material showed a current density of 17.4 mA/cm^2 at a potential of -0.10 V vs. Hg/HgO. The micro λ-MnO_2 achieved a current density of 35 mA/cm^2 at -0.23 V vs. Hg/HgO. The best performance was found in nano λ-MnO_2, which achieved a current density of 70 mA/cm^2 at a potential of -0.15 V vs. Hg/HgO.

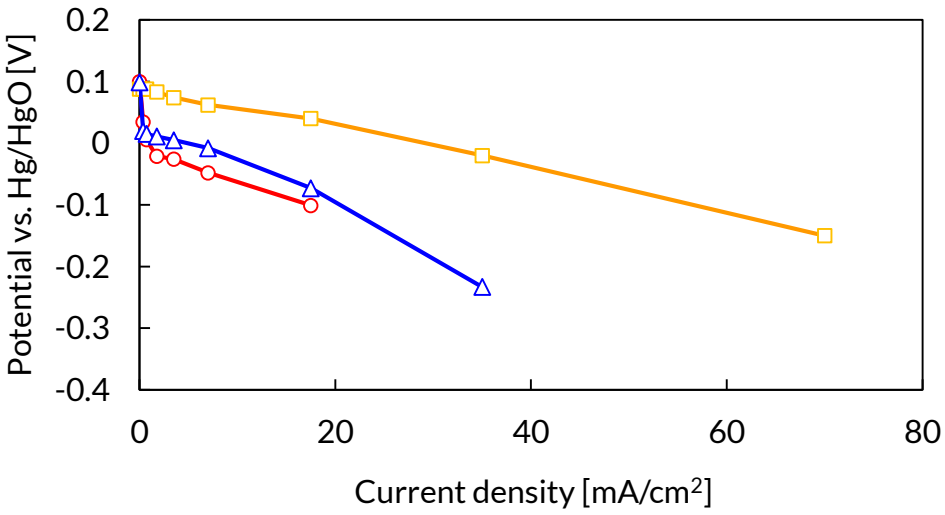

Fig. 5.7: I-V curves of selected samples

The current density of λ-MnO_2 was therefore directly dependent on the surface area. Also for ORR, a higher surface area resulted in more active sites where the reactions could occur. Nevertheless, the increase of ORR does not increase linearly with surface area. Three of the

previously mentioned reasons are probable for this observation. Firstly, the crystallinity was lower in micro and nano λ-MnO_2 than in commercial λ-MnO_2. The higher amorphous proportion (in case of micro λ-MnO_2 also the presence of Mn_3O_4) is likely disadvantageous for the ORR rate. Secondly, the surface area reachable by the electrolyte and oxygen diffused in it may be lower than the BET surface area. Lastly, also for ORR, Mg doping of commercial λ-MnO_2 might have improved its performance due to a lower charge transfer resistance.

Nano-sizing λ-MnO_2 has thus been shown to be a promising strategy in order to improve the performance of the electroactive material in terms of chemical charging with oxygen, electrochemical cycling at high C-rates, and oxygen reduction reaction. In the second part of this chapter, the performance of λ-MnO_2 was tried to be further improved via a fibrous electrode design.

5.3.2. Fibrous λ-MnO_2

Characterization

The λ-MnO_2 covered CF are shown in Fig. 5.8. It can be seen that the entire fibers were covered with λ-MnO_2 which consisted of 2 dimensional plates. The nano-sized structure was expected to be advantageous for application as positive electrode in FCB systems because such a structure allowed for a large availability of active surface sites and small diffusion length. The fact that no binder was required was expected to boost the chemical charge rate as no MnO_2 at the surface was inactivated due to coverage with binder.

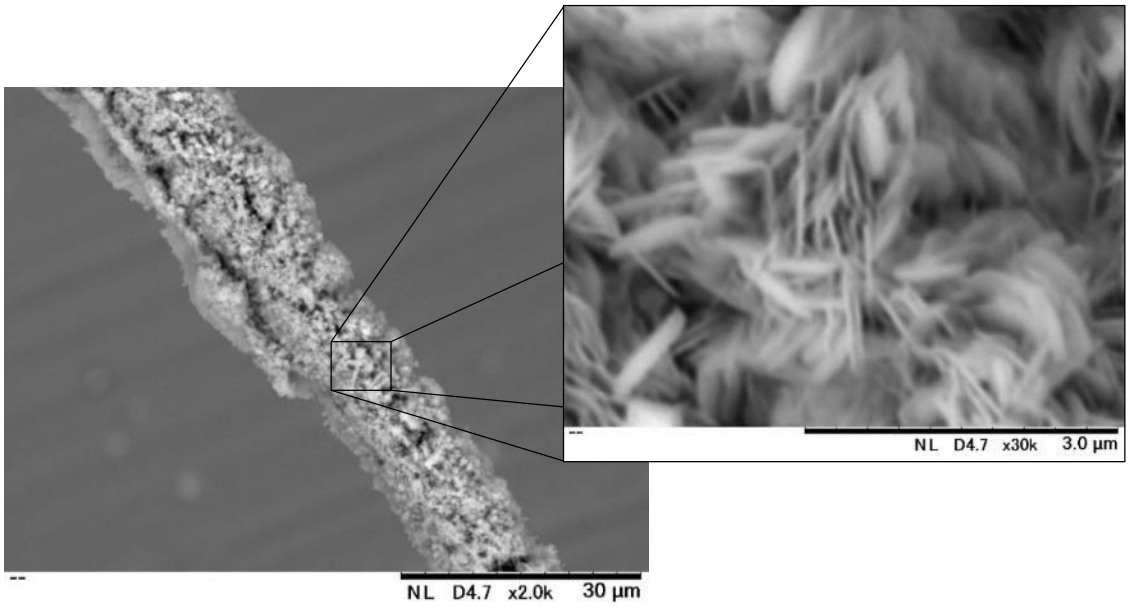

Fig. 5.8:SEM images of λ-MnO_2 covered carbon fibers at two different magnifications

Two different kinds of electrodes were fabricated for analysis of chemical oxygen charge rate and electrochemical cycling. For chemical oxygen charge tests, the λ-MnO_2 covered CF were pressed between two nickel foam sheets at 10 MPa to minimize mechanical stress (bending) due to oxygen bubbles during chemical oxygen charging. For electrochemical cycling test, the fibers were not pressed between two nickel foam sheets which allowed for better post-cycling analysis.

In order to analyze the crystallinity, XRD analysis was conducted and the diffraction pattern of the λ-MnO_2 covered CF is shown in Fig. 5.9. All λ-MnO_2 peaks were present and the peaks were intense, suggesting a good crystallinity. Additional peaks were observed which could be assigned to the glass substrate onto which the fibers were attached for XRD analysis. Also a fairly wide peak was observed at around 24° which was due to the carbon fibers. An unidentifiable peak at 65.2° could not be attributed to a material and it is unclear which phase this peak belongs to. It can also be seen that the peak at 44.5°, which refers to the (440) phase of λ-MnO_2, was the most intense peak. This is different compared to the samples in previous

samples, in which the (110) phase was the most prominent one. Also according to JCPDS card no. 44-0992, the peak at (110) should be the most intense one. It is thus likely that the (440) phase is the phase which is exposed at the surface of the λ-MnO_2 plates. The exposed facet can have large effect on catalytic capabilities, as was shown by various researchers for different materials [54,114,115].

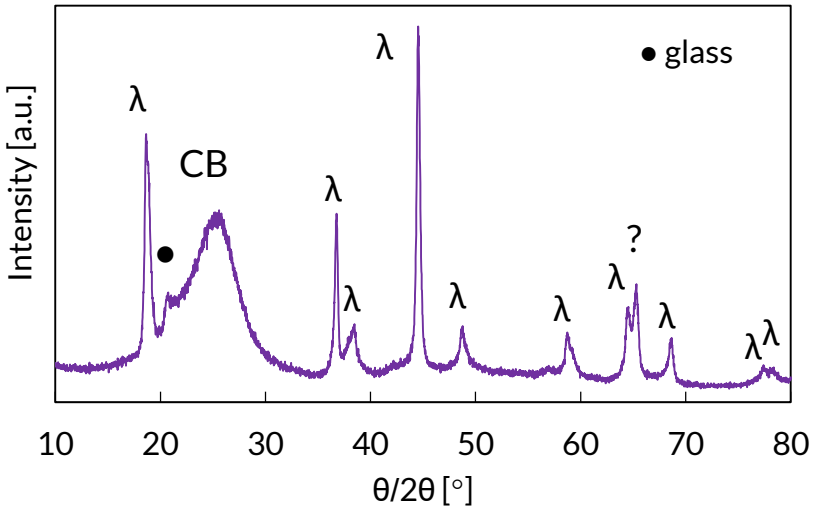

Fig. 5.9: XRD pattern of λ-MnO_2 covered carbon fibers

Chemical charging with oxygen

After assembly of the three-electrode cells, the CF electrode was fully discharged, chemically charged with oxygen at 1.0 MPa and electrochemically discharged at ambient conditions at 0.1 C equivalent to the protocol used in this and previous chapters. The electrochemical discharge curves of the λ-MnO_2 CF is shown in Fig. 5.10. The regenerated capacity of λ-MnO_2 CF was determined at 49.3%, which was more than nano-sized λ-MnO_2 (34.1%) and commercial λ-MnO_2 (11.9%). The reason for these results are likely three-fold. Firstly, the high surface area of the λ-MnO_2 deposited on CF led to a high amount of active sights for chemical charging. Secondly, the 2 D structure results in very short diffusion paths which was shown in previous chapters to be crucial for fast chemical oxygen charging. Lastly,

the fibrous electrodes did not require any binder, which avoided covering the active surface area with inert material.

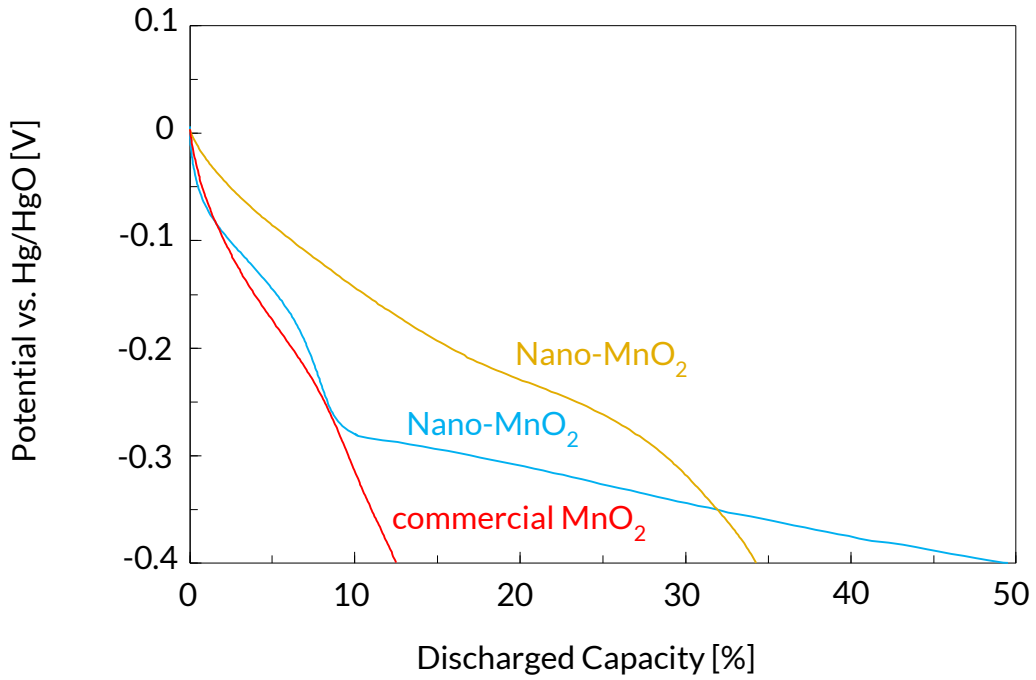

Fig. 5.10: Electrochemical discharge curves of different electrodes after 1 h chemical oxygen charge at 1.0 MPa

It can also be seen, however, that the average potential was fairly low. A shoulder of the discharge curve was observed at ca. -0.12 V vs. Hg/HgO, followed by a drop in potential and a fairly flat remaining curve from ca. -0.28 V vs. Hg/HgO until the discharge cut-off voltage of -0.4 V vs. Hg/HgO. This was considerably different compared to commercial and nano λ-MnO_2 and suggested high losses. Therefore, electrochemical cycling analysis was conducted to get a better understanding.

Cyclability analysis

To assess the fiber electrode under battery mode, the electrodes were electrochemically cycled at different C-rates. The discharge cut-off voltage was set at -0.4 V vs. Hg/HgO and the charge was terminated at 100% of the theoretical capacity. The discharge capacity of the

different cycles is shown in Fig. 5.11, together with the results of commercial λ-MnO_2 as a reference. The capacity was found to be satisfyingly high during the first cycles. It is likely that the 2D plate structure was also beneficial for battery mode due to the short diffusion path. This allowed for an almost complete discharge at low C-rates. Upon increasing the discharge rate, however, the capacity drop was considerably higher compared to the pasted, commercial λ-MnO_2. At discharge rates of 2.0 C or higher, the capacity was much lower than the commercial material.

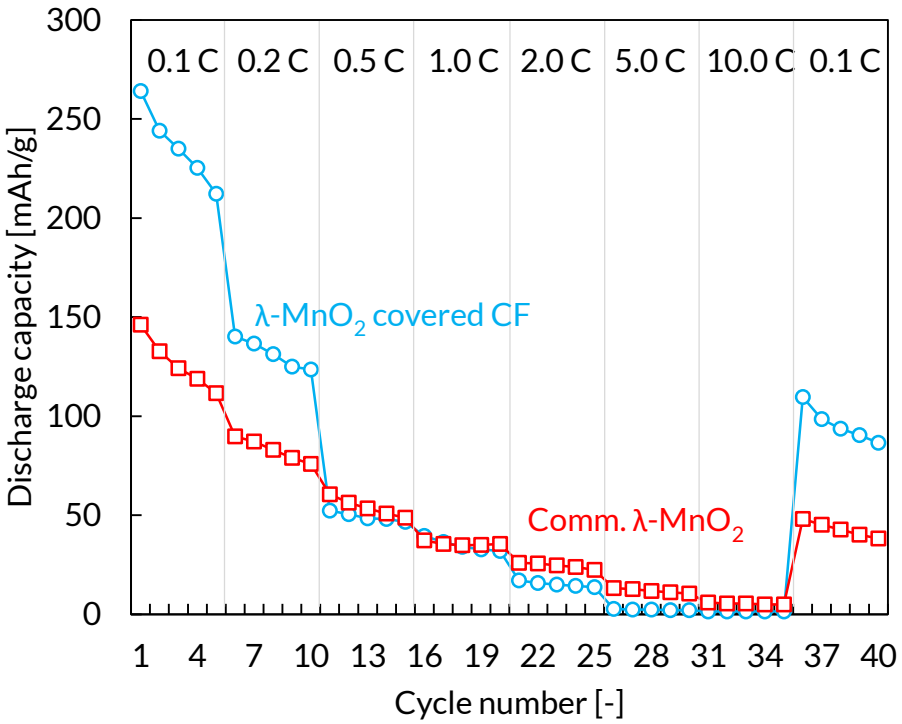

Fig. 5.11: Electrochemical discharge capacities of the fibrous electrode compared to a pasted electrode

For both the chemical oxygen charging and electrochemical cycling tests, a high loss likely caused the low discharge potential and capacity, respectively. In order to verify this claim, SEM images of the fibers were taken after cycling. As shown in Fig. 5.12, it was observed that the connection between λ-MnO_2 and CF was poor which resulted in a considerable gap between the electroactive material and current collector. This in turn likely resulted in high ohmic losses,

which caused the low potential during discharging and accordingly a small discharge capacity at high electrochemical discharge rates.

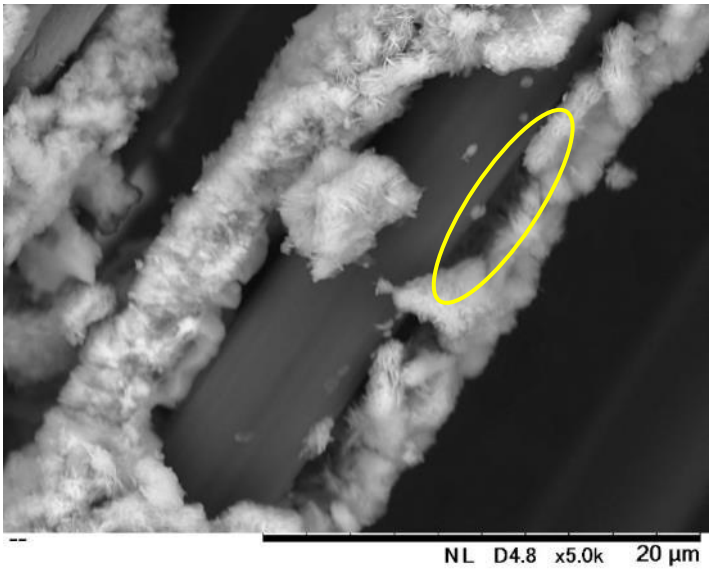

Fig. 5.12: SEM images of the λ-MnO2 covered carbon fibers after electrochemically cycling.

When handling the λ-MnO_2 covered CF, a lot of care had to be taken to keep the fibers from bending. While CF are fairly flexible, the λ-MnO_2 covered CF were found to be barely bendable due to the brittleness of MnO_2, resulting in easily seceding active material.

5.4. Conclusions

In this chapter novel active materials, namely micro- and nano-sized λ-MnO_2, were synthesized and their performance was analyzed under FCB, fuel cell, and battery mode. It was found that decreasing the particle size was a very effective strategy to improve the performance of the electrode. Nano-sized λ-MnO_2 could be chemically charged with oxygen to 34.1% of its initial capacity within 1 h. In comparison, originally used γ-MnO_2 (a = 51.5 m^2/g) required a charge duration of 48 h to achieve a similar capacity. This points out the importance of both the surface area and crystal structure on the chemical charge performance.

Furthermore, nano λ-MnO_2 showed a considerably improved ORR rate, which was mainly due to the higher surface area, and during electrochemical cycling at high discharge rates, nano λ-MnO_2 showed better performance than the other materials. It was also found, however, that electrochemical stability of the nano-sized materials was somewhat poor and needs to be improved in future work. Degradation was mainly ascribed to amorphization of the electroactive material.

This result pointed out that besides proton diffusion, also a high availability of surface MnO_2 is crucial for chemical oxygen charging. As such, it was claimed that also the binder of pasted electrodes decreased the availability of active surface sites. In the second part of this chapter, therefore, an alternative electrode design, which omitted the need for binders, was analyzed.

λ-MnO_2 covered CF were successfully synthesized by first plating γ-MnO_2 onto CF and subsequent transformation of the active material into λ-MnO_2. Chemical oxygen charging tests showed very promising results in terms of capacity which was suggested to be because of the high surface area, short proton diffusion lengths, and inexistence of binder. Nevertheless, improvements have to be made in the future in terms of mechanical stability. Electrochemical cycling showed good performance at low C-rates but poor capacity retention upon increasing the C-rate. It was found that a tight contact between electroactive material and CF current collector is crucial to enable fast electrochemical discharge and long cycle life. Novel synthesis methods thus need to be implemented in order to obtain fully functional λ-MnO_2 covered CF.

A different route to improve the performance of the electroactive material is by supplementing it with a cyatalyst. As such, nano-sized λ-MnO_2 was modified by silver

deposition to improve the reaction rates at the surface. Silver was evenly deposited onto nano λ-MnO_2 by sensitizing latter in a NaOH bath. The Ag-covered λ-MnO_2 showed an improved oxygen reduction reaction rate compared to the Ag-free sample, but the silver reduced the amount of active sites for MnOOH oxidation to occur, thus resulting in a decreased chemical oxygen charge rate. The experimental work and results of silver containing nano λ-MnO_2 are shown in Appendix D.

Chapter 6 Conclusions and Outlook

6.1. Conclusions

Prior to this work, it was found that the chemical charging of the MH negative electrode with hydrogen gas was considerably faster than chemical charging of the MnO_2 positive electrode with oxygen gas. Within 10 min, more than 70% of the theoretical capacity of metal hydride could be charged with hydrogen gas [22]. In contrast to that, within 1 h only 13% of the theoretical capacity of MnO_2 was charged with oxygen [20]. It was claimed that the chemical oxygen charging rate of MnO_2 was constant and that with an oxygen supply of 1.0 MPa, the electrode could be fully charged within 10.3 h. A preliminary test in this dissertation showed however that this was not the case and that the chemical charge rate was even slower than expected. Thus, the objective of this work was to improve the oxygen charging mechanism of MnO_2. This was achieved by first analyzing different crystal structures, which helped identify potential candidates for subsequent research, followed by understanding of the chemical oxygen charge mechanism and finally synthesizing novel electrodes to accelerate the chemical oxygen charging process.

In Chapter 2, various morphologies were investigated to overcome the limitations of the previously used commercial γ-MnO_2. Four different crystal structures, namely α-, β-, γ-, and δ-MnO_2 could be synthesized via a redox method. By altering the temperature and KCl content (the K ions were found to work as a template), different morphologies could be obtained. Seven different materials, including commercial γ- and λ-MnO_2 as reference, were then electrochemically cycled in battery mode in order to assess their capacity and cyclic stability. It was found that α-MnO_2 was unsuitable for FCB systems due to transformation into non-

rechargeable Mn_3O_4. β-MnO_2 was fairly stable, however, its capacity was low. δ-MnO_2 also had a low capacity and it was found to slowly transform into Mn_3O_4 as well.

Additionally, the effect of the particle shape was analyzed. The γ-MnO_2 synthesized in-house consisted of thin 1D shapes <100 nm which was different compared to commercial γ-MnO_2 which consisted of somewhat spherically shaped particles. It was found that 1D structures are unsuitable due to cluster formation in the pasted electrode which resulted in higher internal resistance. It was concluded that commercial γ- and λ-MnO_2 were the most suitable materials for subsequent work.

In Chapter 3, the charge rate during chemical charging with oxygen was analyzed. By comparing the chemical charge curve with the electrochemical charge curve, three distinct phases could be observed, namely oxygen adsorption (stage 0), surface oxidation (stage 1), and proton diffusion (stage 2). It was proposed that in stage 0, oxygen dissolved, diffused and adsorbed onto the MnO_2 particles. This phase was typically very noisy and because it took several tens of seconds until the system reached a steady-state mode, this phase was not analyzed in depth. In stage 1, surface oxidation was the rate limiting step, resulting in a constant chemical oxygen charge rate. In the last stage, proton diffusion was the rate limiting step which caused a decreasing charge rate.

Furthermore, considerable differences of the chemical charge rate were observed between γ- and λ-MnO_2, which were discussed in Chapter 4. In stage 1, the chemical charge rates were 8 mAh/(g·s) and 40 mAh/(g·s) for γ-MnO_2 and λ-MnO_2, respectively. Because the surface area of λ-MnO_2 (14.5 m^2/g) was considerably smaller than that of γ-MnO_2 (51.5 m^2/g), the surface specific chemical charge rate of λ-MnO_2 was by a factor of 17.5 higher than that of γ-MnO_2.

This result was confirmed by EIS analysis which showed a considerably lower charge transfer resistance of discharged λ-MnO_2 than discharged γ-MnO_2. The reason for the faster surface charge rate in λ-MnO_2 than in γ-MnO_2 was identified to be two-fold; firstly, it was found that γ-MnO_2 underwent strong crystal distortion, particularly due to Jahn-Teller distortion. With crystal field theory, it could be explained that such a geometrical distortion caused the high charge transfer resistance. In contrast to that, only limited crystal distortion was observed in λ-MnO_2, thus allowing for a smaller charge transfer resistance than in γ-MnO_2. Secondly, the O–H bond in λ-MnO_2 was much longer (i.e. weaker) than in γ-MnO_2, which led to easily removable protons from the λ-MnO_2 lattice. This also allowed for a fast surface charge rate.

In stage 2, i.e. bulk charging, the γ-MnO_2 was found to perform better than λ-MnO_2 which could be explained with the faster proton diffusion (defined as $A\sqrt{D}$) in γ-MnO_2. Although, it was found that the diffusion coefficient D was higher in λ-MnO_2, its smaller surface area inhibited fast proton diffusion. Thus, bulk charging was faster in γ-MnO_2 than in λ-MnO_2.

In fuel cell mode it was found that λ-MnO_2 had a higher ORR rate compared to γ-MnO_2, which was likely due to the lower charge transfer resistance in protonated λ-MnO_2 compared to protonated γ-MnO_2. In battery mode, γ-MnO_2 showed better performance at high C-rate which was suggested to be because of the faster proton diffusion. The fuel cell mode and battery mode were thus found to help understand and verify the chemical oxygen charging mechanism.

In Chapter 5, different synthesis methods were conducted to obtain λ-MnO_2 with a larger surface area. In the first method, β-MnO_2 was hydrothermally transformed into $LiMn_2O_4$ and subsequently delithiated, resulting in micro-sized λ-MnO_2. In the second method, nano-sized λ-MnO_2 was obtained by first synthesizing poorly crystalline $LiMn_2O_4$ in a combustion method,

followed by hydrothermal treatment to increase the crystallinity and surface area. As a reference material, delithiated commercial $LiMn_2O_4$ was used. The chemical oxygen charging results showed that the charge rate was directly dependent on the surface area and that with nano-sized λ-MnO_2, 34.1% of the theoretical capacity could be regenerated with oxygen after 1 h. To obtain similar charge capacity with commercial γ-MnO_2, 48 h of chemical charging was required. In addition to that, nano-sized λ-MnO_2 also showed quick ORR, high initial capacity and compared to commercial λ-MnO_2 better performance at high discharge cycling.

In order to further improve the performance of nano λ-MnO_2, the possibility of using a binder-free fibrous electrode was analyzed. λ-MnO_2 covered CF were synthesized by first depositing γ-MnO_2 onto CF, followed by transformation into $LiMn_2O_4$ and subsequent delithiation. During FCB mode, it was found that λ-MnO_2 covered CF could be chemically charged to 49.1% of the initial capacity with oxygen. Electrochemical cycling also revealed high capacities of the λ-MnO_2 covered CF but poor performance at high discharge rates. Subsequent SEM analysis showed that the connection between active material and current collector was poor, which resulted in high ohmic losses. Additional work is thus required to improve the capabilities of the fibrous electrode, but nevertheless, its fast chemical charge rate showed that this structure is very promising for FCB systems.

6.2. Recommendations for Future Work

In future work, different issues need to be tackled in order to further improve the performance of the positive electrode in FCB systems. The problem that needs to be solved first is the electrochemical degradation of λ-MnO_2 during cycling (both chemical and electrochemical cycling). A better understanding of the degeneration mechanism of λ-MnO_2 has to be gained and methods to inhibit degeneration need to be found. It has already been

found in this dissertation that partial transformation of λ-MnO_2 into δ-MnO_2 and amorphous MnO_2 occurs, but it is unclear what causes this transformation. Different strategies may need to be employed in order to overcome the degradation issue, such as doping and electrode composition. Details of these ideas and further suggestions how other improvements could be achieved are described below.

Doping

Spinel type structures, including $LiMn_2O_4$, are widely used in lithium ion batteries. Typically, pure $LiMn_2O_4$ does not show very good electrochemical cyclability in lithium ion batteries either, wherefore different modifications have been introduced. By doping with Co [116] and other metals [117,118], the stability could be considerably improved. Analyzing such strategies for the application in FCB systems may be a comparatively simple but effective method to improve the capabilities of λ-MnO_2. A preliminary study about doping is shown in Appendix C.

Composition

The composition of all pasted electrodes here was MnO_2:CB:EVA = 100:15:10 (wt.%). As the surface area of the electroactive material increases, typically also a higher binder amount is required, which in turn also requires more CB. In future work an optimized ratio of the slurry needs to be found for nano λ-MnO_2.

Particles

The nano-sized λ-MnO_2 introduced in this work showed that increasing the surface area and decreasing the particle diameter was a very effective way to improve the chemical charge rate with oxygen. The crystallinity of the synthesized material was not perfect, however,

wherefore it is probable that improving the crystallinity may further boost the capabilities of λ-MnO_2. Novel synthesis strategies for improved synthesis methods should therefore be analyzed.

Catalysts

As shown in Appendix D, silver deposition was beneficial for ORR but depositing on the surface of MnO_2 resulted in slower chemical charge rate. A different strategy to improve the ORR may be by modification of the carbon current collector. Firstly, CB could be replaced with carbon nanotubes or graphene which are known to offer very high electro conductivity. Secondly, the carbon materials could be modified to serve as catalyst. A lot of work has been done by others which show that doping of carbon nanotubes and graphene with nitrogen results in high catalytic capability towards oxygen reduction [119,120]. Such materials may be also suitable in FCB applications. This would allow for faster ORR while not negatively affecting the chemical charge rate, as the MnO_2 would not be modified.

Electrode design

Carbon fibers were shown in this work to be a promising alternative to pasted electrodes on nickel foam. To be fully functional, however, better synthesis methods have to be developed which can assure a tight connection between electroactive material and current collector. The fibrous electrodes could be further improved by synthesizing thinner carbon fibers in a woven form. The MnO_2 could then be deposited into that sheet to create an electrode that (i) has a higher ratio of electroactive material:current collector, (ii) results in low ohmic losses and (iii) is easier to handle than fibrous strings. Such an electrode was manufactured in this work already and in shown in Fig. 6.1. For details about manufacturing, see Appendix F. To date, however, only γ-MnO_2 could be obtained and no suitable method of achieving a λ-MnO_2/carbon nano fiber sheet could be achieved.

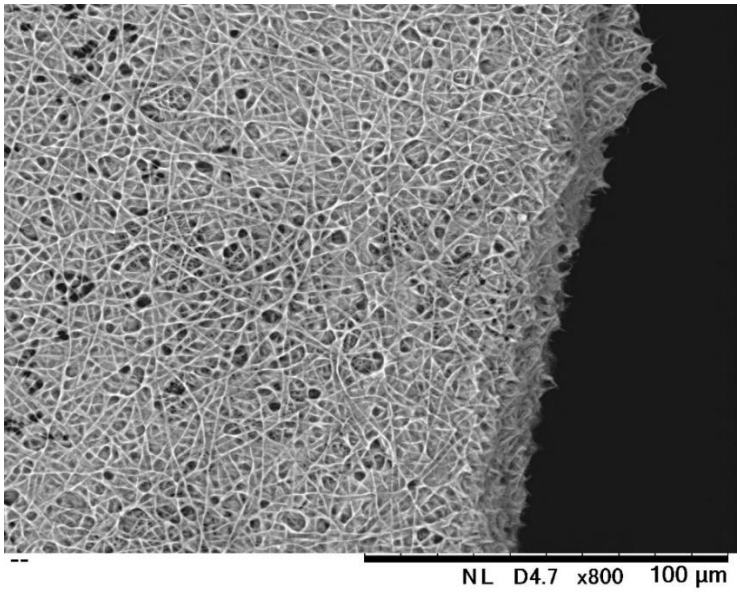

Fig. 6.1: MnO_2 deposited on a nano-CF mesh

Cell design

A lot of effort also needs to be invested to manufacture complete FCB cells. To date, the negative and positive electrodes have only been analyzed separately and no complete FCB system has been realized yet. In particular, mixing of hydrogen and oxygen gases needs to be inhibited to assure a safe, efficient, and durable operation. It is probable that an alkaline membrane needs to be inserted which can effectively separate the two gases.

In addition, solutions have to be found that can tackle the problem of a continuously diluting electrolyte due to the formation of water during fuel cell mode. Methods have to be found how the water can be removed while keeping the hydroxide ions in the electrolyte.

Appendix A – Standard Reduction potentials

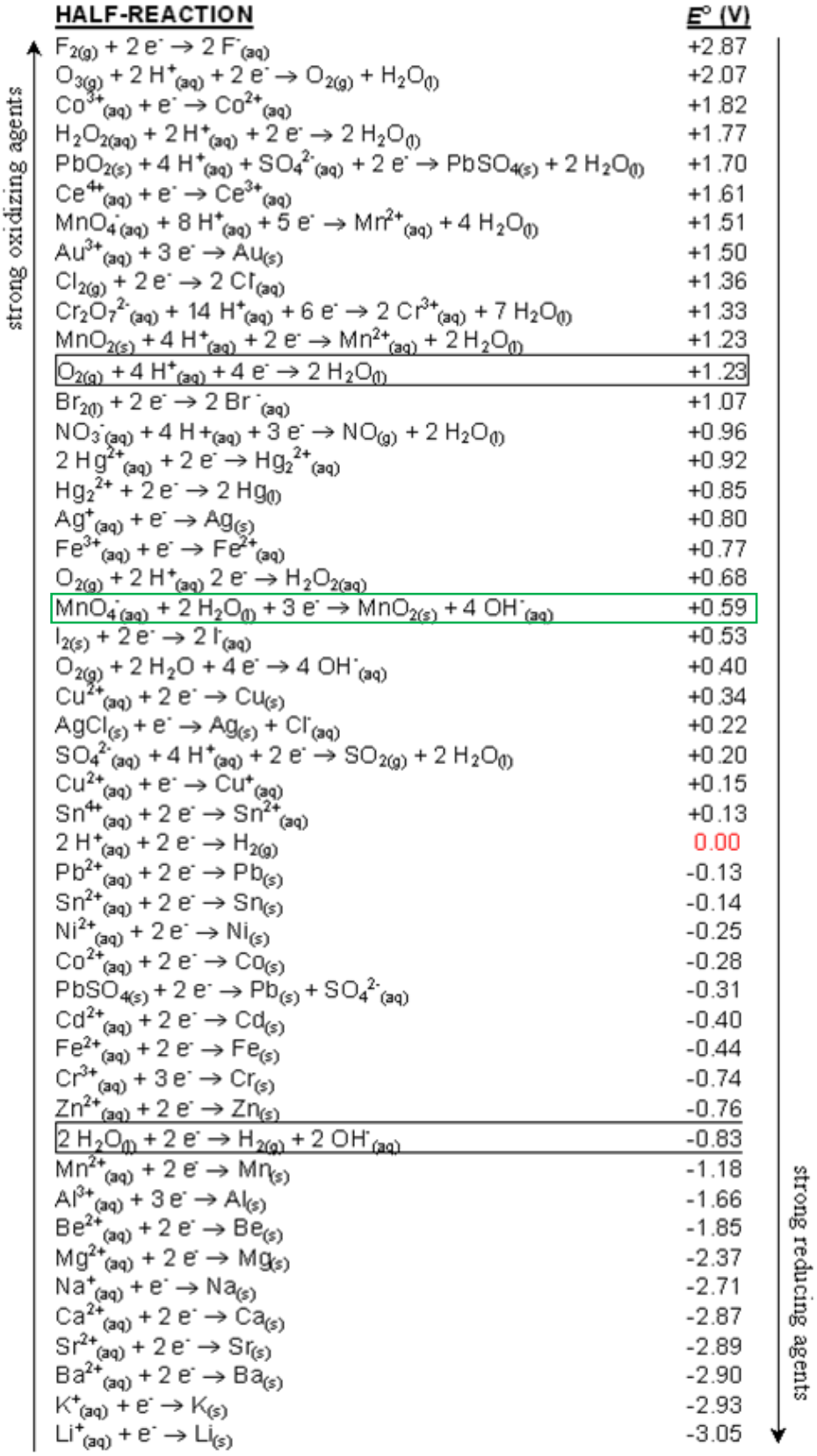

HALF-REACTION	E° (V)
$F_{2(g)} + 2\,e^- \rightarrow 2\,F^-_{(aq)}$	+2.87
$O_{3(g)} + 2\,H^+_{(aq)} + 2\,e^- \rightarrow O_{2(g)} + H_2O_{(l)}$	+2.07
$Co^{3+}_{(aq)} + e^- \rightarrow Co^{2+}_{(aq)}$	+1.82
$H_2O_{2(aq)} + 2\,H^+_{(aq)} + 2\,e^- \rightarrow 2\,H_2O_{(l)}$	+1.77
$PbO_{2(s)} + 4\,H^+_{(aq)} + SO_4^{2-}{}_{(aq)} + 2\,e^- \rightarrow PbSO_{4(s)} + 2\,H_2O_{(l)}$	+1.70
$Ce^{4+}_{(aq)} + e^- \rightarrow Ce^{3+}_{(aq)}$	+1.61
$MnO_4^-{}_{(aq)} + 8\,H^+_{(aq)} + 5\,e^- \rightarrow Mn^{2+}_{(aq)} + 4\,H_2O_{(l)}$	+1.51
$Au^{3+}_{(aq)} + 3\,e^- \rightarrow Au_{(s)}$	+1.50
$Cl_{2(g)} + 2\,e^- \rightarrow 2\,Cl^-_{(aq)}$	+1.36
$Cr_2O_7^{2-}{}_{(aq)} + 14\,H^+_{(aq)} + 6\,e^- \rightarrow 2\,Cr^{3+}_{(aq)} + 7\,H_2O_{(l)}$	+1.33
$MnO_{2(s)} + 4\,H^+_{(aq)} + 2\,e^- \rightarrow Mn^{2+}_{(aq)} + 2\,H_2O_{(l)}$	+1.23
$O_{2(g)} + 4\,H^+_{(aq)} + 4\,e^- \rightarrow 2\,H_2O_{(l)}$	+1.23
$Br_{2(l)} + 2\,e^- \rightarrow 2\,Br^-_{(aq)}$	+1.07
$NO_3^-{}_{(aq)} + 4\,H+_{(aq)} + 3\,e^- \rightarrow NO_{(g)} + 2\,H_2O_{(l)}$	+0.96
$2\,Hg^{2+}_{(aq)} + 2\,e^- \rightarrow Hg_2^{2+}{}_{(aq)}$	+0.92
$Hg_2^{2+} + 2\,e^- \rightarrow 2\,Hg_{(l)}$	+0.85
$Ag^+_{(aq)} + e^- \rightarrow Ag_{(s)}$	+0.80
$Fe^{3+}_{(aq)} + e^- \rightarrow Fe^{2+}_{(aq)}$	+0.77
$O_{2(g)} + 2\,H^+_{(aq)}\,2\,e^- \rightarrow H_2O_{2(aq)}$	+0.68
$MnO_4^-{}_{(aq)} + 2\,H_2O_{(l)} + 3\,e^- \rightarrow MnO_{2(s)} + 4\,OH^-_{(aq)}$	+0.59
$I_{2(s)} + 2\,e^- \rightarrow 2\,I^-_{(aq)}$	+0.53
$O_{2(g)} + 2\,H_2O + 4\,e^- \rightarrow 4\,OH^-_{(aq)}$	+0.40
$Cu^{2+}_{(aq)} + 2\,e^- \rightarrow Cu_{(s)}$	+0.34
$AgCl_{(s)} + e^- \rightarrow Ag_{(s)} + Cl^-_{(aq)}$	+0.22
$SO_4^{2-}{}_{(aq)} + 4\,H^+_{(aq)} + 2\,e^- \rightarrow SO_{2(g)} + 2\,H_2O_{(l)}$	+0.20
$Cu^{2+}_{(aq)} + e^- \rightarrow Cu^+_{(aq)}$	+0.15
$Sn^{4+}_{(aq)} + 2\,e^- \rightarrow Sn^{2+}_{(aq)}$	+0.13
$2\,H^+_{(aq)} + 2\,e^- \rightarrow H_{2(g)}$	0.00
$Pb^{2+}_{(aq)} + 2\,e^- \rightarrow Pb_{(s)}$	-0.13
$Sn^{2+}_{(aq)} + 2\,e^- \rightarrow Sn_{(s)}$	-0.14
$Ni^{2+}_{(aq)} + 2\,e^- \rightarrow Ni_{(s)}$	-0.25
$Co^{2+}_{(aq)} + 2\,e^- \rightarrow Co_{(s)}$	-0.28
$PbSO_{4(s)} + 2\,e^- \rightarrow Pb_{(s)} + SO_4^{2-}{}_{(aq)}$	-0.31
$Cd^{2+}_{(aq)} + 2\,e^- \rightarrow Cd_{(s)}$	-0.40
$Fe^{2+}_{(aq)} + 2\,e^- \rightarrow Fe_{(s)}$	-0.44
$Cr^{3+}_{(aq)} + 3\,e^- \rightarrow Cr_{(s)}$	-0.74
$Zn^{2+}_{(aq)} + 2\,e^- \rightarrow Zn_{(s)}$	-0.76
$2\,H_2O_{(l)} + 2\,e^- \rightarrow H_{2(g)} + 2\,OH^-_{(aq)}$	-0.83
$Mn^{2+}_{(aq)} + 2\,e^- \rightarrow Mn_{(s)}$	-1.18
$Al^{3+}_{(aq)} + 3\,e^- \rightarrow Al_{(s)}$	-1.66
$Be^{2+}_{(aq)} + 2\,e^- \rightarrow Be_{(s)}$	-1.85
$Mg^{2+}_{(aq)} + 2\,e^- \rightarrow Mg_{(s)}$	-2.37
$Na^+_{(aq)} + e^- \rightarrow Na_{(s)}$	-2.71
$Ca^{2+}_{(aq)} + 2\,e^- \rightarrow Ca_{(s)}$	-2.87
$Sr^{2+}_{(aq)} + 2\,e^- \rightarrow Sr_{(s)}$	-2.89
$Ba^{2+}_{(aq)} + 2\,e^- \rightarrow Ba_{(s)}$	-2.90
$K^+_{(aq)} + e^- \rightarrow K_{(s)}$	-2.93
$Li^+_{(aq)} + e^- \rightarrow Li_{(s)}$	-3.05

Fig. A.1: Standard reduction potentials at 298 K, 1 M, 1 atm

Appendix B – Measurement Techniques

Scanning Electron Microscopy

Scanning electron microscopy (SEM) is a widely used technique to analyze the shape of a substrate. It can achieve much higher resolutions compared to optical microscopes because in SEM, electrons are measured whose wave length is much smaller compared to the wavelength of visible light. Furthermore, optical microscopes have a poor depth of field (parts of the substrate that are slightly out of focus become easily blurred) because of a large aperture angle.

Because electrons are used instead of visible light, a vacuum has to be created within the SEM as electrons cannot freely move in air. Furthermore, electrons are not visible, thus special detectors have to be used. Finally because the sample is exposed to a (charged) electron beam, the material has to be sufficiently conductive to dissipate the charge.

As electron source, a tungsten filament (similar to a light bulb) is used, through which a current flows. This creates an electron cloud, which is turned into an electron beam by adding a cathode (negative charge) below it and an anode (positive charge), each with a little hole, further below. The electrons in the electron cloud are attracted by the anode but have to pass through the hole in the cathode to reach it. This creates an electron beam as shown in Fig. B.1. This “electron gun” can be controlled in intensity by changing the potential between anode and cathode.

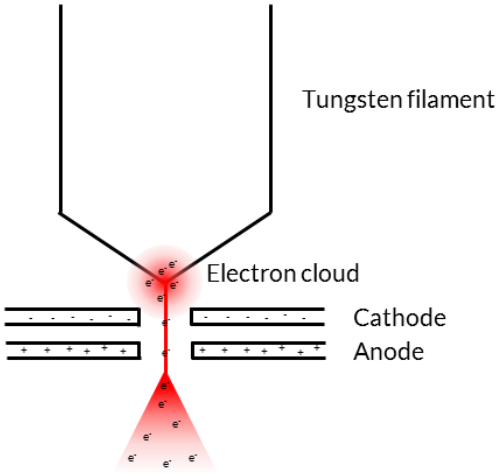

Fig. B.1: Electron gun in an SEM

To focus the emitted electrons, similar to optical microscopes, lenses are required. In an SEM, however, such a lens cannot be made of (insulating) glass, but instead electromagnetic lenses are used. These are made of coil wires around an iron core cylinder. A condenser lens is used to control the size of the beam (the larger the size, the lower the noise but the lower the resolution) and an objective lens is used to focus the beam on the sample. The scan coils are needed to diffract the beam over the sample and scan it along the magnified area.

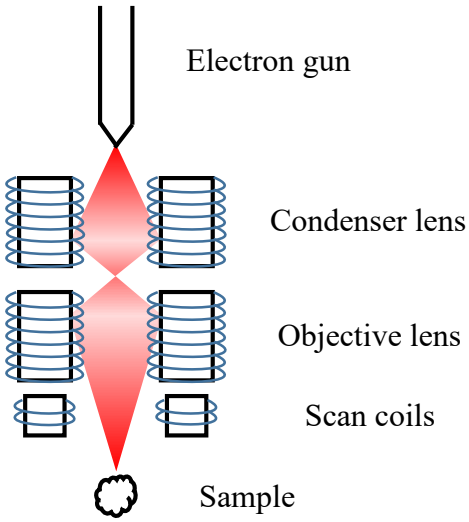

Fig. B.2: SEM column

As the electron beams then travel through the sample, three things can happen. Either, an electron beam passes through the sample, it hits an electron of the sample atom (creating secondary electrons) or it can collide with the nucleus of the sample atom, creating backscattered atoms.

When measuring the secondary electrons, the shape of the sample can be identified. As the beam scans over the sample, secondary electrons are emitted. If the electron beam reaches an elevated spot, more secondary electrons can escape the sample, corresponding to a bright spot. Analogously, if the beam hits a depression or a hole, few secondary electrons escape the sample and a dark spot is processed onto the image.

In the backscattered imaging mode, the atomic weight influences the quantity of measured electrons. A high atomic weight area of the sample will emit more backscattered electrons, making the image brighter. This observation method is thus useful when different materials are present in the sample. Clearly, also in backscattered imaging mode more electrons are measured if the beam crosses an elevated spot, wherefore the topography also affects the image in the backscattered imaging mode.

In the secondary electrons imaging mode, energy-dispersive X-ray spectroscopy (EDX) can be conducted in order to identify the elemental composition of the sample. When an incident electron hits an electron which causes it to scatter away, holes are created in the electron shells. If these holes are in the inner shells, electrons from outer shells will fill these holes which causes X-ray to emit, whose energy is equivalent to the energy difference of the electron being in the outer shell or inner shell. Higher atomic number elements have several shells, wherefore electrons in different energy states can be scattered away. Furthermore,

electrons from different shells can fill these holes, thus creating X-rays with different energies. This creates an EDX spectrum which is unique for every element. Thus, during EDX measurement, the measured EDX spectrum can be compared with standardized EDX spectra to identify and quantify the amount of different elements.

X-ray Diffraction

In order to identify the crystal structure of a solid, X-ray diffraction (XRD) is a widely used methodology because it is non-destructive, fast, and sample can be prepared easily. It is possible to identify single crystals, a mixture of different crystals and amorphous materials.

In an XRD machine, X-rays are produced by creating an electron cloud around a tungsten filament (similar as in SEM) and accelerating the electrons onto a metal target (e.g. Cupper) upon which X-rays are emitted. These X-rays hit the target at an angle θ which is changed throughout the measurement. At certain angles, the backscattered X-rays are strong in intensity, which is described by the Bragg's law:

$$n\ \lambda = 2\ d\ \sin(\theta) \qquad \text{(B.1)}$$

Whereby n is an integer, λ is the wavelength of the incident X-ray beam, d is the distance between atomic layers in the observed crystal and θ is the angle of incidence. When an X-ray hits the crystal at a certain angle, it will be scattered back at the same angle as shown in Fig. B.3. Assuming X-ray 1 is scattered back from an atom at the first plane and X-ray 2 is scattered back from an atom at the second layer, the scattered X-rays are typically out of phase and cancel each other out. If, however, Bragg's equation is true at a certain angle θ, the X-rays are in phase and a constructive interference occurs. The result is a strong intensity measured at the detector. Over an entire spectrum, typically several peaks can be measured which correspond

to the unique crystal structure of the observed sample. This pattern can then be compared to a database to identify which material and crystal structure is present.

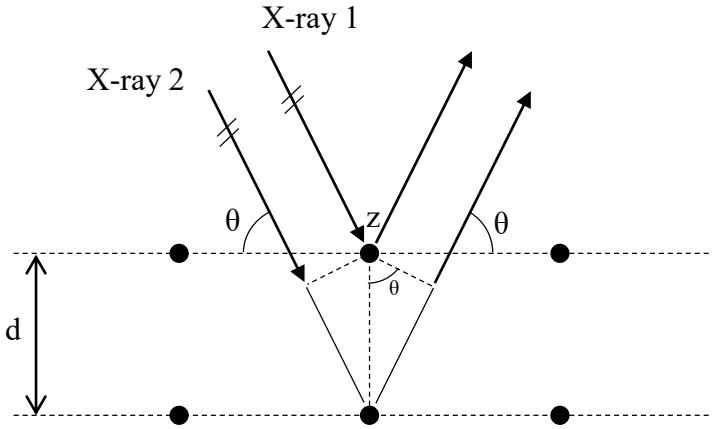

Fig. B.3: X-ray diffraction in two different crystal layers

XRD is thus a very powerful tool and crucial in this work because a big part here deals with the crystal structure of MnO_2. Whereas EDX only provides information about the presence of an element, XRD helps identify the crystal structure of the material.

Brunauer-Emmett-Teller

Brunauer-Emmett-Teller (BET) [121] theory aims to explain the physical adsorption of gas molecules on a solid surface and thus allows to identify the surface area of a material. The basic idea of BET is to measure the amount of adsorbed gas (typically nitrogen) corresponding to a monomolecular layer on the surface of the sample. These measurements are typically done at the boiling point of nitrogen (77.4 K) to minimize errors due to the vapor pressure of nitrogen. The following formula is used in order to measure the surface area:

$$\frac{1}{V_a\left(\frac{P_0}{P}-1\right)} = \frac{C-1}{V_m C}\frac{P}{P_0} + \frac{1}{V_m C}, \qquad \text{(B.2)}$$

whereby P is the partial vapor pressure of adsorbate gas in equilibrium with the surface at 77.4 K [Pa], P_0 is the saturated pressure of adsorbate gas [Pa], V_a is the volume of gas adsorbed at standard temperature and pressure [ml], V_m is the volume of gas adsorbed at standard temperature and pressure to produce an apparent monolayer on the sample surface [ml], and C is the dimensionless constant that is related to the enthalpy of adsorption of the adsorbate gas on the sample.

Appendix C – Doping

Due to the fact that the composition of the commercial materials was not known, EDX analysis was conducted in order to identify whether impurities were present. The EDX pattern of commercial λ-MnO_2 is shown in Fig. C.1. A peak referring to Mg could be observed and the ratio of Mn:Mg was identified to be ca. 20:1 on a molar basis. In case of commercial γ-MnO_2, no impurity could be identified.

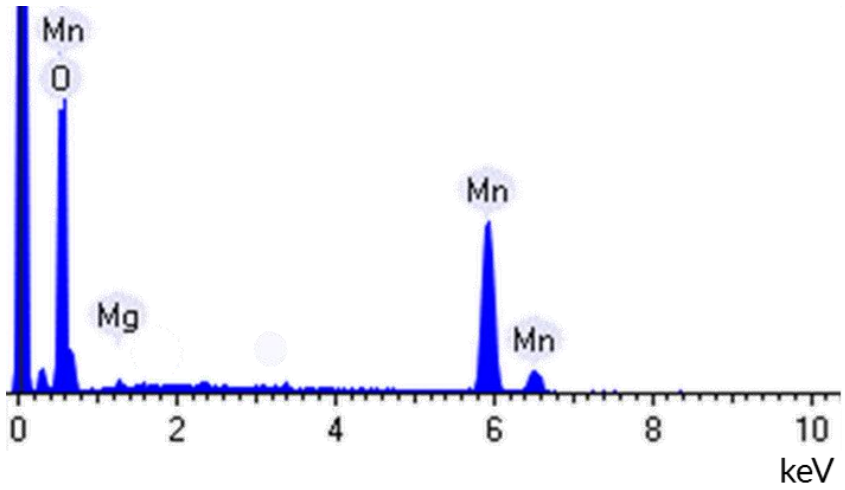

Fig. C.1: EDX pattern of commercial λ-MnO_2

In order to analyze whether Mg doping has an effect on the performance of λ-MnO_2, two samples were synthesized according to a solid state reaction. In this method, commercial γ-MnO_2 was mixed with Li nitrate (and in case of one sample with Mg nitrate) in a molar ratio of (i) Li:Mn = 1:2 and (ii) Li:Mn:Mg = 1:1.9:0.1. These mixtures were then calcined at 700°C and subsequently delithiated in order to obtain λ-MnO_2 and λ-$Mn_{1.95}Mg_{0.05}O_2$. With these samples, electrodes were fabricated and analyzed with EIS in order to obtain information about charge transfer resistance and diffusivity. The EIS spectra are shown in Fig. C.2. It was found that the charge transfer resistances were 0.607 Ω and 0.392 Ω for the Mg-free and Mg-doped

sample, respectively. This showed that doping is indeed beneficial to reduce the charge transfer resistance which affects primarily the chemical oxygen charging and ORR in FCB mode and fuel cell mode. In contrast to that, the diffusion was found to be only marginally affected by Mg doping. The Warburg pre-factor of the Mg-free and Mg-doped sample were 0.501 Ω and 0.450 Ω, respectively.

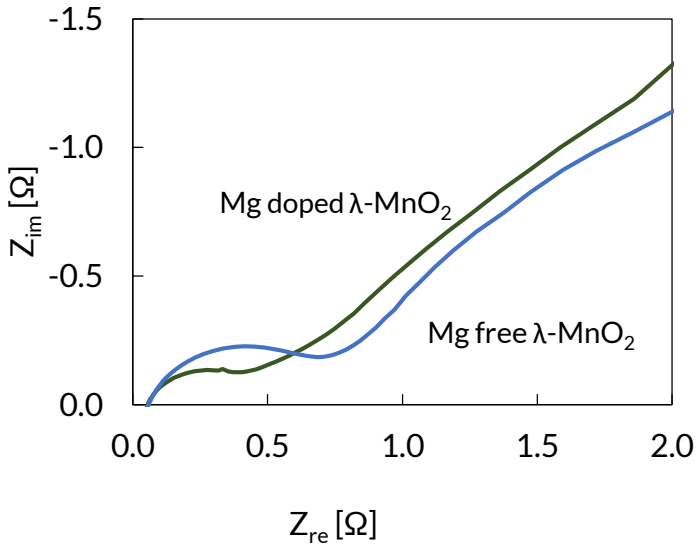

Fig. C.2: EIS spectra of Mg-doped and Mg-free λ-MnO_2

The reason why Mg doping improves the charge transfer resistance is likely due to diminishing Jahn-Teller distortion. Mg is present in the secondary oxidation state, thus increasing the oxidation state of Mn. It has been shown by other that Mg doping is an effective way to reduce Jahn-Teller distortion in lithium ion batteries [122,123] and it is likely that the same reason leads to improved results in FCB system.

Appendix D – Ag-covered nano λ-MnO_2 Charge Curves

Introduction

It was expected that silver deposition improves the catalytic capability during ORR, as silver is known to be a good catalyst in alkaline electrodes [124]. Furthermore, due to the high conductivity of silver, it was expected that silver deposition is also beneficial during electrochemical cycling because of lower ohmic losses. Thus, the effects of silver coating were first analyzed during fuel cell mode and battery mode, and then during FCB mode in order to analyze the effect of silver on the chemical charge rate. As a reference, the same material without silver deposition was used.

Experimental

The silver coated nano λ-MnO_2 was synthesized via a three step process. First, the surface of MnO_2 was activated by immersing 1 g of MnO_2 into a 6 M NaOH solution for 1h. The sensitized MnO_2 was then washed, filtered and ultrasonically suspended in 30 ml H_2O (dispersion A). Secondly, the Ag ion containing solution was prepared. In solution B, 0.16 g $AgNO_3$ (final ratio MnO_2:Ag = 10:1 wt%) was dissolved in 50 ml H_2O and then ammonia was added drop-wise until the solution turned transparent again. Thereafter, 0.15 g Polyvinylpyrrolidone (PVP) and 0.072 g sodium dodecyl sulfate (SDS) were added consecutively and the solution was stirred until the surfactants were completely dissolved. Thirdly, in solution C, 0.20 g glucose (used as reductant) was dissolved in 20 ml H_2O. Solution B was then quickly added to dispersion A and stirred for 10 min. Thereafter, solution C was added drop-wise under stirring. After 12 h, the final product was obtained by centrifuging the dispersion at 140 rpm for 3 times and drying in vacuum at 80°C over-night.

Results and discussion

Characterization

A high resolution SEM image of the Ag coated nano λ-MnO_2 is shown in Fig. D.1. The backscattered image did not show any singular bright spots which means that a well distributed deposition of silver onto nano λ-MnO_2 was achieved.

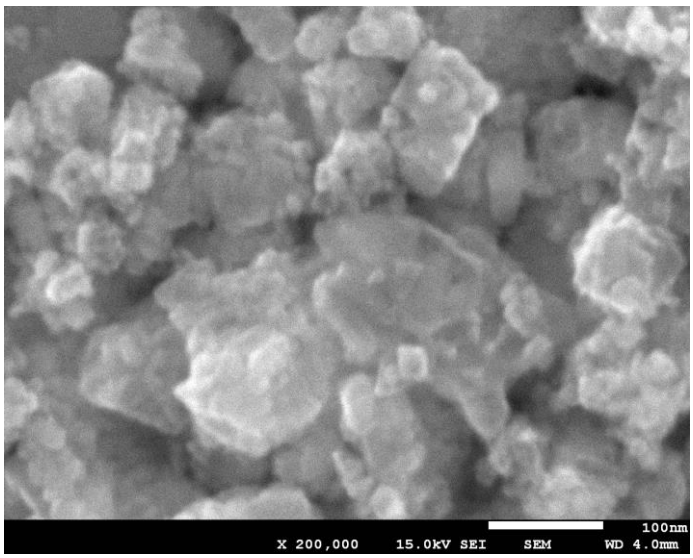

Fig. D.1: SEM image of Ag coated nano λ-MnO_2

To verify the uniform deposition, EDX measurements were conducted. The EDX map and according SEM image are shown in Fig. D.2, verifying a very uniform distribution of silver on the nano λ-MnO_2 particles.

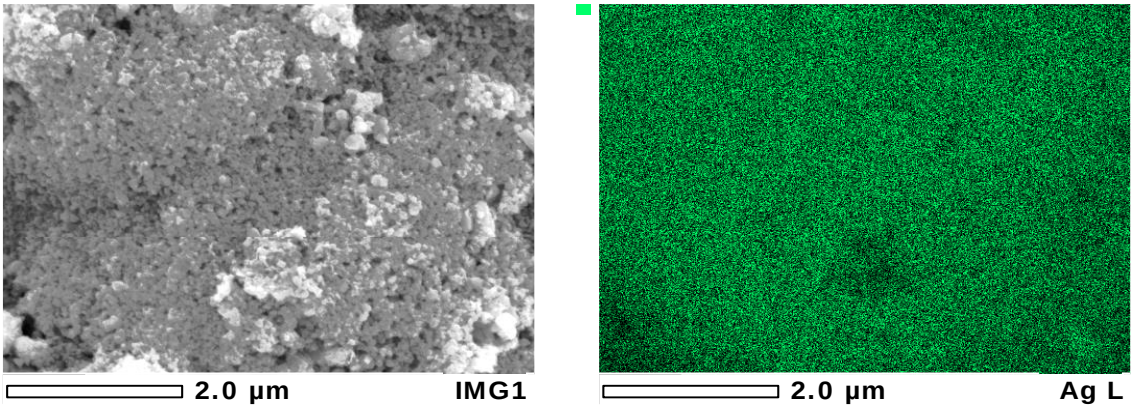

Fig. D.2: SEM and EDX images of Ag-coated nano λ-MnO_2

XRD measurements were conducted to verify the deposition of metallic silver without the presence of silver oxide. It can be seen in Fig. D.3 that only peaks belonging to metallic silver and λ-MnO_2 were measured, thus confirming that the here introduced synthesis method led to the aspired material.

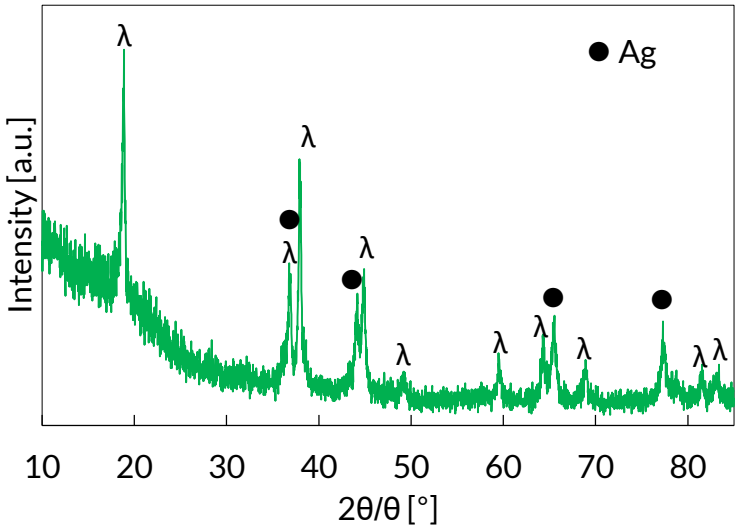

Fig. D.3: XRD pattern of Ag-coated nano λ-MnO_2

To achieve a uniform silver deposition onto MnO_2, several parameters were found to be crucial. In Fig. D.4 and Fig. D.5, two examples are shown where the silver deposition was not optimized. In Fig. D.4 the ratio of silver to MnO_2 was 1:5 (wt. %), which caused a spontaneous

formation of silver nanoparticles in the solution, which led to comparatively large particles. In Fig. D.5, the amount of surfactants was too high, which led to the formation of only few, but large chunks of silver.

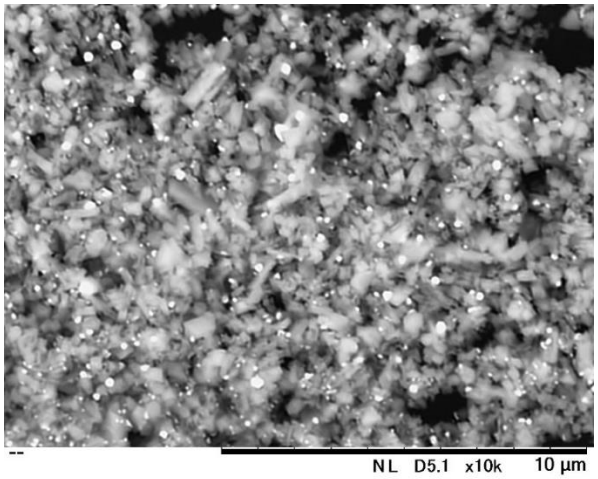

Fig. D.4: SEM image of silver nanoparticles and MnO_2

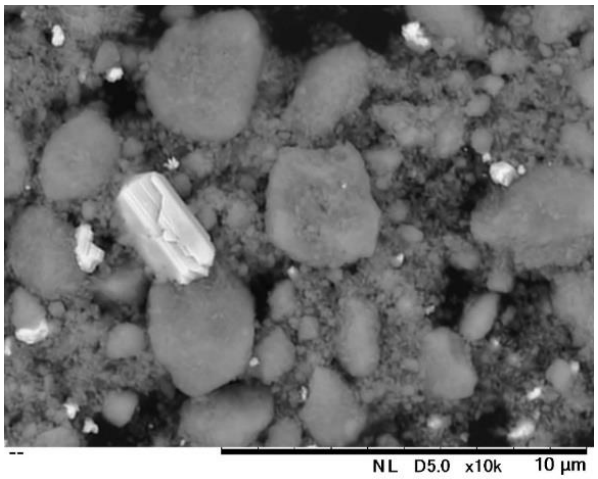

Fig. D.5: SEM image of conglomerated silver nanoparticles and MnO_2

Oxygen reduction reaction

The ORR rate of both the Ag-covered and Ag-free nano λ-MnO_2 were measured according to previous chapters. In Fig. D.6 the I-V curves of both materials are shown. The open circuit voltage was found to be 0.15 V vs. Hg/HgO and 0.09 V vs. Hg/HgO for the Ag-covered and Ag-free nano λ-MnO_2, respectively. Due to a higher activation polarization loss in the Ag-

covered nano λ-MnO_2, the voltage was similar among the two samples at low current densities. However, as the current density increased, it was found that the ohmic losses are considerably smaller in the Ag-covered nano λ-MnO_2 than the Ag-free nano λ-MnO_2. This resulted in a much higher current density of the Ag-covered nano λ-MnO_2, which reached a potential of -0.147 V vs. Hg/HgO at a current density of 140 mA/cm^2. This is the equivalent of an electrochemical discharge rate of 5 C.

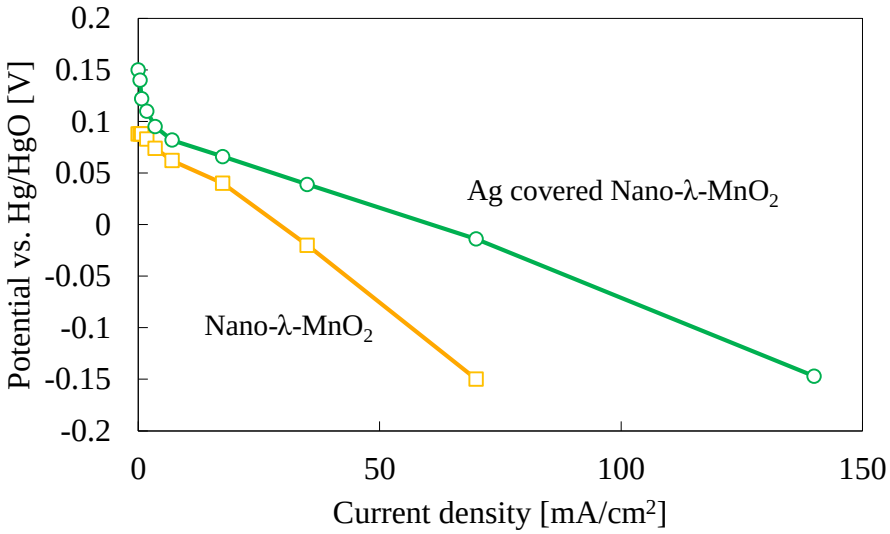

Fig. D.6: ORR of Ag-coated and Ag-free nano λ-MnO_2

This result shows that silver coating was indeed beneficial for the ORR rate of the positive electrode in FCB systems. This may primarily be due to the high activity of silver towards oxygen reduction in alkaline electrolytes. In addition, the improved conductivity likely played a beneficial role. Silver has a resisitivity of $1.59 \cdot 10^{-6}$ Ω cm [125], which is several orders of magnitude lower than that of MnO_2 (0.1 Ω cm [126,127]). It is thus probable that silver coating helps improve the electric conductivity of the electrode, resulting in a faster ORR.

Electrochemical cycling

An improved electric conductivity was expected to also led to better performance during electrochemical redox cycling. The Ag-covered nano λ-MnO_2 was thus tested under battery mode at different C-rates and compared with its Ag-free equivalent. Both electrodes were charged at 0.2 C without a charge cut-off voltage to 100% of the theoretical capacity during all cycles. The discharge C-rate was varied according to previous chapters and for every discharge a cut-off voltage of -0.4 V vs. Hg/HgO was used. The discharge capacities at different C-rates is shown in Fig. D.7.

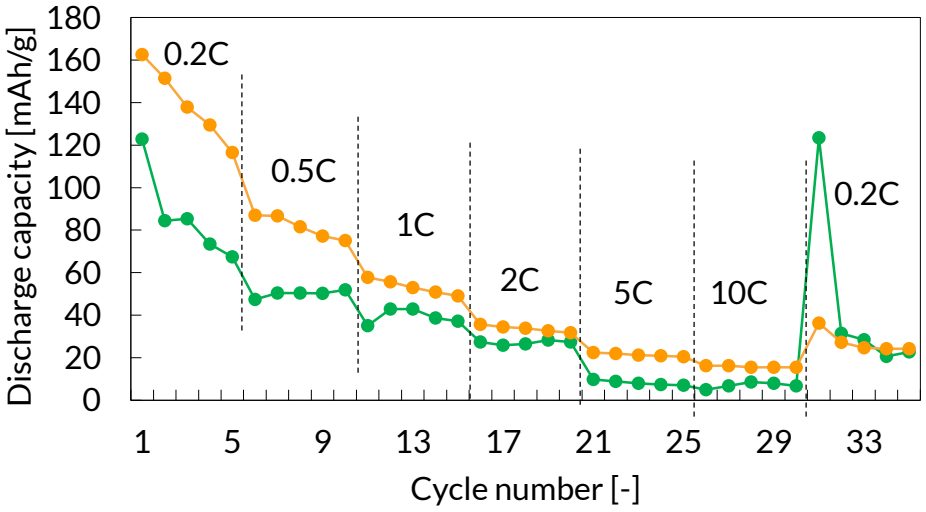

Fig. D.7: Discharge capacities of the Ag-free and Ag-covered nano λ-MnO_2 electrodes.

The discharge capacity of Ag-covered nano λ-MnO_2 was found to fluctuate considerably, even at the same discharge rate. Typically, its discharge capacity was lower than that of the Ag-free equivalent, but at the 5th cycle at 2 C discharge, the capacity was almost the same, and at the 31st cycle (the first cycle at 0.2 C after the 10.0 C discharge) the capacity was even much higher in the Ag-covered sample.

To identify the source of this behavior, the charge curves were analyzed more closely. The charge curves of both the Ag-free and Ag-covered nano λ-MnO_2 are shown in Fig. D.8.

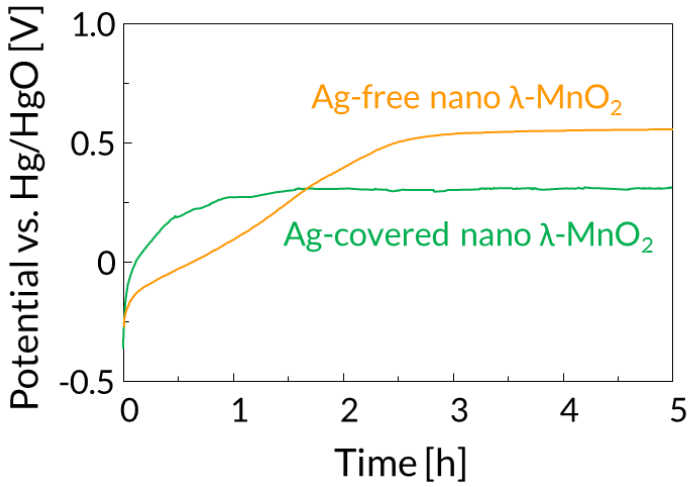

Fig. D.8: Charge curves of Ag-free and Ag-covered nano λ-MnO_2 electrodes during the 5th cycle at 0.2 C

The charge curves show that a high over-potential was present in the Ag-free nano λ-MnO_2 and that the voltage stayed constant throughout most of the step at ca 0.55 V vs. Hg/HgO. This is very close to the oxygen evolution potential in alkaline environment (see Appendix A). The Ag-covered nano λ-MnO_2 on the other hand reached a maximum voltage of only 0.30 V vs. Hg/HgO. Furthermore, the charge curve was found to become noisy after ca. 20 min of charging. At this voltage, it is not possible to evolve oxygen, wherefore it is suggested that an alternative reaction occurs. A possible reaction is the oxidation of silver, as it also occurs in silver-zinc batteries. This reaction occurs in two steps [128]:

$$2\,Ag_s + 2\,OH^- \rightarrow Ag_2O + H_2O + 2\,e^- \qquad (D.1)$$

$$Ag_2O + 2\,OH^- \rightarrow 2\,AgO + H_2O + 2\,e^- \qquad (D.2)$$

The standard reduction potential of these reactions are 0.604 V and 0.342 V, respectively [129]. Reaction 5.7 is thus below the oxidation potential of oxygen in alkaline, which allows

for oxidation of Ag_2O before oxygen evolution reaction. This reaction may inhibit a complete charge of MnO_2 and could therefore explain the low discharge capacity. Thus, the lower capacity of Ag-covered nano λ-MnO_2 is likely due to incomplete charge, not because of degradation of MnO_2. This is supported by the high discharge capacity of the 31st cycle. It is likely that during cycling at high C-rates of up to 10.0 C, not the entire particle was discharged due to proton diffusion limitations and the charged capacity thus steadily increased during those cycles. In the subsequent first discharge at a low C-rate (0.2 C), the particles could be completely discharged, resulting in a very high discharge capacity. The discharge capacity returned to low levels in the subsequent cycles due to an incomplete charge.

The first five charge cycles of the Ag-covered nano λ-MnO_2 are shown in Fig. D.9. The charge rate becomes noisy at an arbitrary state of charge and the sooner it occurs, the lower the following discharge capacity. For example, it was found that the second charge curve reached the lowest potential and the subsequent discharge capacity was lower than the cycle before and after.

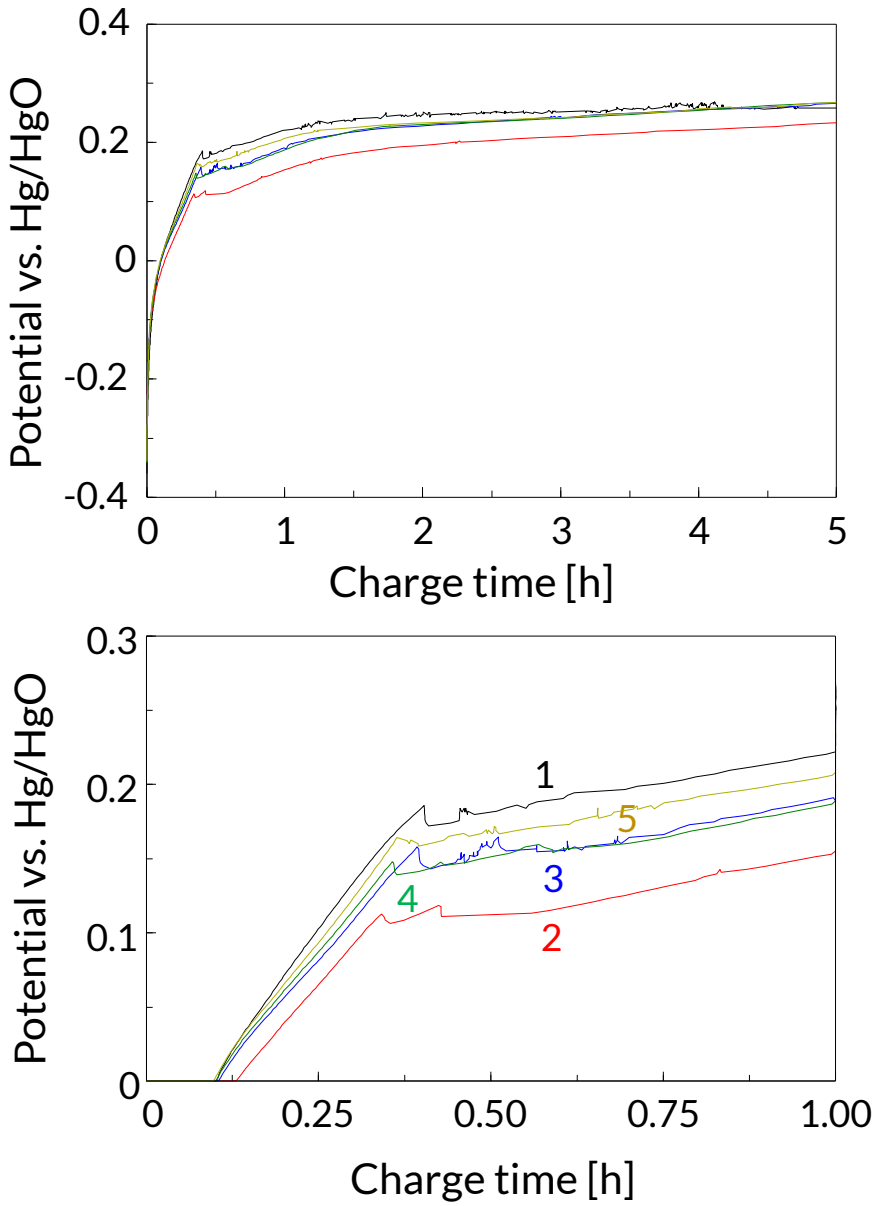

Fig. D.9: Charge curves of Ag-covered λ-MnO_2 highlighting the point at which oxygen evolution starts

Chemical charging with oxygen

Lastly, the Ag-covered nano λ-MnO_2 was also tested under FCB mode according to the equal protocol as the Ag-free nano λ-MnO_2 sample. The resulting discharge curves are shown in Fig. D.10.

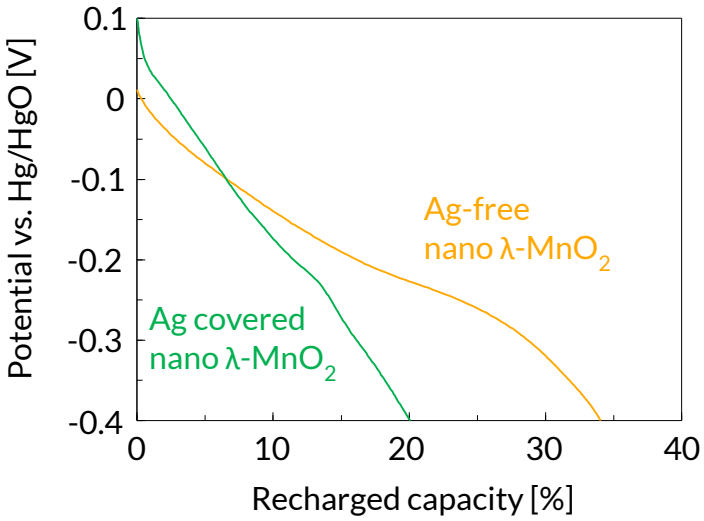

Fig. D.10: Discharge curves (0.1 C) of Ag-free and Ag-covered nano λ-MnO_2 electrodes after chemical oxygen charging

The chemically charged capacity of the Ag-covered sample was considerably smaller than that of the Ag-free sample. Although the initial potential was higher, which may be due to remaining oxygen in the electrolyte which allowed for an ORR over silver, the potential dropped fairly linearly in the Ag-covered nano λ-MnO_2 and only a slight shoulder was observed. The chemical charge rate of the Ag-covered nano λ-MnO_2 is thus slower than for the pristine λ-MnO_2.

The reason for this lower chemical oxygen charge rate is suggested to be due to a smaller availability of active surface sights. Because the silver was deposited on the surface of MnO_2, less sites were available where oxygen could adsorb onto the MnO_2 surface. This resulted in a slower surface oxidation, which is particularly crucial at the beginning of the chemical oxygen charging step, as discussed in Chapter 3.

In the second part, a facile method to synthesize an Ag/MnO_2 compound for the application in FCB system was introduced. Silver was added onto nano λ-MnO_2 in a scalable method. The capabilities as a positive electrode in an FCB were assessed during fuel cell mode, battery mode

and FCB mode. It was shown that the addition of silver improves the oxygen reduction capability of the electrode which was likely due to the high ORR capability and electric conductivity of silver. However, silver caused a side reaction during charging, which was disadvantageous during electrochemical cycling because it resulted in incomplete charge. Furthermore, addition of silver decreased the availability of active surface sites where chemical charge could occur, thus decreasing the chemical oxygen charge rate.

Appendix E – Synthesis of MnO_2 covered carbon nanofibers

MnO_2 covered carbon nano fibers (CNF) were synthesized as follows. First, a CNF mat was fabricated by electrospinning a 12% polyacrylonitrile (PAN) solution in N,N-dimethylformamide (DMF) at 30 kV. The PAN fibers were then transformed into carbon by first stabilizing in 280°C in air and then carbonizing at 1100°C in a O_2 free atmosphere. MnO_2 was then deposited onto the CNF mat via electrochemical plating according to the fibrous electrode in Chapter 5. The resulting electrode is shown in Fig. E.1. Subsequent transformation into λ-MnO_2 unfortunately disintegrated the compound, wherefore other synthesis methods have to be found to obtain a λ-MnO_2/CNF electrode.

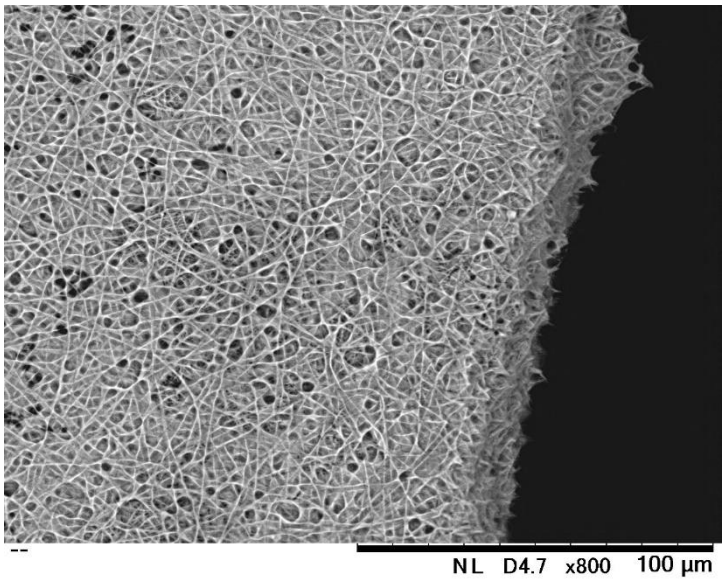

Fig. E.1: MnO_2 covered CNF

Bibliography

[1] Dincer I. Renewable energy and sustainable development: a crucial review. Renew Sustain Energy Rev 2000;4:157–75. doi:10.1016/S1364-0321(99)00011-8.

[2] Ousterhout DG. California Public Utilities Commission Adopts Energy Storage Procurement Targets 2013. https://www.reedsmith.com/California-Public-Utilities-Commission-Adopts-Energy-Storage-Procurement-Targets-10-23-2013/ (accessed April 29, 2016).

[3] Die Energiewende (in German) n.d. http://www.energieverbraucher.de/de/energiewende__1900/ (accessed May 2, 2016).

[4] Waters R. Tesla targets mass market with new Model 3. Financ Times 2016. http://www.ft.com/cms/s/0/8913fdc2-f7c3-11e5-803c-d27c7117d132.html#axzz47AjjtYOo (accessed April 29, 2016).

[5] Inagaki K. Toyota: Emission control. Financ Times 2016. http://www.ft.com/intl/cms/s/2/a7ad7876-d0ef-11e5-831d-09f7778e7377.html#axzz47AjjtYOo (accessed April 29, 2016).

[6] Denholm P, Ela E, Kirby B, Milligan M. The Role of Energy Storage with Renewable Electricity Generation 2010:1–61.

[7] Ragone D V. Review of Battery Systems for Electrically Powered Vehicles. 1968. doi:10.4271/680453.

[8] Gao W. Performance Comparison of a Fuel Cell-Battery Hybrid Powertrain and a Fuel Cell-Ultracapacitor Hybrid Powertrain. IEEE Trans Veh Technol 2005;54:846–55.

[9] Bauman J, Kazerani M. A Comparative Study of Fuel-Cell – Battery , Fuel-Cell – Battery – Ultracapacitor Vehicles. IEEE Trans Veh Technol 2008;57:760–9.

[10] Han J, Park E-S. Direct methanol fuel-cell combined with a small back-up battery. J Power Sources 2002;112:477–83. doi:10.1016/S0378-7753(02)00441-X.

[11] Choi B, Lee S, Fushimi C, Tsutsumi A. Development of NiMH-based Fuel Cell/Battery (FCB) system: Characterization of Ni(OH)2/MnO2 positive electrode for FCB. J Power Sources 2009;194:1150–5. doi:10.1016/j.jpowsour.2009.06.039.

[12] Buchmann I. Battery University. Http://www.batteryuniversity.com/ 2014. http://batteryuniversity.com/learn/article/whats_the_best_battery (accessed April 15, 2016).

[13] Erjavec J. Battery Basics. Hybrid, Electr. Fuel-Cell Veh., 2013, p. 57–84.

[14] Iwakura C, Nohara S, Furukawa N, Inoue H. The possible use of polymer gel electrolytes in nickel/metal hydride battery. Solid State Ionics 2002;148:487–92. doi:10.1016/S0167-2738(02)00092-9.

[15] Evans M. UC Davis ChemWiki 2015. http://chemwiki.ucdavis.edu/Core/Analytical_Chemistry/Electrochemistry/Case_Studies/Case_Study:_Fuel_Cells (accessed April 15, 2016).

[16] Yeager E. Dioxygen electrocatalysis: mechanisms in relation to catalyst structure. J Mol Catal 1986;38:5–25. doi:10.1016/0304-5102(86)87045-6.

[17] Wu J, Zhang D, Wang Y, Wan Y. Manganese oxide–graphene composite as an efficient catalyst for 4-electron reduction of oxygen in alkaline media. Electrochim Acta 2012;75:305–10. doi:10.1016/j.electacta.2012.05.005.

[18] Atkins P, de Paula J. Physical Chemistry. 9th ed. Oxford: Oxford University Press; 2009. doi:10.1039/c1cs15191f.

[19] Lee S, Choi B, Hamasuna N, Fushimi C, Tsutsumi A. Characterization of MnO2 positive electrode for Fuel Cell/Battery (FCB). J Power Sources 2008;181:177–81. doi:10.1016/j.jpowsour.2008.02.083.

[20] Choi B, Lee S, Fushimi C, Tsutsumi A. Power generation/energy storage by a fuel cell/battery system: Regeneration of the MnO2 positive electrode with gaseous oxygen. Electrochim Acta 2010;55:8771–8. doi:10.1016/j.electacta.2010.07.090.

[21] Choi B, Lee S, Fushimi C, Tsutsumi A. Fibrous MnO2 electrode electrodeposited on carbon fiber for a fuel cell/battery system. Electrochim Acta 2011;56:6696–701. doi:10.1016/j.electacta.2011.05.057.

[22] Choi B, Lee S, Kawai H, Fushimi C, Tsutsumi A. Rapid hydrogen charging on metal hydride negative electrode of Fuel Cell/Battery (FCB) systems. Int J Hydrogen Energy 2009;34:2058–61. doi:10.1016/j.ijhydene.2008.12.032.

[23] Choi B, Panthi D, Kwon Y, Tsutsumi A. Chemical Charging on a MnO2 Electrode of a Fuel Cell/Battery System in a Highly O2-Dissolved Electrolyte. Electrochim Acta 2015;160:323–9. doi:10.1016/j.electacta.2015.02.023.

[24] Toupin M, Brousse T, Bélanger D. Charge Storage Mechanism of MnO2 Electrode Used in Aqueous Electrochemical Capacitor. Chem Mater 2004;16:3184–90. doi:10.1021/cm049649j.

[25] Chang J-K, Tsai W-T. Material Characterization and Electrochemical Performance of Hydrous Manganese Oxide Electrodes for Use in Electrochemical Pseudocapacitors. J Electrochem Soc 2003;150:A1333. doi:10.1149/1.1605744.

[26] Yang P, Ding Y, Lin Z, Chen Z, Li Y, Qiang P, et al. Low-cost high-performance solid-state asymmetric supercapacitors based on MnO2 nanowires and Fe2O3 nanotubes. Nano Lett 2014;14:731–6. doi:10.1021/nl404008e.

[27] Jaffe R, Price J, Hitzman M, Slakey F. Energy Critical Elements. Forum Phys Soc 2011. https://www.aps.org/units/fps/newsletters/201107/jaffe.cfm (accessed January 29, 2016).

[28] Devaraj S, Munichandraiah N. Effect of Crystallographic Structure of MnO 2 on Its Electrochemical Capacitance Properties. J Phys Chem C 2008;112:4406–17.

doi:10.1021/jp7108785.

[29] Brock SL, Duan N, Tian ZR, Giraldo O, Zhou H, Suib SL. A Review of Porous Manganese Oxide Materials. Chem Mater 1998;10:2619–28. doi:10.1021/cm980227h.

[30] Baur WH. Rutile-type compounds. V. Refinement of MnO2 and MgF2. Acta Crystallogr Sect B Struct Crystallogr Cryst Chem 1976;32:2200–4. doi:10.1107/S0567740876007371.

[31] Ma R, Bando Y, Zhang L, Sasaki T. Layered MnO2 Nanobelts: Hydrothermal Synthesis and Electrochemical Measurements. Adv Mater 2004;16:918–22. doi:10.1002/adma.200306592.

[32] Brousse T, Toupin M, Dugas R, Athouël L, Crosnier O, Bélanger D. Crystalline MnO2 as Possible Alternatives to Amorphous Compounds in Electrochemical Supercapacitors. J Electrochem Soc 2006;153:A2171. doi:10.1149/1.2352197.

[33] Ghodbane O, Pascal J-LL, Favier FF. Microstructural effects on charge-storage properties in MnO2-based electrochemical supercapacitors. ACS Appl Mater Interfaces 2009;1:1130–9. doi:10.1021/am900094e.

[34] Subramanian V, Zhu H, Vajtai R, Ajayan PM, Wei B. Hydrothermal synthesis and pseudocapacitance properties of MnO2 nanostructures. J Phys Chem B 2005;109:20207–14. doi:10.1021/jp0543330.

[35] Wei W, Cui X, Chen W, Ivey DG. Manganese oxide-based materials as electrochemical supercapacitor electrodes. Chem Soc Rev 2011;40:1697–721. doi:10.1039/c0cs00127a.

[36] Li B, Rong G, Xie Y, Huang L, Feng C. Low-temperature synthesis of alpha-MnO2 hollow urchins and their application in rechargeable Li+ batteries. Inorg Chem 2006;45:6404–10. doi:10.1021/ic0606274.

[37] Jiao F, Bruce PG. Mesoporous Crystalline β-MnO2—a Reversible Positive Electrode for Rechargeable Lithium Batteries. Adv Mater 2007;19:657–60. doi:10.1002/adma.200602499.

[38] Wu C, Xie Y, Wang D, Yang J, Li T. Selected-Control Hydrothermal Synthesis of γ-MnO2 3D Nanostructures. J Phys Chem B 2003;107:13583–7. doi:10.1021/jp035567r.

[39] Kim SH, Kim SJ, Oh SM. Preparation of Layered MnO2 via Thermal Decomposition of KMnO 4 and Its Electrochemical Characterizations. Chem Mater 1999;11:557–63. doi:10.1021/cm9801643.

[40] Kim DK, Muralidharan P, Lee H-W, Ruffo R, Yang Y, Chan CK, et al. Spinel LiMn2O4 Nanorods as Lithium Ion Battery Cathodes. Nano Lett 2008;8:3948–52. doi:10.1021/nl8024328.

[41] Era A, Takehara Z, Yoshizawa S. Discharge mechanism of the manganese dioxide electrode. Electrochim Acta 1967;12:1199–212. doi:10.1016/0013-4686(67)80035-5.

[42] Tang N, Tian X, Yang C, Pi Z, Han Q. Facile synthesis of α-MnO2 nanorods for high-performance alkaline batteries. J Phys Chem Solids 2010;71:258–62.

doi:10.1016/j.jpcs.2009.11.016.

[43] Huang Y, Lin Y, Li W. Controllable syntheses of α- and δ-MnO2 as cathode catalysts for zinc-air battery. Electrochim Acta 2013;99:161–5. doi:10.1016/j.electacta.2013.03.088.

[44] Cheng F, Su Y, Liang J, Tao Z, Chen J. MnO 2 -Based Nanostructures as Catalysts for Electrochemical Oxygen Reduction in Alkaline Media †. Chem Mater 2010;22:898–905. doi:10.1021/cm901698s.

[45] Kalubarme RS, Cho M-S, Yun K-S, Kim T-S, Park C-J. Catalytic characteristics of MnO2 nanostructures for the O2 reduction process. Nanotechnology 2011;22:395402. doi:10.1088/0957-4484/22/39/395402.

[46] Hunter JC. Preparation of a new crystal form of manganese dioxide: λ-MnO2. J Solid State Chem 1981;39:142–7. doi:10.1016/0022-4596(81)90323-6.

[47] Greedan JE, Raju NP, Wills AS, Morin C, Shaw SM, Reimers JN. Structure and Magnetism in λ-MnO2. Geometric Frustration in a Defect Spinel. Chem Mater 1998;10:3058–67. doi:10.1021/cm9801789.

[48] Gummow RJ, de Kock A, Thackeray MM. Improved capacity retention in rechargeable 4 V lithium/lithium-manganese oxide (spinel) cells. Solid State Ionics 1994;69:59–67. doi:10.1016/0167-2738(94)90450-2.

[49] Hosono E, Kudo T, Honma I, Matsuda H, Zhou H. Synthesis of single crystalline spinel LiMn2O4 nanowires for a lithium ion battery with high power density. Nano Lett 2009;9:1045–51. doi:10.1021/nl803394v.

[50] Thackeray MM. Spinel Electrodes for Lithium Batteries. J Am Ceram Soc 2004;82:3347–54. doi:10.1111/j.1151-2916.1999.tb02250.x.

[51] Mondoloni C, Lborde M, Rioux J, Andoni E, Levy-Clement C. Rechargeable Alkaline Manganese Dioxide Batteries. J Electrochem Soc 1992;139:954. doi:10.1149/1.2069374.

[52] Xia X, Guo Z. Studies on a Novel Secondary Battery: MH/MnO2 Rechargeable Battery. Characteristics of the MnO2 cathode. J Electrochem Soc 1997;144:L213–6.

[53] Qu D. The feasibility of using a rechargeable MnO2 cathode with a metal hydride anode. J Appl Electrochem 1999;29:511–20.

[54] Xiao W, Wang D, Lou XW. Shape-Controlled Synthesis of MnO 2 Nanostructures with Enhanced Electrocatalytic Activity for Oxygen Reduction. J Phys Chem C 2010;114:1694–700. doi:10.1021/jp909386d.

[55] Schweigart HELG. Cathodic Reduction Mechanisms of Manganese Dioxide from Derivative Discharge Curves. J Electrochem Soc 1976;123:1123. doi:10.1149/1.2133020.

[56] McBreen J. The electrochemistry of β-MnO2 and γ-MnO2 in alkaline electrolyte. Electrochim Acta 1975;20:221–5. doi:10.1016/0013-4686(75)85028-6.

[57] Ambrose J, Briggs GWD. The manganous hydroxide electrode. Electrochim Acta 1971;16:111–9. doi:10.1016/0013-4686(71)85132-0.

[58] Donne SW. Redox Processes at the Manganese Dioxide Electrode. J Electrochem Soc 1997;144:2961. doi:10.1149/1.1837944.

[59] Donne SW. Redox Processes at the Manganese Dioxide Electrode. J Electrochem Soc 1997;144:2954. doi:10.1149/1.1837943.

[60] Donne SW. Redox Processes at the Manganese Dioxide Electrode. J Electrochem Soc 1997;144:2949. doi:10.1149/1.1837942.

[61] Im D, Manthiram A, Coffey B. Manganese(III) Chemistry in KOH Solutions in the Presence of Bi- or Ba-Containing Compounds and Its Implications on the Rechargeability of γ-MnO2 in Alkaline Cells. J Electrochem Soc 2003;150:A1651. doi:10.1149/1.1622960.

[62] Cao YL, Yang HX, Ai XP, Xiao LF. The mechanism of oxygen reduction on MnO2-catalyzed air cathode in alkaline solution. J Electroanal Chem 2003;557:127–34. doi:10.1016/S0022-0728(03)00355-3.

[63] Meng Y, Song W, Huang H, Ren Z, Chen S-Y, Suib SL. Structure-property relationship of bifunctional MnO2 nanostructures: highly efficient, ultra-stable electrochemical water oxidation and oxygen reduction reaction catalysts identified in alkaline media. J Am Chem Soc 2014;136:11452–64. doi:10.1021/ja505186m.

[64] Ohsaka T, Mao L, Arihara K, Sotomura T. Bifunctional catalytic activity of manganese oxide toward O2 reduction: novel insight into the mechanism of alkaline air electrode. Electrochem Commun 2004;6:273–7. doi:10.1016/j.elecom.2004.01.007.

[65] Mao L. Mechanistic study of the reduction of oxygen in air electrode with manganese oxides as electrocatalysts. Electrochim Acta 2003;48:1015–21. doi:10.1016/S0013-4686(02)00815-0.

[66] Lima FHB, Calegaro ML, Ticianelli EA. Investigations of the catalytic properties of manganese oxides for the oxygen reduction reaction in alkaline media. J Electroanal Chem 2006;590:152–60. doi:10.1016/j.jelechem.2006.02.029.

[67] Zhang X, Li B, Liu C, Chu Q, Liu F, Wang X, et al. Rapid microwave-assisted hydrothermal synthesis of morphology-tuned MnO2 nanocrystals and their electrocatalytic activities for oxygen reduction. Mater Res Bull 2013;48:2696–701. doi:10.1016/j.materresbull.2013.03.025.

[68] Cheng F, Zhao J, Song W, Li C, Ma H, Chen J, et al. Facile controlled synthesis of MnO2 nanostructures of novel shapes and their application in batteries. Inorg Chem 2006;45:2038–44. doi:10.1021/ic051715b.

[69] Stoerzinger KA, Risch M, Han B, Shao-Horn Y. Recent Insights into Manganese Oxides in Catalyzing Oxygen Reduction Kinetics. ACS Catal 2015;5:6021–31. doi:10.1021/acscatal.5b01444.

[70] Cockayne E, Li L. First-Principles Studies of the Atomic, Electronic, and Magnetic

Structure of α-MnO2 (Cryptomelane) n.d.

[71] Bolzan A, Fong C, Kennedy B, Howard C. Powder Neutron Diffraction Study of Pyrolusite, β-MnO2. Aust J Chem 1993;46:939. doi:10.1071/CH9930939.

[72] Fong C, Kennedy BJ, Elcombe MM. A powder neutron diffraction study of λ and γ manganese dioxide and of LiMn2O4. Zeitschrift Für Krist - Cryst Mater 1994;209. doi:10.1524/zkri.1994.209.12.941.

[73] Mishra S, Ceder G. Structural stability of lithium manganese oxides. Phys Rev B 1999;59:6120–30. doi:10.1103/PhysRevB.59.6120.

[74] Kanamura K, Naito H, Yao T, Takehara Z. Structural change of the LiMn2O4 spinel structure induced by extraction of lithium. J Mater Chem 1996;6:33. doi:10.1039/jm9960600033.

[75] Zhang X, Yang W, Yang J, Evans DG. Synthesis and characterization of α-MnO2 nanowires: Self-assembly and phase transformation to β-MnO2 microcrystals. J Cryst Growth 2008;310:716–22. doi:10.1016/j.jcrysgro.2007.11.113.

[76] Huang X, Lv D, Yue H, Attia A, Yang Y. Controllable synthesis of α- and β-MnO2: cationic effect on hydrothermal crystallization. Nanotechnology 2008;19:225606. doi:10.1088/0957-4484/19/22/225606.

[77] Portehault D, Cassaignon S, Baudrin E, Jolivet J-P. Structural and morphological control of manganese oxide nanoparticles upon soft aqueous precipitation through MnO4−/Mn2+ reaction. J Mater Chem 2009;19:2407. doi:10.1039/b816348k.

[78] Shen X-F, Ding Y-S, Liu J, Cai J, Laubernds K, Zerger RP, et al. Control of Nanometer-Scale Tunnel Sizes of Porous Manganese Oxide Octahedral Molecular Sieve Nanomaterials. Adv Mater 2005;17:805–9. doi:10.1002/adma.200401225.

[79] Shannon RD. Revised effective ionic radii and systematic studies of interatomic distances in halides and chalcogenides. Acta Crystallogr Sect A 1976;32:751–67. doi:10.1107/S0567739476001551.

[80] Hill LI, Arrivé H, Guyomard D. Effect of synthesis conditions on the morphology of MnO2 (α-, β-, γ-) synthesized by the hydrothermal-electrochemical method. Ionics (Kiel) 2002;8:161–71. doi:10.1007/BF02376064.

[81] Sing IB, Park S-M. Synthesis of β-MnO2 nanowires and their electrochemical capacitive behavior. Indian J Chem 2015;54A:46–51.

[82] Misnon II, Aziz RA, Zain NKM, Vidhyadharan B, Krishnan SG, Jose R. High performance MnO2 nanoflower electrode and the relationship between solvated ion size and specific capacitance in highly conductive electrolytes. Mater Res Bull 2014;57:221–30. doi:10.1016/j.materresbull.2014.05.044.

[83] Wang X, Li Y. Selected-Control Hydrothermal Synthesis of α- and β-MnO2 Single Crystal Nanowires. J Am Chem Soc 2002;124:2880–1. doi:10.1021/ja0177105.

[84] Chen K, Dong Noh Y, Li K, Komarneni S, Xue D. Microwave–Hydrothermal

Crystallization of Polymorphic MnO2 for Electrochemical Energy Storage. J Phys Chem C 2013;117:10770–9. doi:10.1021/jp4018025.

[85] Chen S, Zhu J, Han Q, Zheng Z, Yang Y, Wang X. Shape-Controlled Synthesis of One-Dimensional MnO 2 via a Facile Quick-Precipitation Procedure and its Electrochemical Properties. Cryst Growth Des 2009;9:4356–61. doi:10.1021/cg900223f.

[86] Kozawa A, Yeager JF. The Cathodic Reduction Mechanism of Electrolytic Manganese Dioxide in Alkaline Electrolyte. J Electrochem Soc 1965;112:959. doi:10.1149/1.2423350.

[87] Ghaemi M, Khosravi-Fard L, Neshati J. Improved performance of rechargeable alkaline batteries via surfactant-mediated electrosynthesis of MnO2. J Power Sources 2005;141:340–50. doi:10.1016/j.jpowsour.2004.10.004.

[88] Llompart S, Ouboumour H, Yu LT, Mas JC, Mendiboure A, Vignaud R. Oxygen-Regeneration of Discharged Manganese Dioxide Electrode I. General Phenomena Observed on Thick Powder Electrodes. J Electrochem Soc 1991;138:665–9. doi:10.1149/1.2086448.

[89] Scott W. Donne, Swinkels DAJ. Redox Processes at the Manganese Dioxide Electrode III . Detection of Soluble and Solid Intermediates during Reduction. J Electrochem Soc 1997;144:2961–7.

[90] Lima FHB, Calegaro ML, Ticianelli E a. Electrocatalytic activity of manganese oxides prepared by thermal decomposition for oxygen reduction. Electrochim Acta 2007;52:3732–8. doi:10.1016/j.electacta.2006.10.047.

[91] Kanungo SB, Parida KM, Sant BR. Studies on MnO2—III. The kinetics and the mechanism for the catalytic decomposition of H2O2 over different crystalline modifications of MnO2. Electrochim Acta 1981;26:1157–67. doi:10.1016/0013-4686(81)85093-1.

[92] Cussler EL. Diffusion Mass Transfer in Fluid Systems. Cambridge University Press; 1997.

[93] Browning GJ, Donne SW. Proton diffusion in γ-manganese dioxide. J Appl Electrochem 2005;35:871–8. doi:10.1007/s10800-005-4738-1.

[94] Qu D. The ac impedance studies for porous MnO2 cathode by means of modified transmission line model. J Power Sources 2001;102:270–6. doi:10.1016/S0378-7753(01)00810-2.

[95] Van Vleck JH. Theory of the Variations in Paramagnetic Anisotropy Among Different Salts of the Iron Group. Phys Rev 1932;41:208–15. doi:10.1103/PhysRev.41.208.

[96] Jahn HA, Teller E. Stability of Polyatomic Molecules in Degenerate Electronic States. I. Orbital Degeneracy. Proc R Soc A Math Phys Sci 1937;161:220–35. doi:10.1098/rspa.1937.0142.

[97] Kohler T, Armbruster T, Libowitzky E. Hydrogen Bonding and Jahn–Teller Distortion in Groutite, α-MnOOH, and Manganite, γ-MnOOH, and Their Relations to the

Manganese Dioxides Ramsdellite and Pyrolusite. J Solid State Chem 1997;133:486–500. doi:10.1006/jssc.1997.7516.

[98] Ammundsen B, Jones DJ, Rozière J, Berg H, Tellgren R, Thomas JO. Ion Exchange in Manganese Dioxide Spinel: Proton, Deuteron, and Lithium Sites Determined from Neutron Powder Diffraction Data. Chem Mater 1998;10:1680–7. doi:10.1021/cm9800478.

[99] Bragg WH, Bragg WL. The Reflection of X-rays by Crystals. Proc R Soc A Math Phys Eng Sci 1913;88:428–38. doi:10.1098/rspa.1913.0040.

[100] Manolopoulos DE, May JC, Down SE. Theoretical studies of the fullerenes: C34 to C70. Chem Phys Lett 1991;181:105–11. doi:10.1016/0009-2614(91)90340-F.

[101] Ouyang CY, Šljivančanin Ž, Baldereschi A. Transition from Mn4+ to Mn3+ induced by surface reconstruction at λ-MnO2(001). J Chem Phys 2010;133. doi:http://dx.doi.org/10.1063/1.3509401.

[102] Li Y-F, Zhu S-C, Liu Z-P. Reaction Network of Layer-to-Tunnel Transition of MnO2. J Am Chem Soc 2016;138:5371–9. doi:10.1021/jacs.6b01768.

[103] Ammundsen B, Jones DJ, Roziere J, Burns GR. Mechanism of Proton Insertion and Characterization of the Proton Sites in Lithium Manganate Spinels. Chem Mater 1995;7:2151–60. doi:10.1021/cm00059a024.

[104] Bard AJ, Faulkner LR. Electrochemical Methods: Fundamentals and Applications, 2nd Edition. Wiley; 2 edition (December 18, 2000); 2000.

[105] Björketun ME, Sundell PG, Wahnström G. Effect of acceptor dopants on the proton mobility in BaZrO3: A density functional investigation. Phys Rev B 2007;76:54307. doi:10.1103/PhysRevB.76.054307.

[106] Crank J. The Mathematics of Diffusion. Second Edi. Clarendon Press; 1975.

[107] Shannon RD, Gumerman PS, Chenavas J. Effect of Octahedral Distortion on Mean Mn3+-O Distances. Am Mineral 1975;60:714–6.

[108] Fang CM, de Wijs GA. Local Structure and Chemical Bonding of Protonated Li x Mn2O4 Spinels from First Principles. Chem Mater 2006;18:1169–73. doi:10.1021/cm051564a.

[109] Bailey MR, Donne SW. Electrochemical Characterization of Proton Diffusion during Discharge and Cycling of -MnO2. J Electrochem Soc 2013;160:A2070–7. doi:10.1149/2.042311jes.

[110] Robinson DM, Go YB, Greenblatt M, Dismukes GC. Water Oxidation by λ-MnO2: Catalysis by the Cubical Mn4O4 Subcluster Obtained by Delithiation of Spinel LiMn2O4. J Am Chem Soc 2010;132:11467–9. doi:10.1021/ja1055615.

[111] Kalyani P. A new solution combustion route to synthesize LiCoO2 and LiMn2O4. J Power Sources 2002;111:232–8. doi:10.1016/S0378-7753(02)00307-5.

[112] Shaohorn Y, Eineii Y, Robertson AD, Averiii WF, Hackney SA, Howard WF. Morphology Modification and Delithiation Mechanisms of LiMn2O4 and Li2MnO3 by Acid Digestion n.d.

[113] Liu W-W, Yan X-B, Lang J-W, Pu J-B, Xue Q-J. Supercapacitors based on graphene nanosheets using different non-aqueous electrolytes. New J Chem New J Chem 2186;37:2186–95. doi:10.1039/c3nj00335c.

[114] Wang JX, Inada H, Wu L, Zhu Y, Choi Y, Liu P, et al. Oxygen Reduction on Well-Defined Core−Shell Nanocatalysts: Particle Size, Facet, and Pt Shell Thickness Effects. J Am Chem Soc 2009;131:17298–302. doi:10.1021/ja9067645.

[115] Zhou K, Li Y. Catalysis Based on Nanocrystals with Well-Defined Facets. Angew Chemie Int Ed 2012;51:602–13. doi:10.1002/anie.201102619.

[116] Arora P, Popov BN, White RE. Electrochemical investigations of cobalt-doped LiMn2O4 as cathode material for lithium-ion batteries. J Electrochem Soc 1998;145:807–15. doi:10.1149/1.1838349.

[117] Guohua L. The Spinel Phases LiMyMn2−yO4 (M = Co, Cr, Ni) as the Cathode for Rechargeable Lithium Batteries. J Electrochem Soc 1996;143:178. doi:10.1149/1.1836405.

[118] Liu W. Electrochemical Characteristics of Spinel Phase LiMn2O4-Based Cathode Materials Prepared by the Pechini Process. J Electrochem Soc 1996;143:3590. doi:10.1149/1.1837257.

[119] Gong K, Du F, Xia Z, Durstock M, Dai L. Nitrogen-doped carbon nanotube arrays with high electrocatalytic activity for oxygen reduction. Science 2009;323:760–4. doi:10.1126/science.1168049.

[120] Qu L, Liu Y, Baek J-B, Dai L. Nitrogen-doped graphene as efficient metal-free electrocatalyst for oxygen reduction in fuel cells. ACS Nano 2010;4:1321–6. doi:10.1021/nn901850u.

[121] Brunauer S, Emmett PH, Teller E. Adsorption of Gases in Multimolecular Layers. J Am Chem Soc 1938;60:309–19. doi:10.1021/ja01269a023.

[122] Prasad R, Benedek R, Thackeray MM. Dopant-induced stabilization of rhombohedral LiMnO2 against Jahn-Teller distortion. Phys Rev B - Condens Matter Mater Phys 2005;71:134111. doi:10.1103/PhysRevB.71.134111.

[123] Song GM, Li WJ, Zhou Y. Synthesis of Mg-doped LiMn2O4 powders for lithium-ion batteries by rotary heating. Mater Chem Phys 2004;87:162–7. doi:10.1016/j.matchemphys.2004.05.023.

[124] Chatenet M, Genies-Bultel L, Aurousseau M, Durand R, Andolfatto F. Oxygen reduction on silver catalysts in solutions containing various concentrations of sodium hydroxide – comparison with platinum. J Appl Electrochem 2002;32:1131–40. doi:10.1023/A:1021231503922.

[125] Serway RA, Gordon JR. Principles of Physics. Saunders College Pub.; 1998.

[126] Wiley JS, Knight HT. The Electrical Resistivity of Pyrolytic Beta MnO2. J Electrochem Soc 1964;111:656. doi:10.1149/1.2426205.

[127] Klose PH. Electrical Properties of Manganese Dioxide and Manganese Sesquioxide. J Electrochem Soc 1970;117:854. doi:10.1149/1.2407656.

[128] Venkatraman M, Van Zee JW. A model for the silver–zinc battery during high rates of discharge. J Power Sources 2007;166:537–48. doi:10.1016/j.jpowsour.2006.12.064.

[129] Allen J. Bard, Roger Parsons JJ. Standard Potentials in Aqueous Solution (Monographs in Electroanalytical Chemistry & Electrochemistry). New York, NY: Marcel Dekker, Inc.; 1985.

List of Publications

- M. Musil, B. Choi, A. Tsutsumi, Systematic Approach to Synthesize Different MnO_2 Crystalloid Structures and their Application in Fuel Cell/Battery Systems, *ECS Trans.*, 64, 19, pp. 63-71, 2015
- M. Musil, B. Choi, A. Tsutsumi, Morphology and Electrochemical Properties of α-, β-, γ-, and δ-MnO_2 Synthesized by Redox Method, *J. Electrochem. Soc.*, 162, 10, pp. A2058-A2065, 2015
- M. Musil, B. Choi, A. Tsutsumi, Novel λ-MnO_2 Positive Electrode Fuel Cell/Battery Systems, J. Electrochem. Soc., *accepted*
- M. Musil, B. Choi, A. Tsutsumi, Chemical Charging Mechanism of Manganese Dioxide in Fuel Cell/Battery Systems, *under preparation*
- M. Musil, B. Choi, A. Tsutsumi, Micro- and Nano-sized λ-MnO_2 for Fast Chemical Oxygen Charge Rate in Fuel Cell/Battery Systems, *under preparation*

Conferences

1. Mike Musil, Bokkyu Choi, Dhruba Panthi, Atsushi Tsutsumi
   Spinel MnO2 as a rapidly oxidizing cathode material for fuel cell/battery (FCB) systems
   ECS Conference on Electrochemical Energy Conversion & Storage with SOFC-XIV, Glasgow, Scotland, July 2015)

2. Mike Musil, Atsushi Tsutsumi,
   A metal hydride-manganese dioxide based electrochemical cell for high energy and power density fuel cell/battery (FCB) system,
   Asia-Pacific Conference on Electrochemical Energy Storage and Conversion (APEnergy2014), Brisbane, Australia, February 5-8, 2014

3. Mike Musil, Atsushi Tsutsumi,
   Novel Cathode Structures for the Development of a Fuel Cell/Battery System, 226th Meeting of the Society, Cancun, Mexico, October 5–9, 2014

4. Mike Musil, Atsushi Tsutsumi,
   A metal hydride-manganese dioxide based electrochemical cell for high energy and power density fuel cell/battery (FCB) system, 33rd Annual Meeting of Hydrogen Energy Systems Society of Japan, Dec. 12-13, Tokyo 2013

5. Mike Musil, Atsushi Tsutsumi
   "Novel Wave-Shaped MnO2 Cathode Supported by a Partially Porous Nickel Layer for Fuel Cell/Battery" 2012 AIChE Annual Meeting, Oct. 28-Nov. 2, 2012, Pittsburgh, PA, USA

Honors

- **Best Poster Award**(The Inaugural Asia-Pacific Conference on Electrochemical Energy Storage and Convention (APEnergy2014), 5-8 Feb., Brisbane, Australia 2014)
  "A Novel MnO_2 Structure Fabricated via Redox Deposition Method for Alkaline Batteries"
  Feb. 8, 2014
- **Best Student Poster Award**(33rd Annual Meeting of Hydrogen Energy Systems Society of Japan, 12-13 Dec., Tokyo 2013)
  "A metal hydride-manganese dioxide based electrochemical cell for high energy and power density fuel cell/battery (FCB) system"
  Dec. 12, 2013